ABSTRACT

Title of dissertation: RADIO ANALYTICS FOR HUMAN ACTIVITY MONITORING AND INDOOR TRACKING

Feng Zhang
Doctor of Philosophy, 2018

Dissertation directed by: Professor K. J. Ray Liu
Department of Electrical and Computer Engineering

With the rapid development of the Internet of Things (IoT), wireless sensing has found wide applications from wellbeing monitoring, activity recognition, to indoor tracking. In this dissertation, we investigate the problem of wireless sensing for IoT applications using only ambient radio signals, e.g., WiFi, LTE, and 5G. In particular, our work mainly focuses on passive speed estimation, motion detection, sleep monitoring, and indoor tracking for wireless sensing.

In this dissertation, we first study the problem of indoor speed estimation using WiFi channel state information (CSI). We develop the statistical electromagnetic (EM) wave theory for wireless sensing and establish a link between the autocorrelation function (ACF) of the physical layer CSI and the speed of a moving object. Based on the developed statistical EM wave theory for wireless sensing, we propose a universal low-complexity indoor speed estimation system leveraging CSI, which can work in both device-free and device-based situations. The proposed speed estimator differs from the other schemes requiring strong

line-of-sight conditions between the source and observer in that it embraces the rich-scattering environment typical for indoors to facilitate highly accurate speed estimation. Moreover, as a calibration-free system, it saves the users' efforts from large-scale training and fine-tuning of system parameters. The proposed speed estimator can enable many IoT applications, e.g., gait monitoring, fall detection, and activity recognition.

Then, we also study the problem of indoor motion detection using CSI. The statistical behaviors of the CSI dynamics when motion presents can be characterized by the developed statistical EM theory for wireless sensing. We formulate the motion detection problem as a hypothesis testing problem and also derive the relationship between the detection rate and false alarm rate for motion detection, which is independent of locations, environments and motion types. Thus, the proposed motion detection system can work in most indoor environments, without any scenario-tailored training efforts. Extensive experiments conducted in several facilities show that the proposed system can achieve better detection performance compared to the existing CSI-based motion detection systems while maintaining a much larger coverage and a much lower false alarm rate.

This dissertation also focuses on sleep monitoring using CSI. First, we build a statistical model for maximizing the signal-to-noise (SNR) ratio of breathing signal, which accounts for all reflecting and scattering multipaths, allowing highly accurate and instantaneous breathing estimation with best-ever performance achieved on commodity devices. Our results demonstrate that the proposed breathing estimator yields a median absolute error of 0.47 bpm and a 95%-tile

error of only 2.92 bpm for breathing estimation, and detects breathing robustly even when a person is 10m away from the WiFi link, or behind a wall. Then, we apply machine learning algorithms on the extracted features from the estimated breathing rates to classify different sleep stages, including wake, rapid eye movement (REM), and non-REM (NREM), which was previously only possible with dedicated hardware. Experimental results show that the proposed sleep monitoring system achieves sleep staging accuracy of 88%, outperforming advanced solutions using contact sensor or radar.

The last work of this dissertation considers the problem of indoor tracking using CSI. First, we leverage a stationary and location-independent property of the time-reversal (TR) focusing effect of radio signals for highly accurate moving distance estimation, which plays a key role in the proposed indoor tracking system. Together with the direction estimation based on inertial measurement unit and location correction using the constraints from the floorplan, the proposed indoor tracking system is shown to be able to track a moving object with decimeter-level accuracy in different environments.

RADIO ANALYTICS FOR HUMAN ACTIVITY MONITORING AND INDOOR TRACKING

by

Feng Zhang

Dissertation submitted to the Faculty of the Graduate School of the
University of Maryland, College Park in partial fulfillment
of the requirements for the degree of
Doctor of Philosophy
2018

Advisory Committee:
Professor K. J. Ray Liu, Chair/Advisor
Professor Min Wu
Professor Gang Qu
Dr. Zoltan Safar
Professor Lawrence C. Washington

© Copyright by
Feng Zhang
2018

Dedication

To my family—

Jingyi Zhang, Tingchun Yang

Hangfang Zhang, Jun Zhang, and Yanfei Xu

Acknowledgments

Firstly, I would like to express my sincere gratitude to my advisor Prof. K. J. Ray Liu for the continuous support of my Ph.D. study and related research, for his patience, motivation, and immense knowledge. His guidance helped me in all the time of research and writing of this thesis. I could not have imagined having a better advisor and mentor for my Ph.D. study.

Besides my advisor, I would like to thank the rest of my thesis committee: Prof. Min Wu, Prof. Gang Qu, Dr. Zoltan Safar, and Prof. Lawrence C. Washington for their support of my Ph.D. defense and their insightful comments and encouragement.

My sincere thanks also goes to Dr. Chen Chen and Dr. Beibei Wang, who lead me in the research. Without their precious support, it would not be possible to conduct this research.

I thank my fellow labmates: Chen Chen, Zhunghan Wu, Qinyi Xu, Chenshu Wu, Deepika Regani, Yi Han, Yuqian Hu, Ruomin Ba, Yusen Fan, and Xiaolu Zeng for the stimulating discussions, for the sleepless nights we were working together before deadlines, and for all the fun we have had in the last four years. In particular, I am grateful to Dr. Chen Chen for enlightening me the first glance of research and work hard with me even in the midnight.

Last but not least, I would like to thank my family: Jingyi Zhang and Tingchun Yang, and Hangfang Zhang, for supporting me spiritually throughout writing this thesis and my life in general.

Table of Contents

List of Tables

List of Figures

List of Abbreviations

ACF	Autocorrelation Function
AoA	Angle of Arrival
CDF	Cumulative Distribution Function
COV	Covariance
CFO	Channel Frequency Offset
CFR	Channel Frequency Response
CIR	Channel Impulse Response
CSI	Channel State Information
ECDF	Empirical Cumulative Distribution Function
EM	Electromagnetic
FMCW	Frequency Modulated Continuous Wave
FFT	Fast Fourier Transform
IoT	Internet of Things
IPIN	Indoor Positioning and Indoor Navigation
LOS	Line of Sight
MAE	Median Absolute Error
MIMO	Multiple Input Multiple Output
MHz	Megahertz
MRC	Maximal Ratio Combining
MUSIC	Multiple Signal Classification
NLOS	Non Line of Sight
PCA	Principal Component Analysis
RF	Radio Frequency
RSS	Received Signal Strength
RSSI	Received Signal Strength Indicator
RX	Receiver
SFO	Sampling Frequency Offset
SNR	Signal-toNoise Radio
STO	Symbol Timing Offset

ToA	Time of Arrival
ToF	Time of Flight
TRRS	Time Reversal Resonance Strength
TR	Time-Reversal
TX	Transmitter
UWB	Ultra-Wide Band

Chapter 1: Introduction

1.1 Motivation

With the development of wireless technologies in the era of the Internet of Things (IoT), people are paying more and more attention to understand the who, what, when, where, and how of everything happening surrounding them with wireless technologies. Human activities can affect wireless signal propagations surrounding them, and information about their activities is in turn embedded in the signals. This makes one wonder whether one can extract meaningful information through wireless sensing by analyzing various features embedded in wireless signals.

By deploying wireless transceivers indoors, macro changes due to human activities and moving objects can be extracted from the wireless signals, which can help infer the real-time location of a moving object, and facilitate applications in manufacturing asset tracking, intelligent transportation, and home/office security systems. In addition, micro changes generated by gestures and vital signals can also be captured without requiring people to wear any device, which is especially useful for providing assistance to the disabled and elderly people in smart home applications.

The traditional wireless sensing systems utilize dedicated devices, e.g., UWB [97], Doppler RADAR [30], FMCW RADAR [8], etc., to monitor human activities in the environment. However, these devices are very costly and need to be well-calibrated before use, which is not easy for ordinary people to use.

A very natural question then arises: instead of using specialized wireless systems, can we utilize the readily available ubiquitous wireless signals, e.g., WiFi signals, to sense the environment in which we live? Motivated by this question, in this dissertation, we will explore its answer from the perspectives of the following important IoT applications — *passive speed estimation*, *motion detection*, *sleep monitoring* and *indoor tracking*:

1. *Passive speed estimation* enables a large number of important indoor applications such as indoor fitness tracking, fall detection, gait monitoring, etc. Especially, fall detection is important to the seniors who live alone in their homes, as the system can detect falls which impose major threats to their lives.

2. *Motion detection* plays a fundamental role in many applications, including security surveillance, in-home activity monitoring, smart building analysis, etc. Nowadays, motion detection systems are often employed for intruder monitoring, elder care, and event detection, etc.

3. *Sleep monitoring* plays a vital role in assessing the quantity and quality of an individual's sleep, which is fundamentally related to health risks like cardiovascular disease, stroke, kidney failure, diabetes, and adverse mental

conditions, etc.

4. *Indoor tracking* has received an increasing attention in recent years. Technavio forecasts the global IPIN market to grow to USD 7.8 billion by 2021 [3], and more than ever before, enterprises of all sizes are investing in indoor tracking technology to support a growing list of applications, including patient tracking in hospitals, asset management for large groceries, workflow automation in large factories, navigation in malls, appliance control, etc.

1.2 Related Works

This dissertation is widely related to RF-based (especially WiFi-based) human activity sensing, viral sign monitoring, and localization. The related works are reviewed in the following subsections, respectively.

1.2.1 Human Activity Sensing

Existing works on WiFi-based human activity sensing techniques using commercial WiFi include gesture recognition [5, 11, 77, 81, 103], human behavior recognition [107, 113, 114], motion tracing [9, 96], passive localization [78, 88], vital signal estimation [6, 24, 60], indoor event detection [126] and so on. These approaches are built upon the phenomenon that human motions inevitably distort the WiFi signal and can be recorded by WiFi receivers for further analysis. In terms of the principles, these works can be divided into two categories: learning based and modeling based. Details of the two categories are elaborated below.

Learning-based: These schemes consist of two phases, namely, an offline phase, and an online phase. During the offline phase, features associated with different human activities are extracted from the WiFi signals and stored in a database; in the online phase, the same set of features are extracted from the instantaneous WiFi signals and compared with the stored features so as to classify the human activities. The features can be obtained either from channel state information (CSI) or the Received Signal Strength Indicator (RSSI), a readily available but low granularity information encapsulating the received power of WiFi signals. For example, E-eyes [114] utilizes histograms of the amplitudes of CSI to recognize daily activities such as washing dishes and brushing teeth. CARM [107] exploits features from the spectral components of CSI dynamics to differentiate human activities. WiGest [5] exploits the features of RSSI variations for gesture recognition. After the features are obtained, then different machine learning methods, such as SVM, deep neural network, HMM, etc., are applied to implement classification.

A major drawback of the learning-based approach lies in that the extracted features are susceptible to the external factors, such as the changes in the environment, the heterogeneity in human subjects, the changes of device locations, etc., which might violate their underlying assumption of the reproducibility of the features in the offline and online phases.

Modeling-based: Based on the adopted techniques, they can be classified into multipath-avoidance and multipath-attenuation. The multipath-avoidance schemes track the multipath components only reflected by a human body and

avoid the other multipath components. Either a high temporal resolution [7] or a "virtual" phased antenna array is used [9], such that the multipath components relevant to motions can be discerned in the time domain or in the spatial domain from those irrelevant to motions. The drawback of these approaches is the requirement of dedicated hardware, such as USRP, WARP [67], etc., to achieve a fine-grained temporal and spatial resolution, which is unavailable on WiFi devices. Note that on commercial main-stream 802.11ac WiFi devices, the maximum bandwidth is 160 MHz, much smaller than the 1.69 GHz bandwidth in WiTrack. Meanwhile, commercial WiFi devices with multiple antennas cannot work as a (virtual) phased antenna array out-of-box before carefully tuning the phase differences among the RF front-ends.

In the multipath-attenuation schemes, the impact of multipath components is attenuated by placing the WiFi devices in the close vicinity of the monitored subjects, so that the majority of the multipath components are affected by the subject [78, 81, 96]. The drawback is the requirement of a very strong LOS working condition, which limits their deployment in practice.

1.2.2 Vital Sign Monitoring

Many works exploit WiFi signals to estimate breathing [47, 70, 74, 104, 112, 116] and/or sleep monitoring [60, 61]. Despite that only controlled and short studied are conducted, these works cannot learn sleep stages due to large estimation errors. For example, the approaches proposed in [60] produce 95%-

tile error of >10 bpm, as evaluated by [42]. To increase the tracking ability of the breathing estimation, a time-domain-based method is also proposed in [60], which uses a peak detector on the smoothed CSI amplitudes of the selected subcarriers. FMCW radar [10,43,142] is also leveraged to monitor breathing. Among them, [43,142] is capable of staging sleep, which, however, rely on specialized radios, rendering them not ubiquitously applicable.

1.2.3 Indoor Localization and Tracking

Table 1.1 summarizes typical WiFi-based localization systems. In general, these works can be classified into two categories: modeling-based approach and fingerprinting-based approach. The features utilized in these approaches can be obtained either from the RSSI readings and the timestamps of the received packets at the receiver (RX) or from the CSI.

In the modeling-based schemes, either the distance [33] [89] [15] [122] or the angle [52] [34] [90] between an anchor point and the device can be estimated and the device can be localized by performing geometrical triangulation. The distance between the anchor point and the device can be estimated from the decay of RSSI [132] or from the time of arrival (ToA) of the transmitted packets which can be extracted from the timestamps of the received packets [125]. The angle in between can be obtained by examining the features of the CSI received by multiple receive antennas, and then, the angle of arrival (AoA) of the direct path to the target can be calculated. ToA-based methods typically require synchronization

between the anchor point and the device and thus are very sensitive to timing offsets [35]; AoA-based methods require an array of phased antennas which are not readily available in commercial WiFi chips [34]. Recently, a decimeter-level tracking system, Widar, is proposed in [79] and [80], however, the system can only work in a small area with the constraint of LOS. The main challenges for the modeling-based approaches are the blockage and reflection of the transmitted signal since only the signal coming from the direct path between the anchor point and the device is useful for localization.

The fingerprinting-based schemes consist of an offline phase and an online phase. During the offline phase, features associated with different locations are extracted from the WiFi signals and stored in a database; in the online phase, the same features are extracted from the instantaneous WiFi signals and compared with the stored features so as to classify the locations. The features can be obtained either from the vector of RSSIs [132] [21] or the detailed CSI [111] [110] [119] from a specific location to all the anchor points in range. A major drawback of the fingerprinting-based approaches lies in that the features they use are susceptible to the dynamics of the environment. For example, the change of furniture or the status of doors may have a severe impact on these features and the database of the mapped fingerprints need to be updated before it can be used again. In addition, the computational complexity of the fingerprinting-based approaches scales with the size of the database and thus they are not feasible for low-latency applications, especially when the number of the collected fingerprints is large.

Table 1.1: Summary of typical WiFi-based localization systems

	Method	Existing Solutions
Modeling-based	ToA	CAESAR [33], ToneTrack [125]
	AoA	ArrayTrack [124], SpotFi [52], Phaser [34]
	RSSI	RADAR [15]
	CSI	FILA [118]
Fingerprinting-based	RSSI	Horus [132], Nibble [21]
	CSI	PinLoc [92], TRIPS [119], DeepFi [111]

1.3 Dissertation Outline and Contributions

Considering the limitations of current studies discussed in Section 1.2, we are motivated to develop new radio analytic techniques that can not only fully utilize the information embedded in radio signals, but also support simple implementation with commercial WiFi devices.

In this dissertation, we first introduce the primer of wireless sensing in Chapter 2, i.e., the wireless channel models for wireless sensing and the techniques for information extraction from the multipaths. Then, we presents four different indoor monitoring systems, that is, a passive indoor speed estimation system, an indoor motion detection system, a sleep monitoring system, and an indoor tracking system. that exploit CSI with different radio analytic methods, in Chapter 3, Chapter 4, Chapter 5, and Chapter 6, respectively. Chapter 7 concludes the dissertation.

The contributions and outline of Chapter 3–6 are described as follows.

1.3.1 Speed Estimation: a Statistical Electromagnetic Approach (Chapter 3)

In this chapter, we present WiSpeed, a universal low-complexity indoor speed estimation system leveraging radio signals, such as commercial WiFi, LTE, 5G, etc., which can work in both device-free and device-based situations. By exploiting the statistical theory of electromagnetic waves, we establish a link between the autocorrelation function of the physical layer channel state information and the speed of a moving object, which lays the foundation of WiSpeed. WiSpeed differs from the other schemes requiring strong line-of-sight conditions between the source and observer in that it embraces the rich-scattering environment typical for indoors to facilitate highly accurate speed estimation. Moreover, as a calibration-free system, WiSpeed saves the users' efforts from large-scale training and fine-tuning of system parameters. In addition, WiSpeed could extract the stride length as well as detect abnormal activities such as falling down, a major threat to seniors that leads to a large number of fatalities every year. Extensive experiments show that WiSpeed achieves a mean absolute percentage error of 4.85% for device-free human walking speed estimation and 4.62% for device-based speed estimation, and a detection rate of 95% without false alarms for fall detection.

1.3.2 Robust Whole-Home Motion Detection With a Single WiFi Link (Chapter 4)

In this chapter, we propose WiDetect, a highly accurate, calibration-free, and low-complexity wireless motion detector. By exploiting the statistical theory of electromagnetic waves, we establish a link between the autocorrelation function of the physical layer channel state information (CSI) and human motion in the environment. Temporal, frequency and spatial diversities are also exploited to further improve the robustness and sensitivity of WiDetect. Extensive experiments conducted in several facilities show that WiDetect can achieve better detection performance compared to a commercial home security system, while with much larger coverage and lower cost.

1.3.3 Sleep Staging via Respiratory Rate Monitoring (Chapter 5)

In this chapter, we present the model, design, and implementation of S-MARS, the first practical Sleep Monitoring system that exploits Ambient Radio Signals to recognize sleep stages and assess sleep quality. This will enable a future smart home that monitors daily sleep in a ubiquitous, non-invasive and contactless manner, without instrumenting the subject's body or the bed. The key enabler underlying SMARS is a statistical model that accounts for all reflecting and scattering multipaths, allowing highly accurate and instantaneous breathing estimation with best-ever performance achieved on commodity devices. On this

basis, SMARS then recognizes different sleep stages, including wake, rapid eye movement (REM), and non-REM (NREM), which was previously only possible with dedicated hardware. We implement a real-time system on commercial WiFi chipsets and deploy it in 6 homes, resulting in 32 nights of data in total. Our results demonstrate that SMARS yields a median absolute error of 0.47 bpm and a 95%-tile error of only 2.92 bpm for breathing estimation, and detects breathing robustly even when a person is 10m away from the link, or behind a wall. SMARS achieves sleep staging accuracy of 88%, outperforming advanced solutions using contact sensor or radar. The performance is also validated upon a public sleep dataset of 20 patients. By achieving promising results with merely a single commodity RF link, we believe that SMARS will set the stage for a practical in-home sleep monitoring solution.

1.3.4 Indoor Tracking: a Time-Reversal Focusing Ball Approach (Chapter 6)

In this chapter, we propose WiBall, an accurate and calibration-free indoor tracking system that can work well in non-line-of-sight based on radio signals. WiBall leverages a stationary and location-independent property of the time-reversal focusing effect of radio signals for highly accurate moving distance estimation. Together with the direction estimation based on inertial measurement unit and location correction using the constraints from the floorplan, WiBall is shown to be able to track a moving object with decimeter-level accuracy in d-

ifferent environments. Since WiBall can accommodate a large number of users with only a single pair of devices, it is low-cost and easily scalable, and can be a promising candidate for future indoor tracking applications.

Chapter 2: Primer of Wireless Sensing

In wireless sensing, wireless channel models play a paramount role as it can depict how human activities or environmental dynamics can affect the received radio signals. In this chapter, we first introduce the wireless channel models, which include the model of the propagation of radio signals, the model of the noise measurements of wireless channels in practical system, and the methods to deal with the noise. Then, we introduce two multipath diversity harvesting approaches, time-reversal technique and statistical EM wave theory, to extract the environmental information embedded in each multipath from the received wireless signals.

2.1 Wireless Channel Models for Wireless Sensing

Given a wireless transmission pair each equipped with omnidirectional antennas, the channel impulse response (CIR) at time t can be expressed as

$$h(\tau, t) = \sum_{l \in \Omega} a_l(t)\delta(\tau - \tau_l(t)), \tag{2.1}$$

where $a_l(t)$ and $\tau_l(t)$ denote the complex channel gain and propagation delay of the l-th multipath component (MPC), respectively, Ω denotes the set of MPCs, and $\delta(\cdot)$ denotes the Dirac delta function [98]. The propagation delay is a function

of the propagation distance: $\tau_l(t) = \frac{d_l(t)}{c}$, where c is the speed of light and $d_l(t)$ is the traveled distance of the l-th MPC.

In practice, the complex channel gains and propagation delays are usually slowly varying functions of frequency, however, we are primarily interested in transmitting over bands that are narrow relative to the carrier frequency, and over such ranges the dependency on the frequency can be ignored. It should be noted that although the individual channel gains and delays are assumed to be independent of the frequency, the overall channel response can still vary with frequency due to the fact that different multipaths have different delays.

For the time-varying impulse response $h(\tau, t)$, we can further define a time-varying channel frequency response (CFR), also called Channel State Information (CSI), as follows.

$$H(t, f) = \sum_{l \in \Omega} a_l(t) \exp(-j2\pi f \tau_l(t)), \tag{2.2}$$

where f denotes the particular frequency where the channel is measured. For example, in an OFDM-based communication system, such as WiFi, LTE, 5G, etc., the CSI is measured at each subcarrier with frequency f.

CSI depicts how radio signals propagate from a transmitter (Tx) to a receiver (Rx), e.g., reflected or scattered off all reflectors in the space such as the walls, furniture, human bodies, etc., and is highly sensitive to environmental perturbations. Any environmental dynamics, including walking, gestures and even minute human chest and abdomen movements, will alter the paths of signal propagation and thus modulate the wireless signal before it arrives at the

receiver, allowing wireless sensing technologies to capture these activities from the measured CSI time series.

In principle, the MPCs can be classified into two sets: $\Omega_s(t)$ and $\Omega_d(t)$, where $\Omega_s(t)$ denotes the set of time-invariant MPCs, e.g., reflected off the floor and walls, and $\Omega_d(t)$ denotes the set of time-varying MPCs, e.g., reflected off the human body.

When the channel sampling rate F_s is large enough, it is reasonable to assume that both the sets $\Omega_s(t)$, $\Omega_d(t)$ and the complex amplitude of each MPC $a_l(t)$ are time-invariant within a sufficiently short period. Thus the CSI can be written as

$$\begin{aligned} H(t,f) &= \sum_{l_s \in \Omega_s} a_{l_s} \exp(-j2\pi f \frac{d_{l_s}}{c}) + \sum_{l_d \in \Omega_d} a_{l_d} \exp(-j2\pi f \frac{d_{l_d}(t)}{c}) \\ &\triangleq H_s(f) + H_d(t,f), \end{aligned} \tag{2.3}$$

where $H_s(f)$ and $H_d(t,f)$ denote the contribution of the time-invariant MPCs and time-varying MPCs, respectively.

In real measurements, $H(t,f)$ is often corrupted by the phase noise, caused by the timing and frequency synchronization offsets, and the additive thermal noise $n(t,f)$, and the reported CSI $\tilde{H}(t,f)$ can be expressed as

$$\tilde{H}(t,f) = \exp(-j(\alpha(t) + \beta(t)f))H(t,f) + n(t,f), \tag{2.4}$$

where $\alpha(t)$ and $\beta(t)$ are the random initial and linear phase distortions at time t, respectively.

Since the information of environmental dynamics is embedded in the time-varying MPCs $H_d(t,f)$, the core of wireless sensing technologies is to extract

$H_d(t,f)$ from the noisy measurements. In literation, there are two approaches to deal with the phase distortions: *phase cleaning* [25,78,91,128] and *phase elimination* [107,113,138].

For the *phase cleaning* approach, the phase distortions are partially removed and both the phase information and amplitude information are used. Take the phase $\tilde{\phi}(f)$ of the measured CSI $\tilde{H}(t,f)$, and for $f = 1,\ldots,F$, we have

$$\tilde{\phi}(f) = \alpha(t) + \beta(t)f + \angle n(t,f). \tag{2.5}$$

Since the thermal noise is much smaller than the CSI, the phase distortion incurred by the thermal noise can be ignored and we have the approximation:

$$\tilde{\phi}(f) \approx \alpha(t) + \beta(t)f, \tag{2.6}$$

where $f = 1,\cdots,F$. Then, a simple linear regression can be applied to estimate the slope of the linear phase distortion $\beta(t)$ at time t. However, the initial phase offset $\alpha(t)$ can not be removed.

For the *phase elimination* approach, only the amplitude information is used and the phase information is discarded. Define the *channel power response* $G(t,f)$ as the square of the magnitude of $\tilde{H}(t,f)$:

$$\begin{aligned} G(t,f) &\triangleq |\tilde{H}(t,f)|^2 \\ &= |H(t,f)|^2 + 2\mathrm{Re}\{n^*(t,f)H(t,f) \\ &\quad \exp(-j(\alpha(t)+\beta(t)f))\} + |n(t,f)|^2 \\ &\triangleq |H(t,f)|^2 + \varepsilon(t,f) \end{aligned} \tag{2.7}$$

where the superscript * denotes the operator of complex conjugate, the operator

Re$\{x\}$ denotes the real part of x, and $\varepsilon(t, f)$ is defined as the noise term, which can be approximated as additive white Gaussian noise (AWGN) with variance $\sigma^2(f)$ and is statistically independent of $H(t, f)$. The approximation implicitly exploits the fact that the magnitude of thermal noise is usually much smaller than that of CSI.

2.2 Multipath Diversity Harvesting

The performance of wireless sensing depends greatly on the richness of information that can be extracted from the radio signals, while the information richness is often dictated by the channel bandwidth through which the radio signals are transmitted. With more and more bandwidth available for the wireless systems nowadays, many more smart IoT applications and services only-imagined today may be possible in the near future, because richer information becomes available with a wider bandwidth. For example, one can see many more multipaths in indoors with a much larger bandwidth, which can serve as hundreds of virtual antennas/sensors.

How to utilize these multipaths to meet our needs for smart IoT applications? In this dissertation, we propose two multipath harvesting and manipulation schemes, that is, statistical EM wave theory and time-reversal technique, to extract the information embedded in each multipath from the received wireless signals. Inspired by the above two multipath harvesting schemes, various types of analytics, referred to as radio analytics, based on the wireless channel state

information can be developed to enable many cutting-edge IoT applications that have been envisioned for a long time, but have never been achieved.

The first approach is to resort to the statistical EM wave theory [40]. Radio propagation in a building interior is in general very difficult to be analyzed because that the EM waves can be absorbed and scattered by walls, doors, windows, moving objects, etc. However, buildings and rooms can be viewed as reverberation cavities in that they exhibit internal multipath propagations. Hence, instead of deterministic models, e.g., ray-tracing, we apply the statistical theory of EM fields developed for reverberation cavities to analyze the statistical properties of the multipaths. Environmental dynamics can be thus reflected by the change of the derived statistical metrics. We take the first approach in the following applications: fall detection [138], motion detection [137], and sleep monitoring [139].

The second multipath harvesting approach is to resort to the time reversal (TR) phenomenon [102, 127, 135]. TR technique treats each path of the multipath channel as a distributed virtual antenna and provide a high resolution spatial-temporal resonance, commonly known as the focusing effect [26, 46, 65]. In physics, the TR spatial-temporal resonance can be viewed as the result of the resonance of electromagnetic (EM) field in response to the environment. When the propagation environment changes, the involved multipath signal varies correspondingly and consequently the spatial-temporal resonance also changes. We take the second approach in the application of indoor tracking [136].

Chapter 3: Speed Estimation: a Statistical Electromagnetic Approach

As people are spending more and more their time indoors nowadays, understanding their daily indoor activities will become a necessity for future life. Since the speed of the human body is one of the key physical parameters that can characterize the types of human activities, speed estimation of human motions is a critical module in human activity monitoring systems. Compared with traditional wearable sensor-based approaches, device-free speed estimation is more promising due to its better user experience, which can be applied in a wide variety of applications, such as smart homes [48], health care [76], fitness tracking [86], and entertainment.

Nevertheless, indoor device-free speed estimation is very challenging mainly due to the severe multipath propagations of signals and the blockage between the monitoring devices and the objects under monitoring. Conventional approaches of motion sensing require specialized devices, ranging from RADAR, SONAR, laser, to camera. Among them, the vision-based schemes [106] can only perform motion monitoring in their fields of vision with performance degradation in dim light conditions. Also, they introduce privacy issues. Meanwhile, the

speed estimation produced by RADAR or SONAR [37] varies for different moving directions, mainly because of the fact that the speed estimation is derived from the Doppler shift which is relevant to the moving direction of an object. Also, the multipath propagations of indoor spaces further undermine the efficacy of RADAR and SONAR.

In this chapter, we present WiSpeed, a robust universal speed estimator for human motions in a rich-scattering indoor environment, which can estimate the speed of a moving object under either the device-free or device-based condition. WiSpeed is actually a fundamental principle which requires no specific hardware as it can simply utilize only a single pair of commercial off-the-shelf WiFi devices.

The rest of this chapter is organized as follows. Section 3.1 introduces the statistical theory of EM waves in cavities and its extensions for wireless motion sensing. Section 3.2 presents the basic principles and detailed designs of WiSpeed. Experimental evaluation is shown in Section 3.3. Section 3.4 discusses the parameter selections and the computational complexity of WiSpeed and Section 3.5 summarizes this chapter.

3.1 System Model

In this section, we first decompose the received electric field at the Rx into different components and then, the statistical behavior of each component is analyzed under certain statistical assumptions.

3.1.1 Decomposition of the Received Electric Field

To provide an insight into the impact of motions on the EM waves, we consider a rich-scattering environment as illustrated in Fig. 3.1(a), which is typical for indoor spaces. The scatterers are assumed to be diffusive and can reflect the impinging EM waves towards all directions. A transmitter (Tx) and a receiver (Rx) are deployed in the environment, both equipped with omnidirectional antennas. The Tx emits a continuous EM wave via its antennas, which is received by the Rx. In an indoor environment or a reverberating chamber, the EM waves are usually approximated as plane waves, which can be fully characterized by their electric fields. Let $\vec{E}_{Rx}(t, f)$ denote the electric field received by the receiver at time t, where f is the frequency of the transmitted EM wave. In order to analyze the behavior of the received electric field, we decompose $\vec{E}_{Rx}(t, f)$ into a sum of electric fields contributed by different scatterers based on the superposition principle of electric fields

$$\vec{E}_{Rx}(t, f) = \sum_{i \in \Omega_s(t)} \vec{E}_i(t, f) + \sum_{j \in \Omega_d(t)} \vec{E}_j(t, f), \tag{3.1}$$

where $\Omega_s(t)$ and $\Omega_d(t)$ denote the set of static scatterers and dynamic (moving) scatterers, respectively, and $\vec{E}_i(t, f)$ denotes the part of the received electric field scattered by the i-th scatterer. The intuition behind the decomposition is that each scatterer can be treated as a "virtual antenna" diffusing the received EM waves in all directions and then these EM waves add up together at the receive antenna after bouncing off the walls, ceilings, windows, etc. of the building.

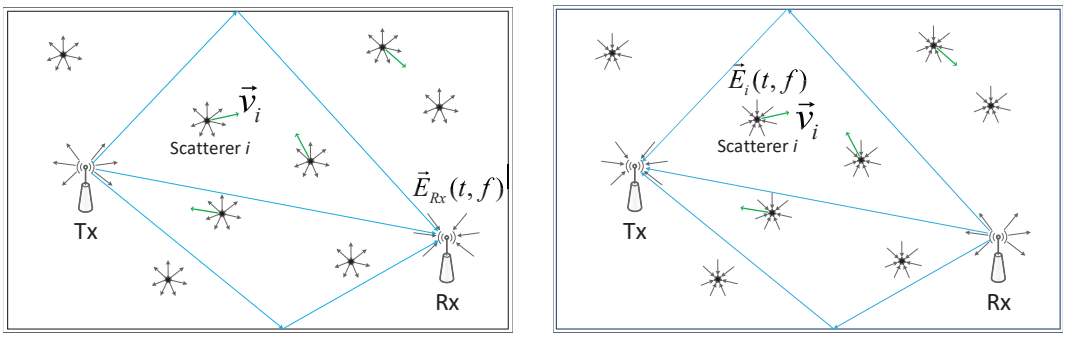

(a) Propagation of radio signals in rich scattering environment.

(b) Understanding $\vec{E}_i(t,f)$, $i \in \Omega_d(t)$ using channel reciprocity.

Figure 3.1: Illustration of wave propagation with many scatterers.

When the transmit antenna is static, it can be considered to be a "special" static scatterer, i.e., $Tx \in \Omega_s(t)$; when it is moving, it can be classified in the set of dynamic scatterers, i.e., $Tx \in \Omega_d(t)$. The power of $\vec{E}_{Tx}(t,f)$ dominates that of electric fields scattered by scatterers.

Within a sufficiently short period, it is reasonable to assume that both the sets $\Omega_s(t)$, $\Omega_d(t)$ and the electric fields $\vec{E}_i(t,f)$, $i \in \Omega_s(t)$ change slowly in time. Then, we have the following approximation:

$$\vec{E}_{Rx}(t,f) \approx \vec{E}_s(f) + \sum_{j \in \Omega_d} \vec{E}_j(t,f), \tag{3.2}$$

where $\vec{E}_s(f) \approx \sum_{i \in \Omega_s(t)} \vec{E}_i(t,f)$.

3.1.2 Statistical Behaviors of the Received Electric Field

As is known from the channel reciprocity, EM waves traveling in both directions will undergo the same physical perturbations (i.e. reflection, refraction, diffraction, etc.). Therefore, if the receiver were transmitting EM waves, all the

scatterers would receive the same electric fields as they contribute to $\vec{E}_{Rx}(t,f)$, as shown in Fig. 3.1(b). Therefore, in order to understand the properties of $\vec{E}_{Rx}(t,f)$, we only need to analyze its individual components $\vec{E}_i(t,f)$, which is equal to the received electric field by the i-th scatterer as if the Rx were transmitting. Then, $\vec{E}_i(t,f)$ can be interpreted as an integral of plane waves over all direction angles, as shown in Fig. 3.2. For each incoming plane wave with direction angle $\Theta = (\alpha, \beta)$, where α and β denote the elevation and azimuth angles, respectively, let $\vec{k}$ denote its vector wavenumber and let $\vec{F}(\Theta)$ stand for its angular spectrum which characterizes the electric field of the wave. The vector wavenumber $\vec{k}$ is given by $-k(\hat{x}\sin(\alpha)\cos(\beta) + \hat{y}\sin(\alpha)\sin(\beta) + \hat{z}\cos(\alpha))$ where the corresponding free-space wavenumber is $k = \frac{2\pi f}{c}$ and c is the speed of light. The angular spectrum $\vec{F}(\Theta)$ can be written as $\vec{F}(\Theta) = F_\alpha(\Theta)\hat{\alpha} + F_\beta(\Theta)\hat{\beta}$, where $F_\alpha(\Theta)$, $F_\beta(\Theta)$ are complex numbers and $\hat{\alpha}$, $\hat{\beta}$ are unit vectors that are orthogonal to each other and to $\vec{k}$. If the speed of the i-th scatterer is v_i, then $\vec{E}_i(t,f)$ can be represented as

$$\vec{E}_i(t,f) = \int_0^{2\pi} \int_0^{\pi} \vec{F}(\Theta) \exp(-j\vec{k}\cdot\vec{v}_i t)\sin(\alpha)\,\mathrm{d}\alpha\,\mathrm{d}\beta, \tag{3.3}$$

where z-axis is aligned with the moving direction of scatterer i, as illustrated in Fig. 3.2, and time dependence $\exp(-j2\pi f t)$ is suppressed since it does not affect any results that will be derived later. The angular spectrum $\vec{F}(\Theta)$ could be either deterministic or random. The electric field in 3.3 satisfies Maxwell's equations because each plane-wave component satisfies Maxwell's equations [40].

Radio propagation in a building interior is in general very difficult to be analyzed because that the EM waves can be absorbed and scattered by walls, doors,

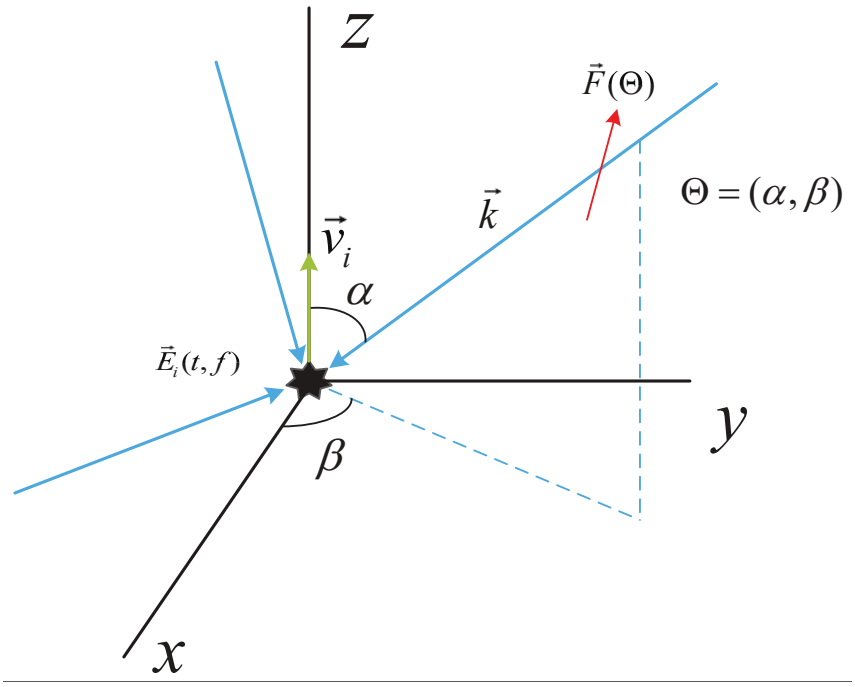

Figure 3.2: Plane wave component $\vec{F}(\Theta)$ of the electric field with vector wavenumber $\vec{k}$.

windows, moving objects, etc. However, buildings and rooms can be viewed as reverberation cavities in that they exhibit internal multipath propagations. Hence, we refer to a statistical modeling instead of a deterministic one and apply the statistical theory of EM fields developed for reverberation cavities to analyze the statistical properties of $\vec{E}_i(t,f)$. We assume that $\vec{E}_i(t,f)$ is a superposition of a large number of plane waves with uniformly distributed arrival directions, polarizations, and phases, which can well capture the properties of the wave functions of reverberation cavities [40]. Therefore, we take $\vec{F}(\Theta)$ to be a random variable and the corresponding statistical assumptions on $\vec{F}(\Theta)$ are summarized as follows:

Assumption 1 *For* $\forall\Theta$, $F_\alpha(\Theta)$ *and* $F_\beta(\Theta)$ *are both circularly-symmetric Gaussian random variables [99] with the same variance, and they are statistically independent.*

Assumption 2 *For each dynamic scatterer, the angular spectrum components arriving from different directions are uncorrelated.*

Assumption 3 *For any two dynamic scatterers* $i_1,\ i_2 \in \Omega_d$, $\vec{E}_{i_1}(t_1, f)$ *and* $\vec{E}_{i_2}(t_2, f)$ *are uncorrelated, for* $\forall t_1,\ t_2$.

Assumption 1 is due to the fact that the angular spectrum is a result of many rays or bounces with random phases and thus it can be assumed that each orthogonal component of $\vec{F}(\Theta)$ tends to be Gaussian under the Central Limit Theorem. Assumption 2 is because that the angular spectrum components corresponding to different directions have taken very different multiple scattering paths and they can thus be assumed to be uncorrelated with each other. Assumption 3 results from the fact that the channel responses of two locations separated by at least half wavelength are statistically uncorrelated [23] [119], and the electric fields contributed by different scatterers can thus be assumed to be uncorrelated.

Under these three assumptions, $\vec{E}_i(t, f)$, $\forall i \in \Omega_d$ can be approximated as a stationary process in time. Define the temporal ACF of an electric field $\vec{E}(t, f)$ as

$$\rho_{\vec{E}}(\tau, f) = \frac{\langle \vec{E}(0, f), \vec{E}(\tau, f) \rangle}{\sqrt{\langle |\vec{E}(0, f)|^2 \rangle \langle |\vec{E}(\tau, f)|^2 \rangle}}, \tag{3.4}$$

where τ is the time lag, $\langle\ \rangle$ stands for the ensemble average over all realizations, $\langle \vec{X}, \vec{Y} \rangle$ denotes the inner product of $\vec{X}$ and $\vec{Y}$, i.e., $\langle \vec{X}, \vec{Y} \rangle \triangleq \langle \vec{X} \cdot \vec{Y}^* \rangle$ and * is the operator of complex conjugate and $\cdot$ is dot product, $|\vec{E}(t, f)|^2$ denotes the square

of the absolute value of the electric field. Since $\vec{E}(t,f)$ is assumed to be a stationary process, the denominator of 3.4 degenerates to $E^2(f)$ which stands for the power of the electric field, i.e., $E^2(f) = \langle|\vec{E}(t,f)|^2\rangle$, $\forall t$, and the ACF is merely a normalized counterpart of the auto-covariance function.

For the i-th scatterer with moving velocity $\vec{v}_i$, $\langle\vec{E}_i(0,f)\cdot\vec{E}_i^*(\tau,f)\rangle$ can be derived as [40]

$$\begin{aligned}
&\langle\vec{E}_i(0,f)\cdot\vec{E}_i^*(\tau,f)\rangle \\
=\ & \int_{4\pi}\int_{4\pi}\langle\vec{F}(\Theta_1)\cdot\vec{F}(\Theta_2)\rangle\exp(j\vec{k}_2\cdot\vec{v}_i\tau)\,\mathrm{d}\Theta_1\,\mathrm{d}\Theta_2 \\
=\ & \frac{E_i^2(f)}{4\pi}\int_{4\pi}\exp(jkv_i\tau\cos(\alpha_2))\mathrm{d}\Theta_2 \\
=\ & E_i^2(f)\frac{\sin(kv_i\tau)}{kv_i\tau},
\end{aligned} \tag{3.5}$$

where we define $\int_{4\pi} \triangleq \int_0^{2\pi}\int_0^{\pi}$ and $\mathrm{d}\Theta \triangleq \sin(\alpha)\,\mathrm{d}\alpha\,\mathrm{d}\beta$, and $E_i^2(f)$ is the power of $\vec{E}_i(t,f)$. With Assumption 3, the auto-covariance function of $\vec{E}_{Rx}(t,f)$ can be written as

$$\begin{aligned}
&\left\langle(\vec{E}_{Rx}(0,f)-\vec{E}_s(f))\cdot(\vec{E}_{Rx}^*(\tau,f)-\vec{E}_s^*(f))\right\rangle \\
=\ & \sum_{i\in\Omega_d}E_i^2(f)\frac{\sin(kv_i\tau)}{kv_i\tau},
\end{aligned} \tag{3.6}$$

and the corresponding ACF can thus be derived as

$$\rho_{\vec{E}_{Rx}}(\tau,f) = \frac{1}{\sum_{j\in\Omega_d}E_j^2(f)}\sum_{i\in\Omega_d}E_i^2(f)\frac{\sin(kv_i\tau)}{kv_i\tau}. \tag{3.7}$$

From 3.7, the ACF of $\vec{E}_{Rx}$ is actually a combination of the ACF of each moving scatterer weighted by their radiation power, and the moving direction of each dynamic scatterer does not play a role in the ACF. The importance of 3.7 lies in the

fact that the speed information of the dynamic scatterers is actually embedded in the ACF of the received electric field.

3.2 Theoretical Foundation and Design of WiSpeed

In this section, we introduce the theoretical foundation and the detailed design of WiSpeed.

3.2.1 Theoretical Foundations of WiSpeed

In the following, we have derived the ACF of the received electric field at the Rx, which depends on the speed of the dynamic scatterers. If all or most of the dynamic scatterers move at the same speed v, then the right-hand side of 3.7 would degenerate to $\rho_{\vec{E}_{Rx}}(\tau, f) = \frac{\sin(kv\tau)}{kv\tau}$, and it becomes very simple to estimate the common speed from the ACF. However, it is not easy to directly measure the electric field at the Rx and analyze its ACF. Instead, the power of the electric field can be viewed equivalent to the power of the channel response that can be measured by commercial WiFi devices. In this section, we will discuss the principle of WiSpeed that utilizes the ACF of the CSI power response for speed estimation.

Without loss of generality, we use the channel response of OFDM-based WiFi systems as an example. Let $X(t, f)$ and $Y(t, f)$ be the transmitted and received signals over a subcarrier with frequency f at time t. Then, the least-square estimator of the CSI for the subcarrier with frequency f measured at time t is

$H(t,f) = \frac{Y(t,f)}{X(t,f)}$ [28]. In practice, the obtained estimation of the CSI suffers from the synchronization errors, which mainly consists of channel frequency offset (CFO), sampling frequency offset (SFO) and symbol timing offset (STO) [23]. Although the WiFi receivers perform timing and frequency synchronization, the residual of these errors cannot be neglected. However, the impact of synchronization errors on the amplitude of CSI is insignificant and thus WiSpeed only exploits the amplitude information of the measured CSI.

We define the power response $G(t,f)$ as the square of the magnitude of CSI, which takes the form

$$G(t,f) \triangleq |H(t,f)|^2 = \|\vec{E}_{Rx}(t,f)\|^2 + \varepsilon(t,f), \tag{3.8}$$

where $\|\vec{E}\|^2$ denotes the total power of $\vec{E}$, and $\varepsilon(t,f)$ is assumed to be an additive noise due to the imperfect measurement of CSI.

The noise $\varepsilon(t,f)$ can be assumed to follow a normal distribution. To prove this, we collect a set of one-hour CSI data in a static indoor environment with the channel sampling rate $F_s = 30\,\text{Hz}$. The Q-Q plot of the normalized $G(t,f)$ and standard normal distribution for a given subcarrier is shown in Fig. 3.3(a), which shows that the distribution of the noise is very close to a normal distribution. To verify the whiteness of the noise, we also study the ACF of $G(t,f)$ that can be defined as [95] $\rho_G(\tau,f) = \frac{\gamma_G(\tau,f)}{\gamma_G(0,f)}$, where $\gamma_G(\tau,f)$ denotes the auto-covariance function, i.e., $\gamma_G(\tau,f) \triangleq \text{cov}(G(t,f), G(t-\tau,f))$. In practice, sample auto-covariance function $\hat{\gamma}_G(\tau,f)$ is used instead. If $\varepsilon(t,f)$ is white noise, the sample ACF $\hat{\rho}_G(\tau,f)$, for $\forall \tau \neq 0$, can be approximated by a normal random vari-

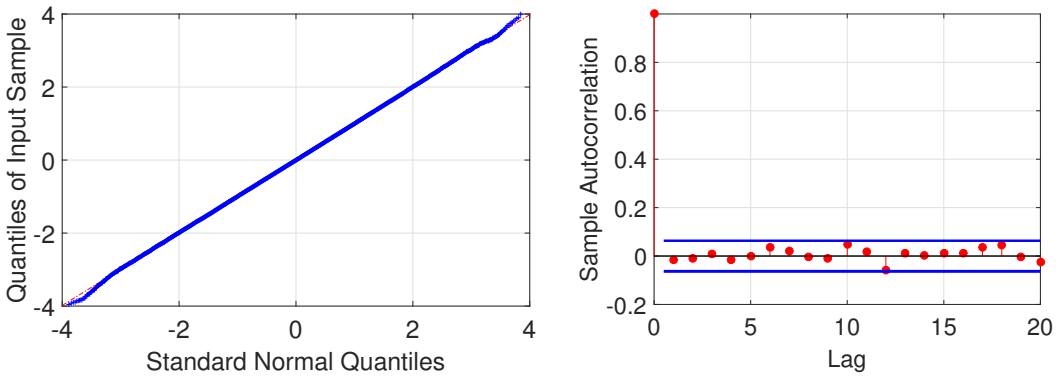

(a) Q-Q plot of noise.

(b) Sample ACF of noise.

Figure 3.3: The Q-Q plot and sample ACF of a typical CSI power response.

able with zero mean and standard deviation $\sigma_{\hat{\rho_G}(\tau,f)} = \frac{1}{\sqrt{T}}$. Fig. 3.3(b) shows the sample ACF of $G(t,f)$ when 2000 samples on the first subcarrier are used. As we can see from the figure, all the taps of the sample ACF are within the interval of $\pm 2\sigma_{\hat{\rho_G}(\tau,f)}$, and thus, it can be assumed that $\varepsilon(t,f)$ is an additive white Gaussian noise, i.e., $\varepsilon(t,f) \sim \mathcal{N}(0,\sigma^2(f))$.

In the previous analysis in Section 3.1, we assume that the Tx transmits continuous EM waves, but in practice the transmission time is limited. For example, in IEEE 802.11n WiFi systems operated in 5 GHz frequency band with 40 MHz bandwidth channels, a standard WiFi symbol is 4 μs, composed of a 3.2 μs useful symbol duration and a 0.8 μs guard interval. According to [101], for most office buildings, the delay spread is within the range of 40 to 70 ns, which is much smaller than the duration of a standard WiFi symbol. Therefore, we can assume continuous waves are transmitted in WiFi systems.

Based on the above assumptions and 3.2, 3.8 can be approximated as

$$
\begin{aligned}
G(t,f) &\approx \|\vec{E}_s(f) + \sum_{i\in\Omega_d} \vec{E}_i(t,f)\|^2 + \varepsilon(t,f) \\
&= \left\| \sum_{u\in\{x,y,z\}} \left(E_{su}(f)\hat{u} + \sum_{i\in\Omega_d} E_{iu}(t,f)\hat{u} \right) \right\|^2 + \varepsilon(t,f) \\
&= \sum_{u\in\{x,y,z\}} \left| E_{su}(f) + \sum_{i\in\Omega_d} E_{iu}(t,f) \right|^2 + \varepsilon(t,f) \\
&= \sum_{u\in\{x,y,z\}} \left(|E_{su}(f)|^2 + 2\mathrm{Re}\left\{ E^*_{su}(f) \sum_{i\in\Omega_d} E_{iu}(t,f) \right\} \right. \\
&\quad \left. + \left| \sum_{i\in\Omega_d} E_{iu}(t,f) \right|^2 \right) + \varepsilon(t,f), \qquad (3.9)
\end{aligned}
$$

where $\hat{x}$, $\hat{y}$ and $\hat{z}$ are unit vectors orthogonal to each other as shown in Fig. 3.2, $\mathrm{Re}\{\cdot\}$ denotes the operation of taking the real part of a complex number, and E_{iu} denotes the component of $\vec{E}_i$ in the u-axis direction, for $\forall u \in \{x,y,z\}$. Then, the auto-covariance function of $G(t,f)$ can be derived as

$$
\begin{aligned}
\gamma_G(\tau,f) &= \mathrm{cov}\left(G(t,f), G(t-\tau,f)\right) \\
&\approx \sum_{u\in\{x,y,z\}} \left(2|E_{su}(f)|^2 \sum_{i\in\Omega_d} \mathrm{cov}(E_{iu}(t,f), E_{iu}(t-\tau,f)) \right. \\
&\quad + \sum_{\substack{i_1,i_2\in\Omega_d \\ i_1\geq i_2}} \mathrm{cov}(E_{i_1u}(t,f), E_{i_1u}(t-\tau,f)) \cdot \\
&\quad \left. \mathrm{cov}(E_{i_2u}(t,f), E_{i_2u}(t-\tau,f)) \right) + \delta(\tau)\sigma^2(f), \qquad (3.10)
\end{aligned}
$$

where Assumptions 1-3 and 3.3 are applied to simplify the expression and the detailed derivations can be found in Appendix 3.6.1.

According to the relation between the auto-covariance and autocorrelation,

$\gamma_G(\tau,f)$ can be rewritten in the forms of ACFs of each scatterer as

$$\gamma_G(\tau,f) \approx \sum_{u\in\{x,y,z\}}\Bigg(\sum_{i\in\Omega_d}\frac{2|E_{su}(f)|^2E_i^2(f)}{3}\rho_{E_{iu}}(\tau,f) + \sum_{\substack{i_1,i_2\in\Omega_d\\ i_1\geq i_2}}\frac{E_{i_1}^2(f)E_{i_2}^2(f)}{9}\rho_{E_{i_1u}}(\tau,f)\rho_{E_{i_2u}}(\tau,f)\Bigg)+\delta(\tau)\sigma^2(f), \quad (3.11)$$

where the right-hand side is obtained by using the relation $E_{iu}^2(f)=\frac{E_i^2(f)}{3}$, $\forall u\in\{x,y,z\}$, $\forall i\in\Omega_d$ [40]. The corresponding ACF $\rho_G(\tau,f)$ of $G(t,f)$ is thus obtained by $\rho_G(\tau,f)=\frac{\gamma_G(\tau,f)}{\gamma_G(0,f)}$, where $\gamma_G(\tau,0)$ can be obtained by plugging $\rho_{E_{iu}}(0,f)=1$ into 3.11. When the moving directions of all the dynamic scatterers are approximately the same, then we can choose z-axis aligned with the common moving direction. Then, the closed forms of $\rho_{E_{iu}}(\tau,f)$, $\forall u\in\{x,y,z\}$, are derived under Assumptions 1-2 [40], i.e., for $\forall i\in\Omega_d$,

$$\begin{aligned}\rho_{E_{ix}}(\tau,f) &= \rho_{E_{iy}}(\tau,f)\\ &= \frac{3}{2}\left[\frac{\sin(kv_i\tau)}{kv_i\tau}-\frac{1}{(kv_i\tau)^2}\left(\frac{\sin(kv_i\tau)}{kv_i\tau}-\cos(kv_i\tau)\right)\right], \quad (3.12)\\ \rho_{E_{iz}}(\tau,f) &= \frac{3}{(kv_i\tau)^2}\left[\frac{\sin(kv_i\tau)}{kv_i\tau}-\cos(kv_i\tau)\right]. \quad (3.13)\end{aligned}$$

The theoretical spatial ACFs are shown in Fig. 3.4(a) where $d\triangleq v_i\tau$. As we can see from Fig. 3.4(a), the magnitudes of all the ACFs decay with oscillations as the distance d increases.

For a WiFi system with a bandwidth of 40 MHz and a carrier frequency of 5.805 GHz, the difference in the wavenumber k of each subcarrier can be neglected, e.g., $k_{\max}=122.00$ and $k_{\min}=121.16$. Then, we can assume $\rho(\tau,f)\approx\rho(\tau)$, $\forall f$. Thus, we can improve the sample ACF by averaging across all subcarri-

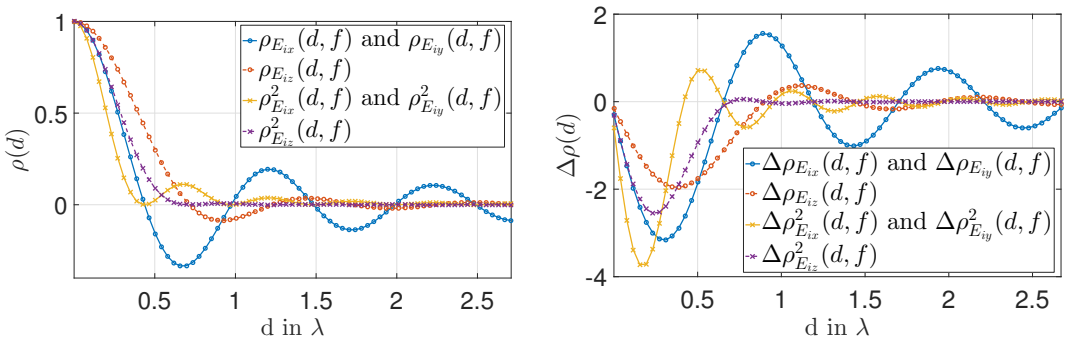

(a) Theoretical spatial ACFs.

(b) Diff. of spatial ACFs.

Figure 3.4: Theoretical spatial ACF for different orthogonal components of EM waves.

ers, i.e., $\hat{\rho}_G(\tau) \triangleq \frac{1}{F}\sum_{f\in\mathcal{F}}\hat{\rho}_G(\tau,f)$, where $\mathcal{F}$ denotes the set of all the available subcarriers and F is the total number of subcarriers. When all the dynamic scatterers have the same speed, i.e., $v_i = v$ for $\forall i \in \Omega_d$, which is the case for monitoring the motion for a single human subject, by defining the substitutions $E^2_{su} \triangleq \frac{2}{F}\sum_{f\in\mathcal{F}}|E_{su}(f)|^2$, $E^2_d \triangleq \frac{1}{3F}\sum_{i\in\Omega_d}\sum_{f\in\mathcal{F}}E^2_i(f)$, $\hat{\rho}_G(\tau)$ can be further approximated as (for $\tau \neq 0$)

$$\hat{\rho}_G(\tau) \approx C \sum_{u\in\{x,y,z\}} \left(E^2_d \hat{\rho}^2_{E_{iu}}(\tau) + E^2_{su}\hat{\rho}_{E_{iu}}(\tau) \right), \tag{3.14}$$

where C is a scaling factor and the variance of each subcarrier is assumed to be close to each other.

From 3.14, we observe that $\rho_G(\tau)$ is a weighted combination of $\rho_{E_{iu}}(\tau)$ and $\rho^2_{E_{iu}}(\tau)$, $\forall u \in \{x,y,z\}$. The left-hand side of 3.14 can be estimated from CSI and the speed is embedded in each term on the right-hand side. If we can separate one term from the others on the right-hand side of 3.14, then the speed can be estimated.

Taking the differential of all the theoretical spatial ACFs as shown in Fig. 3.4(b) where we use the notation $\Delta\rho(\tau)$ to denote $\frac{\mathrm{d}\rho(\tau)}{\mathrm{d}\tau}$, we find that although the ACFs of different components of the received EM waves are superimposed, the first local peak of $\Delta\rho^2_{E_{iu}}(\tau)$, $\forall u \in \{x, y\}$, happens to be the first local peak of $\Delta\rho_G(\tau)$ as well. Therefore, the component $\rho^2_{E_{iu}}(\tau)$ can be recognized from $\rho_G(\tau)$, and the speed information can thus be obtained by localizing the first local peak of $\Delta\hat{\rho}_G(\tau)$, which is the most important feature that WiSpeed extracts from the noisy CSI measurements.

To verify 3.14, we build a prototype of WiSpeed with commercial WiFi devices. The configurations of the prototype are summarized as follows: both WiFi devices operate on WLAN channel 161 with a center frequency of $f_c = 5.805\,\mathrm{GHz}$, and the bandwidth is 40 MHz; the Tx is equipped with a commercial WiFi chip and two omnidirectional antennas, while the Rx is equipped with three omnidirectional antennas and uses Intel Ultimate N WiFi Link 5300 with modified firmware and driver [38]. The Tx sends sounding frames with a channel sampling rate F_s of 1500 Hz, and CSI is obtained at the Rx. The transmission power is configured as 20 dBm.

All experiments in this chapter are conducted in a typical indoor office environment as shown in Fig. 3.5. In each experiment, the LOS path between the Tx and the Rx is blocked by at least one wall, resulting in a severe NLOS condition. More specifically, we investigate two cases:

1. **The Tx is in motion and the Rx remains static:** The Tx is attached to a

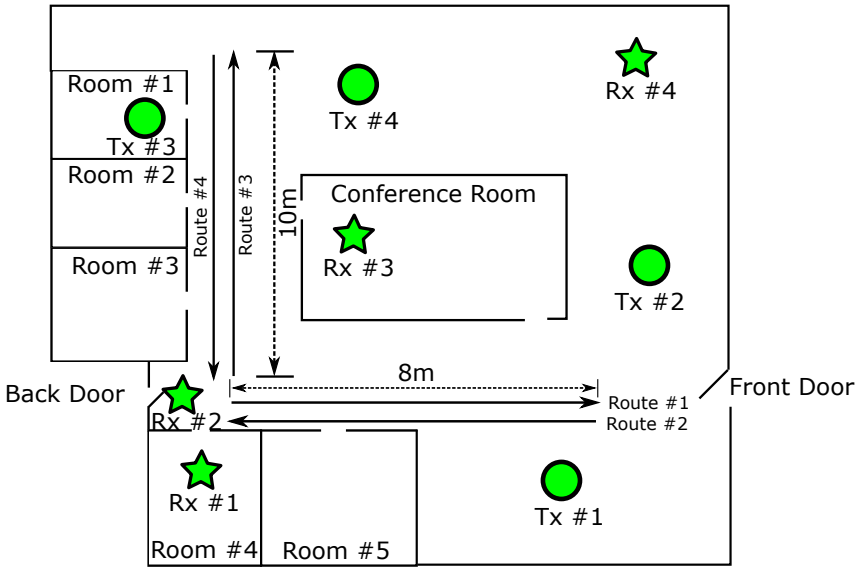

Figure 3.5: Experimental settings in a typical office environment with different Tx/Rx locations and walking routes.

cart and the Rx is placed at Location Rx #1 as shown in Fig. 3.5. The cart is pushed forward at an almost constant speed along Route #1 marked in Fig. 3.5 from $t = 3.7\,\mathrm{s}$ to $t = 14.3\,\mathrm{s}$.

2. **Both the Tx and the Rx remain static and a person passes by:** the Tx and Rx are placed at Location Tx #1 and Rx #1 respectively. A person walks along Route #1 at a speed similar to Case (1) from $t = 4.9\,\mathrm{s}$ to $t = 16.2\,\mathrm{s}$.

Since the theoretical approximations are only valid under the short duration assumption, we set the maximum time lag τ as $0.2\,\mathrm{s}$. In both cases, we compute the sample ACF $\hat{\rho}_G(\tau)$ every $0.05\,\mathrm{s}$.

Fig. 3.6 demonstrates the sample ACFs for the two cases. In particular, Fig. 3.6(a) visualizes the sample ACF corresponding to a snapshot of Fig. 3.6(e) for different subcarriers given a fixed time t with the time lag $\tau \in [0, 0.2s]$, and

Fig. 3.6(c) shows the average ACF $\hat{\rho}_G(\tau)$, which is much less noisy compared with individual $\hat{\rho}_G(\tau, f)$. In this case, the Tx can be regarded as a moving scatterer with a dominant radiation power compared with the other scatterers, giving rise to the dominance of $E_d^2\rho_{E_{iu}}^2(\tau)$, $u \in \{x, y, z\}$ over the other components in 3.14. Additionally, $\rho_{E_{iz}}^2(\tau)$ decays much faster than $\rho_{E_{ix}}^2(\tau)$ and $\rho_{E_{iy}}^2(\tau)$, and $\rho_{E_{ix}}^2(\tau) = \rho_{E_{iy}}^2(\tau)$. Thus, a similar pattern between $\hat{\rho}_G(\tau)$ and $\rho_{E_{ix}}^2(\tau)$ ($\rho_{E_{iy}}^2(\tau)$) can be observed with a common and dominant component $\frac{\sin^2(kv\tau)}{(kv\tau)^2}$, where v is the speed of the cart and the person. The experimental result illustrated in Fig. 3.6(c) matches well with the theoretical analysis in the sense that only the component $\rho_{E_{ix}}^2(\tau)$ dominates the obtained ACF estimation and the impacts of the other components can be neglected.

Similarly, for Case (2), Fig. 3.6(b) shows the sample ACF $\hat{\rho}_G(\tau, f)$ for different subcarriers and Fig. 3.6(d) shows the average sample ACF $\hat{\rho}_G(\tau)$, which is a snapshot of Fig. 3.6(f) given a fixed time t with the time lag $\tau = [0, 0.2s]$. Clearly, the pattern of the component $\rho_{E_{iu}}^2(\tau)$, $u \in \{x, y\}$, in the sample ACF is much less pronounced than Case (1) shown in Fig. 3.6(c) and Fig. 3.6(e). This can be justified by the fact that the radiation power E_d^2 is much smaller than that in Case (1), as the set of dynamic scatterers only consists of different parts of a human body in mobility. Consequently, the shape of $\hat{\rho}_G(\tau)$ resembles more closely to $\rho_{E_{iu}}(\tau)$, $\forall u \in \{x, y, z\}$ with a dominant component $\frac{\sin(kv\tau)}{kv\tau}$. Note that the component $\frac{\sin(kv\tau)}{kv\tau}$ oscillates two times slower than the component $\frac{\sin^2(kv\tau)}{(kv\tau)^2}$ does. From Fig. 3.6(d), we can observe that the obtained ACF is a result of a weighted sum of these two components. We also observe that the slow-varying trend of the ACF follows the

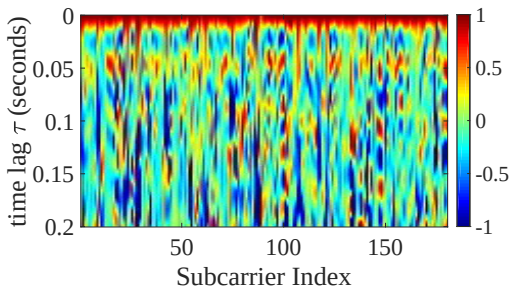

(a) ACF measured by different subcarriers for a moving Tx.

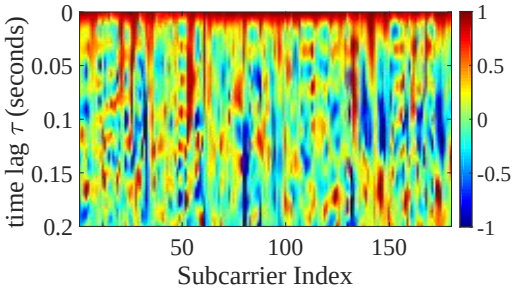

(b) ACF measured by different subcarriers for a walking human.

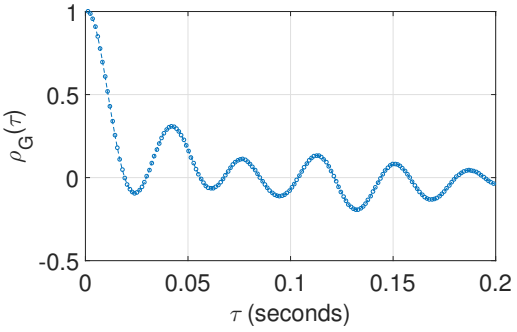

(c) Snapshot of ACF for a moving Tx.

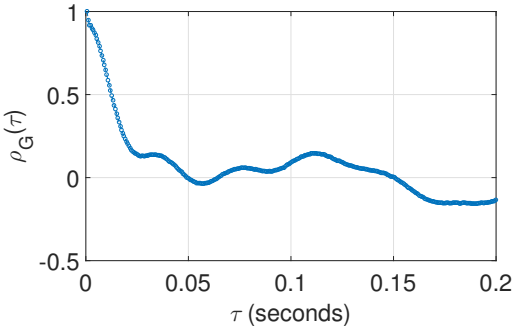

(d) Snapshot of ACF for a walking human.

shape of the component $\frac{\sin(kv\tau)}{kv\tau}$ and the component $\frac{\sin^2(kv\tau)}{(kv\tau)^2}$ is only embedded in the trend, the weight of $\frac{\sin(kv\tau)}{kv\tau}$ should be larger than that of $\frac{\sin^2(kv\tau)}{(kv\tau)^2}$. Note that the embedded component $\frac{\sin^2(kv\tau)}{(kv\tau)^2}$ has a similar pattern compared with Case (1) since the moving speeds in the two experiments are similar to each other.

3.2.2 Design of WiSpeed

Based on the theoretical results derived above, we propose WiSpeed, which integrates three modules: moving speed estimator, acceleration estimator, and gait cycle estimator. The moving speed estimator is the core module of WiSpeed, while the other two extract useful features from the moving speed estimator to

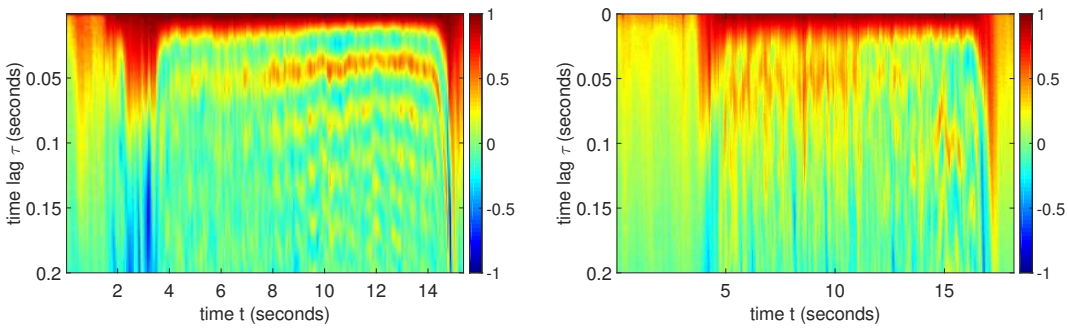

(e) ACF matrix for a moving Tx.

(f) ACF matrix for a walking human.

Figure 3.6: ACFs for the two scenarios.

detect falling down and to estimate the gait cycle of a walking person.

3.2.2.1 Moving Speed Estimator

WiSpeed estimates the moving speed of the subject by calculating the sample ACF $\Delta\hat{\rho}_G(\tau)$ from CSI measurements, localizing the first local peak of $\Delta\hat{\rho}_G(\tau)$, and mapping the peak location to the speed estimation. Since in general, the sample ACF $\Delta\hat{\rho}_G(\tau)$ is noisy as can be seen in Fig. 3.6(e) and Fig 3.6(f), we develop a novel robust local peak identification algorithm based on the idea of local regression [29] to reliably detect the location of the first local peak of $\Delta\hat{\rho}_G(\tau)$.

For notational convenience, write the discrete signal for local peak detection as $y[n]$, and our goal is to identify the local peaks in $y[n]$. First of all, we apply a moving window with length $2L+1$ to $y[n]$, where L is chosen to be comparable with the width of the desired local peaks. Then, for each window with its center located at n, we verify if there exists any potential local peak within the window by performing a linear regression and a quadratic regression to the

data inside the window, separately. Let SSE denote the sum of squared errors for the quadratic regression and SSE_r denote that for the linear regression. If there is no local peak within the given window, the ratio $\alpha[n] \triangleq \frac{(\text{SSE}_r - \text{SSE})/(3-2)}{\text{SSE}/(2\text{L}+1-3)}$ can be interpreted as a measure of the likelihood of the presence of a peak within the window, and has a central F-distribution with 1 and $2(L-1)$ degrees of freedom, under certain assumptions [87]. We choose a potential window with the center point n only when $\alpha[n]$ is larger than a preset threshold η, which is determined by the desired probability of finding a false peak, and $\alpha[n]$ should also be larger than its neighborhoods $\alpha[n-L]$,...,$\alpha[n+L]$. When L is small enough and there exists only one local peak within the window, the location of the local peak can be directly obtained from the fitted quadratic curve.

We use a numerical example in the following to verify the effectiveness of the proposed local peak identification algorithm. Let $y(t) = \cos(2\pi f_1 t + 0.2\pi) + \cos(2\pi f_2 t + 0.3\pi) + n(t)$, where we set $f_1 = 1\,\text{Hz}$, $f_2 = 2.5\,\text{Hz}$, and $n(t) \sim \mathcal{N}(0, \sigma^2)$ is additive white Gaussian noise with zero mean and variance σ^2. The signal $y(t)$ is sampled at a rate of 100 Hz from time $t = 0\,\text{s}$ to $t = 1\,\text{s}$. When the noise is absent, the true locations of the two local peaks are $t_1 \approx 0.331\,\text{s}$ and $t_2 \approx 0.760\,\text{s}$ and the estimates of our proposed local peak identification algorithm are $\hat{t}_1 \approx 0.327\,\text{s}$ and $\hat{t}_2 \approx 0.763\,\text{s}$, as shown in Fig. 3.7(a). When the noise is present and σ is set to 0.2, the estimates are $\hat{t}_1 \approx 0.336\,\text{s}$ and $\hat{t}_2 \approx 0.762\,\text{s}$, as shown in Fig. 3.7(b). As we can see from the results, the estimated locations of the local peaks are very close to those of the actual peaks even when the signal is corrupted with the noise, which shows the effectiveness of the proposed local peak identification algorithm.

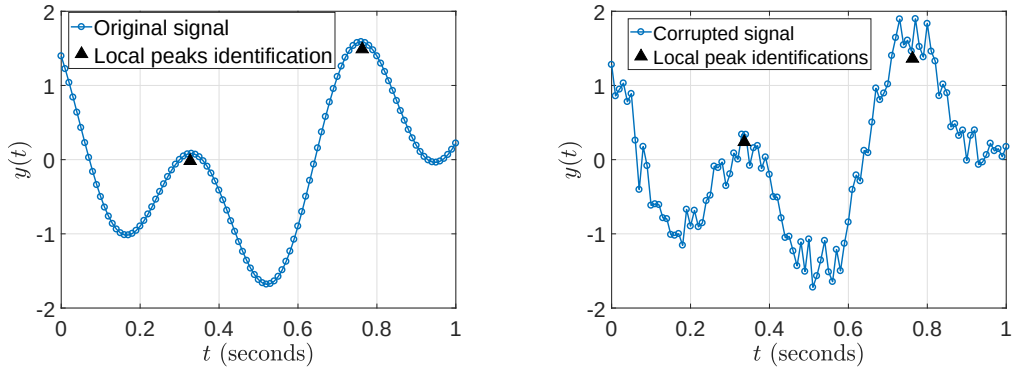

(a) Original signal and its estimated local peaks.

(b) Corrupted signal and its estimated local peaks.

Figure 3.7: An illustration of the peak identification algorithm.

Then, the speed of the moving object can be estimated as $\hat{v} = \frac{d_1}{\hat{\tau}}$, where d_1 is the distance between the first local peak of $\Delta\rho^2_{E_{ix}}(d)$ and the origin, and $\hat{\tau}$ is the location of the first local peak of $\Delta\hat{\rho}_G(\tau)$. The distance d_1 can be obtained by solving the equation

$$\frac{\partial^2}{\partial d^2}\rho^2_{E_{ix}}(d, f) = 0, \tag{3.15}$$

where $\rho_{E_{ix}}(d, f)$ denotes the theoretical spatial ACF as shown in Fig. 3.4(a). As 3.15 does not have a closed-form solution, we evaluate the second smallest root of 3.15 numerically which leads to about 0.54λ. A median filter is then applied to the speed estimates to remove the outliers. The proposed speed estimator is summarized in Algorithm 1.

3.2.2.2 Acceleration Estimator

Acceleration can be calculated from $\hat{v}$ obtained above. One intuitive method of acceleration estimation is to take the difference of two adjacent speed estimates

Algorithm 1 The proposed speed estimator

Input: T consecutive CSI measurements before time t: $H(s,f)$, $s = t - \frac{T-1}{F_s}, ..., t - \frac{1}{F_s}, t$, and $f \in \mathcal{F}$;

Output: Speed estimation at t: $\hat{v}(t)$.

1: Calculate the CSI power response: $G(s,f) \leftarrow |H(s,f)|^2$;

2: Calculate the ACF of each subcarrier f: $\hat{\rho}_G(\tau, f) \leftarrow \frac{1}{T}\sum_{s=t-\frac{T-1}{F_s}+\tau}^{t}\Big(G(s-\tau,f) - \bar{G}(f)\Big)\Big(G(s,f) - \bar{G}(f)\Big)$, where $\bar{G}(f)$ is the sample mean;

3: Aggregate ACF across all the subcarriers: $\hat{\rho}_G(\tau) \leftarrow \frac{1}{F}\sum_{f\in\mathcal{F}}\hat{\rho}_G(\tau, f)$;

4: Calculate the differential ACF: $\Delta\hat{\rho}_G(\tau) \leftarrow \hat{\rho}_G(\tau) - \hat{\rho}_G(\tau - \frac{1}{F_s})$;

5: Apply the proposed peak identification algorithm to estimate the location of the first local peak of $\Delta\hat{\rho}_G(\tau)$: $\hat{\tau}$;

6: Speed estimation at time t: $\hat{v}(t) \leftarrow \frac{0.54\lambda}{\hat{\tau}}$.

and then divide the difference of the speeds by the difference of their measurement time. However, this scheme is not robust as it is likely to magnify the estimation noise. Instead, we leverage the fact that the acceleration values can be approximated as a piecewise linear function as long as there are enough speed estimates within a short duration. ℓ_1 trend filter produces trend estimates that are smooth in the sense of being piecewise linear [49] and is well suited to our purpose. Thus, we adopt an ℓ_1 trend filter to extract the piecewise linear trend embedded in the speed estimation and then, estimate the accelerations by taking differential of the smoothed speed estimation.

Mathematically, let $\hat{v}[n]$ denote $\hat{v}(n\Delta T)$, where ΔT is the interval between two estimates, and let $\tilde{v}[n]$ denote the smoothed one. Then, $\tilde{v}[n]$ is obtained by solving the following unconstrained optimization problem:

$$\min_{\tilde{v}[n],\forall n} \sum_{n=1}^{N} (\tilde{v}[n]-\hat{v}[n])^2 + \lambda \sum_{n=2}^{N-1} \Big| \tilde{v}[n-1]-2\tilde{v}[n]+\tilde{v}[n+1] \Big|, \tag{3.16}$$

where $\lambda \geq 0$ is the regularization parameter used to control the trade-off between smoothness of $\tilde{v}[n]$ and the size of the residual $|\tilde{v}[n]-\hat{v}[n]|$, and N denotes the size of the speed estimates that need to be smoothed. Then, we obtain the acceleration estimation as $\hat{a}[n] = \frac{(\tilde{v}[n]-\tilde{v}[n-1])}{\Delta T}$. As shown in [49], the complexity of the ℓ_1 filter grows linearly with the length of the data N and can be calculated in real-time on most platforms.

3.2.2.3 Gait Cycle Estimator

When the estimated speed is within a certain range, e.g., from 1 m/s to 2 m/s, and the acceleration estimates are small, then WiSpeed starts to estimate the corresponding gait cycle. In fact, the process for walking a single step can be decomposed into three stages: lifting one leg off the ground, using the lifted leg to contact with the ground and pushing the body forward, and keeping still for a short period of time before the next step. The same procedure is repeated until the destination is reached.

In terms of speed, one cycle of walking consists of an acceleration stage followed by a deceleration stage. WiSpeed leverages the periodic pattern of speed changes for gait cycle estimation. More specifically, WiSpeed extracts the local peaks in the speed estimates corresponding to the moments with the largest speeds. To achieve peak localization, we use the persistence-based scheme presented in [53] to formulate multiple pairs of local maximum and local minimum, and the locations of the local maximum are considered as the peak locations. The time interval between every two adjacent peaks is computed as a gait cycle. Meanwhile, the moving distance between every two adjacent peaks is calculated as the estimation of the stride length.

3.3 Experimental Evaluation

In this section, we first introduce the indoor environment and system setups of the experiments. Then, the performance of WiSpeed is evaluated in two

applications: human walking monitoring and human fall detection.

3.3.1 Environment

We conduct extensive experiments in a typical office environment, with floorplan shown in Fig. 3.5. The indoor space is occupied by desks, computers, shelves, chairs, and household appliances. The same WiFi devices as introduced in Section 3.2 are used during the experiments.

3.3.2 Experimental Settings

Two sets of experiments are performed. In the first set of experiments, we study the performance of WiSpeed in estimating the human walking speed. For device-free scenarios, it shows that the number of steps and stride length can also be estimated besides the walking speed. Estimation accuracy is used as the metric which compares the estimated walking distances with the ground-truth distances, since measuring walking distance is much easier and more accurate than measuring the speed directly. Different routes and locations of the devices are tested and the details of experiment setup are summarized in Tab. 3.1 and Tab. 3.2. In the second set of experiments, we investigate the performance of WiSpeed as a human activity monitoring scheme. Two participants are asked to perform different activities, including standing up, sitting down, picking up things from the ground, walking, and falling down.

Table 3.1: Exp. settings for device-free human walking monitoring

Config. / Setting	Tx loc.	Rx loc.	Route index
Setting #1	Tx #1	Rx #1	Route #1/#2
Setting #2	Tx #1	Rx #2	Route #1/#2
Setting #3	Tx #2	Rx #1	Route #1/#2
Setting #4	Tx #3	Rx #2	Route #3/#4
Setting #5	Tx #4	Rx #2	Route #3/#4
Setting #6	Tx #3	Rx #3	Route #3/#4

Table 3.2: Exp. settings for device-based speed monitoring

Config. / Setting	Tx loc.	Rx loc.	Route index
Setting #7	moving	Rx #1	Route #1/#2
Setting #8	moving	Rx #4	Route #1/#2
Setting #9	moving	Rx #1	Route #3/#4
Setting #10	moving	Rx #4	Route #3/#4

3.3.3 Human Walking Monitoring

Fig. 3.8 visualizes one of the experimental results under Setting #1 of Route #1, i.e., both the Tx and Rx are static and one experimenter walks along the specified route. Fig. 3.8a–c show three snapshots of estimated ACFs at different time instances marked in Fig. 3.8d. From Fig. 3.8, we can conclude that although the ACFs are very different, the locations of the first local peak of $\Delta\hat{\rho}_G(\tau)$ are highly consistent as long as the ACFs are calculated under similar walking speeds.

Fig. 3.8d shows the results of walking speed estimation for the experiment, and we can see a very clear pattern of walking due to the acceleration and deceleration. The corresponding stride length estimation is shown in Fig. 3.8e. The estimated walking distance is 8.46 m and it is within 5.75% of the ground-truth distance of 8 m. On the other hand, the average stride length is 0.7 m and very close to the average walking stride length of the participants.

Fig. 3.9 shows two typical speed estimation results both under Setting #7 of Route #1 where the Tx is attached to a cart and one experimenter pushes the cart along the specified route. The cart moves at different speeds for these two realizations, and Fig. 3.9(a) and Fig. 3.9(b) show the corresponding speed estimates, respectively. As we can see from the estimated speed patterns, there are no periodic patterns like the device-free walking speed estimates as in Fig. 3.8d. This is because when the Tx is moving, the energy of the EM waves reflected by the human body is dominated by that radiated by the transmit antennas and WiSpeed can only estimate the speed of moving antennas. The estimated moving distance

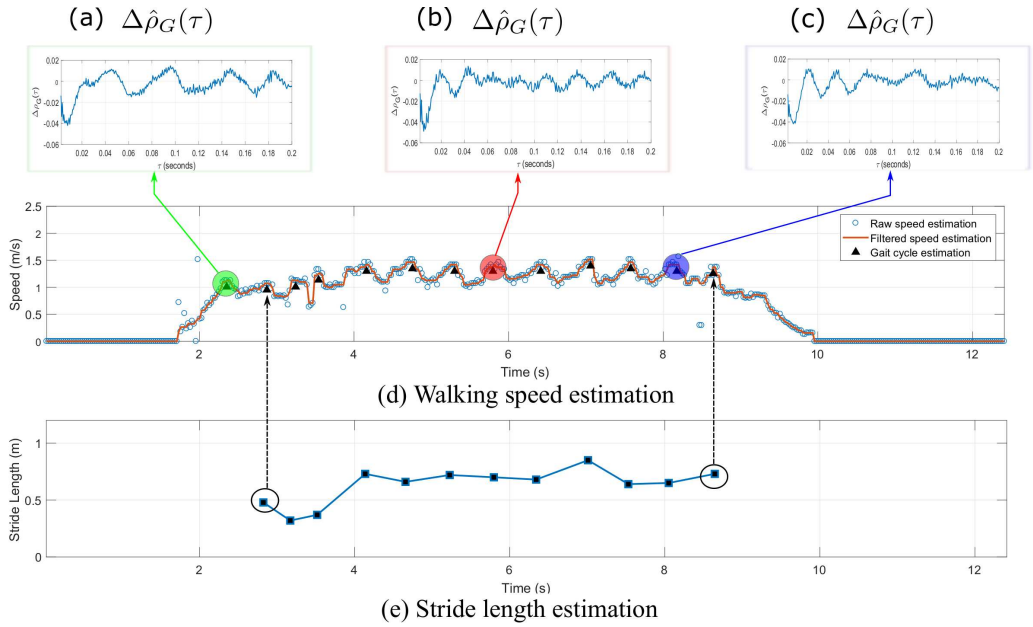

Figure 3.8: Experimental results for human walking monitoring under Setting #1 and Route #1.

for the case that Tx moves at a higher speed is 8.26 m and the other one is 8.16 m, where the ground-truth distance is 8 m. Note that the speed estimators, proposed in [135] and [136], can also obtain the similar results under the same condition, however, they cannot work for device-free scenarios.

Fig. 3.10 summarizes the accuracy of the 200 experiments of human walk-

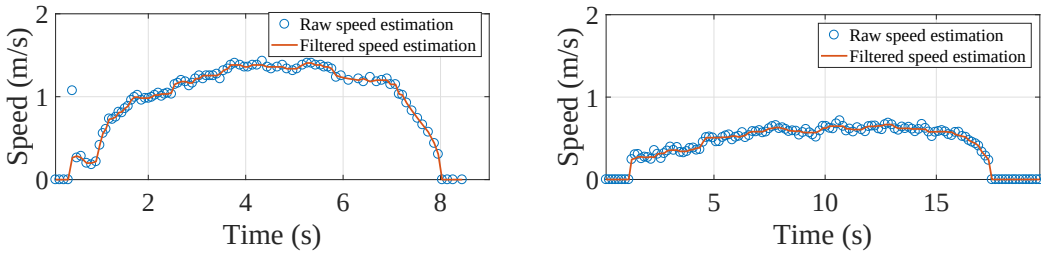

(a) Tx moves at a higher speed. (b) Tx moves at a lower speed.

Figure 3.9: Speed estimation for a moving Tx.

ing speed estimation. More specifically, Fig. 3.10(a) shows the error distribution for Setting #1 – #6, and Fig. 3.10(b) demonstrates the corresponding error distribution for Route #1 – #4; Fig. 3.10(c) shows the error distribution for Setting #7 – #10, and Fig. 3.10(d) demonstrates the corresponding error distribution for Route #1 – #4. The bottom and top error bars stand for the 5% percentiles and 95% percentiles of the estimates, respectively, and the middle of point is the sample mean of the estimates. The ground-truths for Routes #1–#4 are shown in Fig. 3.5. From the results, we find that (i) WiSpeed performs consistently for different Tx/Rx locations, routes, subjects, and walking speeds, indicating the robustness of WiSpeed under various scenarios, and (ii) WiSpeed tends to overestimate the moving distances under device-free settings. This is because we use the route distances as baselines and ignore the displacement of the subjects in the direction of gravity. Since WiSpeed measures the absolute moving distance of the subject in the coverage area, the motion in the gravity direction would introduce a bias into the distance estimation.

In summary, WiSpeed achieves a MAPE of 4.85% for device-free human walking speed estimation and 4.62% for device-based speed estimation, which outperforms the existing approaches, even with only a single pair of WiFi devices and in severe NLOS conditions. Note that WiDar [78] can achieve a median speed error of 13%, however, they require multiple pairs of WiFi devices and strong line-of-sight operating condition, i.e., the object being tracked should be within the fields of vision of both the transmitters and receivers.

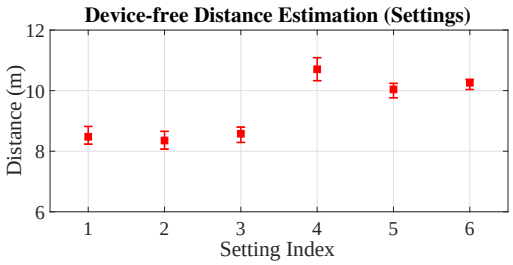

(a) Estimation results for Setting #1 – #6.

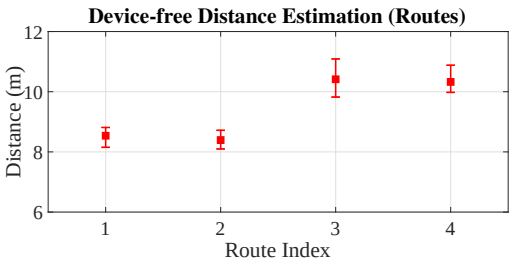

(b) Estimation results for Route #1 – #4.

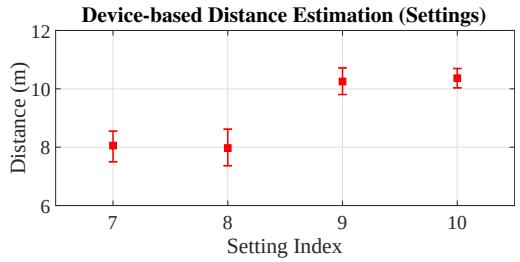

(c) Estimation results for Setting #7 – #10.

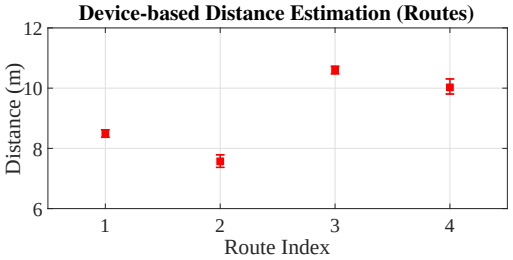

(d) Estimation results for Route #1 – #4.

Figure 3.10: Error distribution of distance distance estimates under different conditions.

3.3.4 Human Fall Detection

In this subsection, we show that WiSpeed can differentiate falling down from other normal daily activities. We collect a total of five sets of data: (i) falling to the ground, (ii) standing up from a chair, (iii) sitting down on a chair, and (iv) bowing and picking up items from the ground, (v) walking inside the room. Each experiment lasts for 8 s. We collect 20 datasets of the falling down activity from two subjects, and 10 datasets for each of the other four activities from the same two subjects. The experiments are conducted in Room #5, and the WiFi Tx and Rx are placed at Location Tx #1 and Rx #2 as shown in Fig. 3.5. Fig. 3.11 shows a snapshot of speed and acceleration estimation results for different activities and

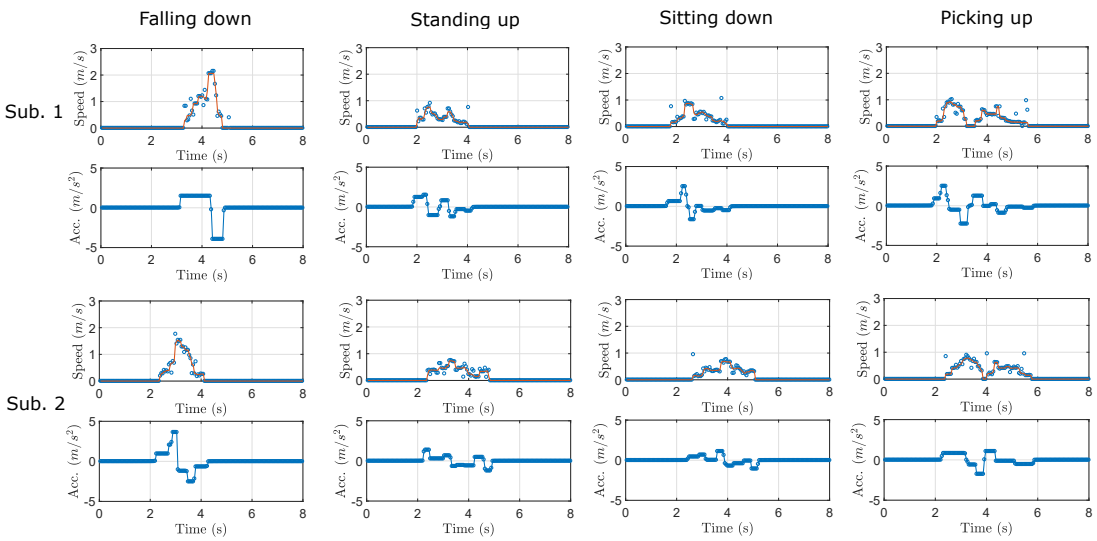

Figure 3.11: Speed and Acceleration for different activities and subjects.

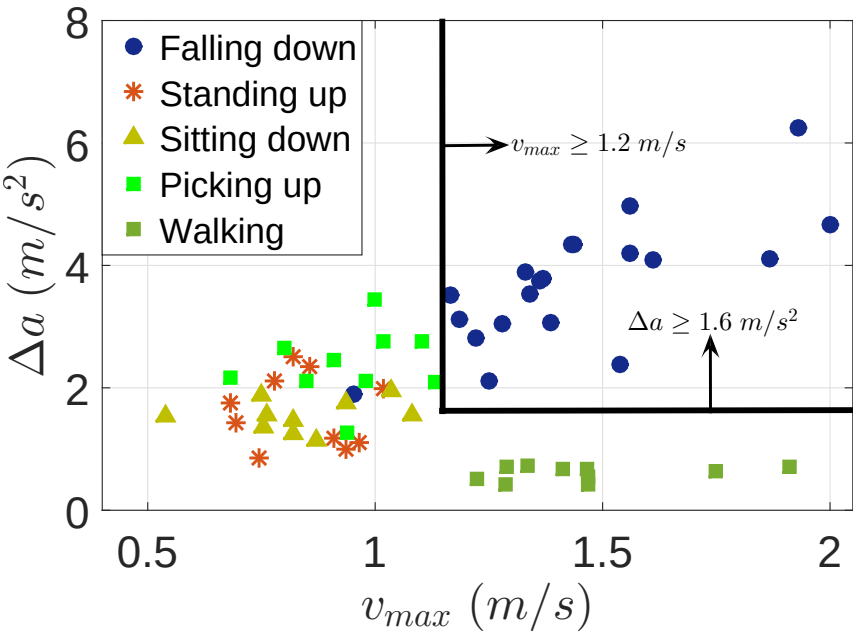

Figure 3.12: Distribution of the two metrics for all the activities.

subjects.

Realizing that the duration of a real-world falling down can be as short as 0.5s and the human body would experience a sudden acceleration and then

a deceleration [14], we propose two metrics for falling down detection: (i) the maximum change in acceleration within 0.5 s, denoted as Δa, and (ii) the maximum speed during the period of the maximum change of acceleration, written as $v_{\max}$. Fig. 3.12 shows the distribution of $(\Delta a, v_{\max})$ of all activities from the two subjects. Obviously, by setting two thresholds: $\Delta a \geq 1.6\, m/s^2$ and $v_{\max} \geq 1.2\, m/s$, WiSpeed could differentiate falls from the other four activities except one outlier, leading to a detection rate of 95% and zero false alarm, while [114] requires machine learning techniques. This is because WiSpeed extracts the most important physical features for activity classification, namely, the speed and the change of acceleration, while [114] infers these two physical values indirectly.

3.4 Discussion

In this section, we discuss the system parameter selections for different applications and their impact on the computational complexity of WiSpeed, and the behavior of WiSpeed when multiple objects are present.

3.4.1 Tracking a Fast Moving Object

In order to track fast speed-varying object, we adopt the following equation with a reduced number of samples to calculate the sample auto-covariance function:

$$\hat{\gamma}_G(\tau, f) = \frac{1}{M} \sum_{t=T-M+1}^{T} \Big(G(t-\tau, f) - \bar{G}(f)\Big)\Big(G(t, f) - \bar{G}(f)\Big), \tag{3.17}$$

where T is the length of the window, M is the number of samples for averaging, and $\bar{G}(f)$ is the sample average. 3.17 shows that to estimate a moving subject with speed v, WiSpeed requires a time window with a duration $T_0 = \frac{0.54\lambda}{v} + \frac{M}{F_s}$ seconds. Essentially, WiSpeed captures the average speed of motion in a period of time rather than the instantaneous moving speed. For instance, with $v = 1.3\,m/s$, $F_s = 1500\,\text{Hz}$, $f_c = 5.805\,\text{GHz}$, and $M = 100$, T_0 is around 0.12 s. In case that the speed changes significantly within a duration of T_0, the performance of WiSpeed would degrade. To track the speed of a fast-varying moving subject, a smaller T_0 is desirable, which can be achieved by increasing the channel sampling rate F_s or increasing the carrier frequency to reduce the wavelength λ.

3.4.2 Computational Complexity

The main computational complexity of WiSpeed comes from the estimation of the overall ACF $\hat{\rho}_G(\tau)$, giving rise to a total of FMT_0F_s multiplications where F is the number of available subcarriers. For motions with slow-varying speeds such as walking and standing up, a lower channel sampling rate suffices which could reduce the complexity. For example, in our experiments of human walking speed estimation and human fall detection, $F_s = 1500\,\text{Hz}$, $f_c = 5.805\,\text{GHz}$, $F = 180$, and $M = 100$, the total number of multiplications for WiSpeed to produce one output is around 3 million. This leads to a computational time of 80.4 ms on a desktop with Intel Core i7-7500U processor and 16GB memory, which is short enough for real-time applications.

3.4.3 Impact of Multiple Moving Objects

WiSpeed is designed to estimate the speed of a single moving object in the environment. If there exist multiple moving objects within the coverage of WiSpeed, WiSpeed would capture the highest speed among the objects. This is because WiSpeed uses the first local peak of the obtained ACF differential to estimate the speed and the component of ACF contributed by the object with the highest moving speed has the closest peak to the origin.

An experiment is conducted to illustrate the conjecture. Under Setting #4 as described in Section 3.3.2, two subjects first walk along Route #3, and then, they turn around at the same time and repeat the process along Route #4. For each Route, Subject #1 walks with a lower speed and starts to walk earlier than Subject #2, and Subject #2 walks with a higher speed and stops earlier than Subject #1. Fig. 3.13 shows that WiSpeed first captures the walking speed of Subject #1 while Subject #2 keeps static, and then, it captures the speed of Subject #2 when the speed of Subject #2 exceeds that of Subject #1.

One potential solution for detecting the speeds of multiple moving objects is to deploy multiple transmission pairs of WiSpeed. The coverage of each pair can be tuned by varying the distance between the transmitter and receiver. The environment can thus be divided into multiple small regions and it is reasonable to assume that there is only a single person within each small region.

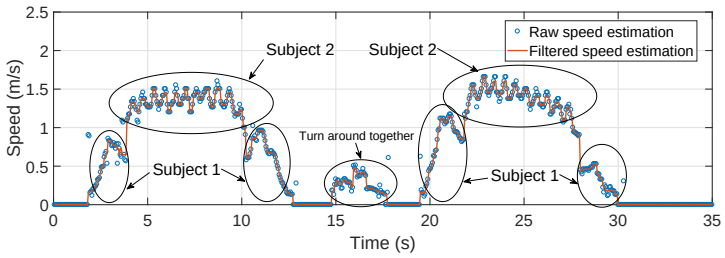

Figure 3.13: Two subjects walking in the environment.

3.5 Summary

In this chapter, we propose WiSpeed, a universal indoor speed estimation system for human motions leveraging commercial WiFi, which can estimate the speed of a moving object under either device-free or device-based condition. WiSpeed is built upon the statistical theory of EM waves which quantifies the impact of human motions on EM waves for indoor environments. We conduct extensive experiments in a typical indoor environment which demonstrates that WiSpeed can achieve a MAPE of 4.85% for device-free human walking speed monitoring and a MAPE of 4.62% for device-based speed estimation. Meanwhile, it achieves an average detection rate of 95% with no false alarms for human fall detection. Due to its large coverage, robustness, low cost, and low computational complexity, WiSpeed is a very promising candidate for indoor passive human activity monitoring systems.

3.6 Appendix

3.6.1 Derivation of 3.10

First, we can rewrite $G(t,f)$ as

$$G(t,f) = \sum_{u\in\{x,y,z\}} G_u(t,f) + \varepsilon(t,f), \tag{3.18}$$

where $G_u(t,f) \triangleq |E_{su}(f)|^2 + 2\mathrm{Re}\left\{E^*_{su}(f)\sum_{i\in\Omega_d} E_{iu}(t,f)\right\} + \left|\sum_{i\in\Omega_d} E_{iu}(t,f)\right|^2$. Then, the covariance of $G(t,f)$ can be written as

$$\begin{aligned}
&\gamma_G(\tau,f) = \mathrm{cov}\Big(G(t,f), G(t-\tau,f)\Big) \\
&= \sum_{u\in\{x,y,z\}} \mathrm{cov}\Big(G_u(t,f), G_u(t-\tau,f)\Big) + \mathrm{cov}\Big(\varepsilon(t,f), \varepsilon(t-\tau,f)\Big) \\
&= \sum_{u\in\{x,y,z\}} \mathrm{cov}\Big(G_u(t,f), G_u(t-\tau,f)\Big) + \delta(\tau)\sigma^2(f),
\end{aligned} \tag{3.19}$$

which is due to Assumptions 2-3 and the assumptions of the noise term. Thus, in the following, we only need to focus on the term $\gamma_{G_u}(\tau,f) \triangleq \mathrm{cov}\Big(G_u(t,f), G_u(t-\tau,f)\Big)$, that is, for $\forall u \in \{x,y,z\}$, we have the equation 3.20.

$$\begin{aligned}
&\gamma_{G_u}(\tau,f) = \Big\langle G_u(t,f) - \langle G_u(t,f)\rangle, G_u(t-\tau,f) - \langle G_u(t-\tau,f)\rangle \Big\rangle \\
&= \Big\langle \underbrace{2\mathrm{Re}\Big\{E^*_{su}(f)\sum_{i\in\Omega_d} E_{iu}(t,f)\Big\}}_{\mathcal{A}_1} + \underbrace{\Big(\Big|\sum_{i\in\Omega_d} E_{iu}(t,f)\Big|^2 - \langle\Big|\sum_{i\in\Omega_d} E_{iu}(t,f)\Big|^2\rangle\Big)}_{\mathcal{A}_2}, \\
&\underbrace{2\mathrm{Re}\Big\{E^*_{su}(f)\sum_{i\in\Omega_d} E_{iu}(t-\tau,f)\Big\}}_{\mathcal{A}_3} + \underbrace{\Big(\Big|\sum_{i\in\Omega_d} E_{iu}(t-\tau,f)\Big|^2 - \langle\Big|\sum_{i\in\Omega_d} E_{iu}(t-\tau,f)\Big|^2\rangle\Big)}_{\mathcal{A}_4}\Big\rangle
\end{aligned} \tag{3.20}$$

We begin with the term $\Big\langle \mathcal{A}_1, \mathcal{A}_3 \Big\rangle$. For notational convenience, define $E_{iu}(t,f) \triangleq$

$a_i(t) + jb_i(t)$ and $E_{su}(f) \triangleq u + jv$, for $\forall i \in \Omega_d$, $\forall u \in \{x, y, z\}$, and a_i, b_i, u, v are all real. Then, we have

$$\begin{aligned}
&\left\langle \mathcal{A}_1, \mathcal{A}_3 \right\rangle \\
=\ & 4\left\langle u\sum_{i\in\Omega_d} a_i(t) + v\sum_{i\in\Omega_d} b_i(t), u\sum_{i\in\Omega_d} a_i(t-\tau) + v\sum_{i\in\Omega_d} b_i(t-\tau)\right\rangle \\
=\ & 4u^2\sum_{i\in\Omega_d}\left\langle a_i(t), a_i(t-\tau)\right\rangle + 4v^2\sum_{i\in\Omega_d}\left\langle b_i(t), b_i(t-\tau)\right\rangle \\
=\ & 4(u^2+v^2)\sum_{i\in\Omega_d}\left\langle a_i(t), a_i(t-\tau)\right\rangle, \qquad (3.21)
\end{aligned}$$

where we apply the assumption that the real and imaginary parts of the electric field have the same statistical behaviors. At the same time, we have

$$\begin{aligned}
&\mathrm{cov}(E_{iu}(t,f), E_{iu}(t-\tau,f)) \\
=\ & \left\langle E_{iu}(t,f), E_{iu}(t-\tau,f)\right\rangle \\
=\ & \left\langle a_i(t), a_i(t-\tau)\right\rangle + \left\langle b_i(t), b_i(t-\tau)\right\rangle \\
=\ & 2\left\langle a_i(t), a_i(t-\tau)\right\rangle. \qquad (3.22)
\end{aligned}$$

Thus, we have

$$\begin{aligned}
&\left\langle \mathcal{A}_1, \mathcal{A}_3 \right\rangle \\
=\ & 2|E_{su}(f)|^2\sum_{i\in\Omega_d}\mathrm{cov}\Big(E_{iu}(t,f), E_{iu}(t-\tau,f)\Big). \qquad (3.23)
\end{aligned}$$

Next, we derive the term $\left\langle \mathcal{A}_1, \mathcal{A}_4 \right\rangle$ as shown in 3.24. According to the integral representation of the electric field in 3.3, we have

$$\begin{aligned}
&|E_{iu}(t,f)|^2 \\
=\ & \iint_{4\pi} F_{iu}(\Theta_1)F^*_{iu}(\Theta_2)\exp(-j(\vec{k}(\Theta_1)-\vec{k}(\Theta_2))\cdot\vec{v}_i t)\mathrm{d}\Theta_1\mathrm{d}\Theta_2, \qquad (3.25)
\end{aligned}$$

$$\begin{aligned}
\Big\langle \mathcal{A}_1, \mathcal{A}_4 \Big\rangle &= 2\Big\langle u \sum_{i\in\Omega_d} a_i(t) + v \sum_{i\in\Omega_d} b_i(t), \Big(\sum_{i\in\Omega_d} a_i(t-\tau)\Big)^2 + \Big(\sum_{i\in\Omega_d} b_i(t-\tau)\Big)^2 - \langle \Big| \sum_{i\in\Omega_d} E_{iu}(t-\tau, f)\Big|^2 \rangle \Big\rangle \\
&= 2\Big\langle u \sum_{i\in\Omega_d} a_i(t) + v \sum_{i\in\Omega_d} b_i(t), \Big(\sum_{i\in\Omega_d} a_i(t-\tau)\Big)^2 + \Big(\sum_{i\in\Omega_d} b_i(t-\tau)\Big)^2 \Big\rangle \\
&= 2u \sum_{i\in\Omega_d} \Big\langle a_i(t), a_i^2(t-\tau) \Big\rangle + 2v \sum_{i\in\Omega_d} \Big\langle b_i(t), b_i^2(t-\tau) \Big\rangle. \qquad (3.24)
\end{aligned}$$

and thus, the covariance between $E_{iu}(t,f)$ and $|E_{iu}(t-\tau,f)|^2$ can be expressed as

$$\begin{aligned}
& \mathrm{cov}(E_{iu}(t,f), |E_{iu}(t-\tau,f)|^2) \\
&= \Big\langle E_{iu}(t,f) - \langle E_{iu}(t,f)\rangle, |E_{iu}(t-\tau,f)|^2 - \langle |E_{iu}(t-\tau,f)|^2 \rangle \Big\rangle \\
&= \Big\langle E_{iu}(t,f), |E_{iu}(t-\tau,f)|^2 \Big\rangle \\
&= \iiint_{4\pi} \Big\langle F_{iu}(\Theta_1), F_{iu}(\Theta_{21}) F_{iu}^*(\Theta_{22}) \Big\rangle \exp(-j\vec{k}(\Theta_1)\cdot\vec{v}_i t) \\
&\qquad \exp(-j(\vec{k}(\Theta_{21}) - \vec{k}(\Theta_{22}))\cdot\vec{v}_i(t-\tau))\, \mathrm{d}\Theta_1\, \mathrm{d}\Theta_{21}\, \mathrm{d}\Theta_{22} \\
&= \int_{4\pi} \Big\langle F_{iu}(\Theta_1), |F_{iu}(\Theta_1)|^2 \Big\rangle \exp(-j\vec{k}(\Theta_1)\cdot\vec{v}_i t)\, \mathrm{d}\Theta_1 \\
&= \int_{4\pi} \Big(\Big\langle \mathrm{Re}\Big\{F_{iu}(\Theta_1)\Big\}, \mathrm{Re}\Big\{F_{iu}(\Theta_1)\Big\}^2 \Big\rangle + \\
&\quad j\Big\langle \mathrm{Im}\Big\{F_{iu}(\Theta_1)\Big\}, \mathrm{Im}\Big\{F_{iu}(\Theta_1)\Big\}^2 \Big\rangle \Big) \exp(-j\vec{k}(\Theta_1)\cdot\vec{v}_i t)\mathrm{d}\Theta_1 \\
&= 0, \qquad (3.26)
\end{aligned}$$

since $\langle X^3 \rangle \equiv 0$ for any Gaussian random variable with zero mean. At the same time, we have

$$\begin{aligned}
& \Big\langle E_{iu}(t,f), |E_{iu}(t-\tau,f)|^2 \Big\rangle \\
&= \Big\langle a_i(t), a_i^2(t-\tau) \Big\rangle + j\Big\langle b_i(t), b_i^2(t-\tau) \Big\rangle, \qquad (3.27)
\end{aligned}$$

$$
\begin{aligned}
\Big\langle \mathcal{A}_2, \mathcal{A}_4 \Big\rangle &= \operatorname{cov}\Big(\Big(\sum_{i\in\Omega_d} a_i(t)\Big)^2 + \Big(\sum_{i\in\Omega_d} b_i(t)\Big)^2, \Big(\sum_{i\in\Omega_d} a_i(t-\tau)\Big)^2 + \Big(\sum_{i\in\Omega_d} b_i(t-\tau)\Big)^2\Big) \\
&= \operatorname{cov}\Big(\Big(\sum_{i\in\Omega_d} a_i(t)\Big)^2, \Big(\sum_{i\in\Omega_d} a_i(t-\tau)\Big)^2\Big) + \operatorname{cov}\Big(\Big(\sum_{i\in\Omega_d} b_i(t)\Big)^2, \Big(\sum_{i\in\Omega_d} b_i(t-\tau)\Big)^2\Big) \\
&= 2\sum_{i_1,i_2\in\Omega_d} \operatorname{cov}\Big(a_{i1}(t)a_{i2}(t), a_{i1}(t-\tau)a_{i2}(t-\tau)\Big) \\
&= 2\sum_{i\in\Omega_d} \operatorname{cov}\Big(a_i^2(t), a_i^2(t-\tau)\Big) + 2\sum_{\substack{i_1,i_2\in\Omega_d \\ i_1\neq i_2}} \operatorname{cov}\Big(a_{i1}(t)a_{i2}(t), a_{i1}(t-\tau)a_{i2}(t-\tau)\Big) \qquad (3.29)
\end{aligned}
$$

---

and thus, we have $\Big\langle a_i(t), a_i^2(t-\tau)\Big\rangle = 0$. Plugging this result in 3.24, we can obtain

$$\Big\langle \mathcal{A}_1, \mathcal{A}_4 \Big\rangle = 0. \qquad (3.28)$$

Similarly, we can also derive that $\Big\langle \mathcal{A}_2, \mathcal{A}_3 \Big\rangle = 0$. At last, we derive the term $\Big\langle \mathcal{A}_2, \mathcal{A}_4 \Big\rangle$ as shown in 3.29. Since for any two Gaussian random variables, X and Y, with zero mean, the expectations can be evaluated by using of the following relationship [72]:

$$\Big\langle X^2 Y^2 \Big\rangle = \Big\langle X^2 \Big\rangle \Big\langle Y^2 \Big\rangle + 2\Big\langle XY \Big\rangle^2, \qquad (3.30)$$

then, we have, $\forall i \in \Omega_d$,

$$
\begin{aligned}
& \operatorname{cov}\Big(a_i^2(t), a_i^2(t-\tau)\Big) \\
=\ & \Big\langle a_i^2(t) - \Big\langle a_i^2(t)\Big\rangle, a_i^2(t-\tau) - \Big\langle a_i^2(t-\tau)\Big\rangle\Big\rangle \\
=\ & \Big\langle a_i^2(t), a_i^2(t-\tau)\Big\rangle - \Big\langle a_i^2(t)\Big\rangle\Big\langle a_i^2(t-\tau)\Big\rangle \\
=\ & 2\Big\langle a_i(t), a_i(t-\tau)\Big\rangle^2 \\
=\ & \frac{1}{2}\operatorname{cov}\Big(E_{iu}(t,f), E_{iu}(t-\tau,f)\Big)^2. \qquad (3.31)
\end{aligned}
$$

For $i_1, i_2 \in \Omega_d$ and $i_1 \neq i_2$, we have

$$\begin{aligned}
& \operatorname{cov}\Big(a_{i1}(t)a_{i2}(t), a_{i1}(t-\tau)a_{i2}(t-\tau)\Big) \\
= & \left\langle a_{i1}(t)a_{i2}(t), a_{i1}(t-\tau)a_{i2}(t-\tau)\right\rangle \\
= & \left\langle a_{i1}(t)a_{i1}(t-\tau), a_{i2}(t)a_{i2}(t-\tau)\right\rangle \\
= & \left\langle a_{i1}(t), a_{i1}(t-\tau)\right\rangle\left\langle a_{i2}(t), a_{i2}(t-\tau)\right\rangle \\
= & \frac{1}{4}\operatorname{cov}\Big(E_{i_1u}(t,f), E_{i_1u}(t-\tau,f)\Big) \\
& \operatorname{cov}\Big(E_{i_2u}(t,f), E_{i_2u}(t-\tau,f)\Big). \qquad (3.32)
\end{aligned}$$

Therefore, $\left\langle \mathcal{A}_2, \mathcal{A}_4 \right\rangle$ can be derived as

$$\begin{aligned}
\left\langle \mathcal{A}_2, \mathcal{A}_4 \right\rangle = & \sum_{\substack{i_1, i_2 \in \Omega_d \\ i_1 \geq i_2}} \operatorname{cov}\Big(E_{i_1u}(t,f), E_{i_1u}(t-\tau,f)\Big) \\
& \operatorname{cov}\Big(E_{i_2u}(t,f), E_{i_2u}(t-\tau,f)\Big). \qquad (3.33)
\end{aligned}$$

Finally, we can obtain the result shown in 3.10.

Chapter 4: Robust Whole-Home Motion Detection With a Single WiFi Link

Motion detection plays a fundamental role in many applications, including security surveillance, in-home activity monitoring, smart building analysis, etc. Nowadays, motion detection systems are often employed for intruder monitoring, elder care, and event detection, etc.

Unfortunately, compared with the Internet of Things advances for physical environment sensing (e.g., temperature, humidity, pressure, etc), human motion sensing technology is far from mature. Existing approaches based on cameras, infrared, RFID, etc., not only require specialized hardware but also suffer from several drawbacks that prevent them from ubiquitous adoption. For example, the mainstream video-based methods, which dominate the current markets with a number of products like Foscam, Dropcam, and Nest Cam, are vulnerable to non-motion environmental changes in daytime (e.g., sunlight condition, air flow close to heating or cooling vents), resulting in frequent false alarms. They cover only limited Line-Of-Sight (LOS) areas. To achieve whole-home coverage, they resort to multiple devices installed at different locations. In addition, a video-based approach raises significant privacy concerns and is not feasible for ubiquitously

passive motion sensing.

The WiFi-based approach naturally circumvents the shortcomings such as directive coverage and privacy intrusiveness that are inherent in previous methods.

In this chapter, we present the model, design, and implementation of WiDetect, the first practical whole-home motion detection system that achieves almost zero false alarms using only a single WiFi link. The key breakthrough lies in our investigation from a statistical perspective towards hundreds of scattering multipath components indoors. To the best of our knowledge, we are the first to explore the statistical behaviors, rather than geometrical properties, of CSI for motion sensing. Accordingly, we build a statistical model that comprehensively leverages all existing multipath components for motion detection.

The rest of this chapter is organized as follows. Section 4.1 introduces the system model, and Section 4.2 presents the design and implementation of WiDetect. Section 4.3 shows the extensive experimental evaluations of WiDetect. Section 4.4 summarizes this chapter.

4.1 System Model

To avoid the impact of synchronization errors on the measured CSI $\tilde{H}(t, f)$, in the following, we only use the power response $G(t, f)$, defined in Section 2.1,

which takes the form

$$\begin{aligned} G(t,f) &\triangleq |\tilde{H}(t,f)|^2 \\ &= |H(t,f)|^2 + 2\mathrm{Re}\{n^*(t,f)H(t,f) \\ &\quad \exp(-j(\alpha(t)+\beta(t)f))\} + |n(t,f)|^2 \\ &\triangleq |H(t,f)|^2 + \varepsilon(t,f) \\ &= \mu(t,f) + \varepsilon(t,f), \end{aligned} \tag{4.1}$$

where $\mu(t,f)$ denotes the part contributed by the signal propagations, and $\varepsilon(t,f)$ denotes the additive measurement noise.

According to the discussions in Section 3.2, the ACF of the term $\mu(t,f)$ can be approximated as

$$\begin{aligned} \rho_\mu(\tau,f) \approx \frac{1}{E_d^2(f)} \sum_{u\in\{x,y,z\}} \Bigg(& \sum_{i\in\Omega_d} \frac{2E_{s,u}^2(f)E_i^2(f)}{3} \rho_{E_{i,u}}(\tau,f) \\ & + \sum_{\substack{i_1,i_2\in\Omega_d \\ i_1\geq i_2}} \frac{E_{i_1}^2(f)E_{i_2}^2(f)}{9} \rho_{E_{i_1,u}}(\tau,f)\rho_{E_{i_2,u}}(\tau,f) \Bigg). \end{aligned} \tag{4.2}$$

where $E_i^2(f)$ denotes the radiation power of the i-th scatterer, $E_{s,u}^2(f)$ denotes the radiation power contributed by all the static scatterers along the direction $\hat{u}$, and $E_d^2(f)$ denotes the variance of $\mu(t,f)$.

The impact of the motion of each individual dynamic scatterer on the propagation of EM waves has been quantified in 4.2 based on the ACF of the power of the received electric field, and the influence of each dynamic scatterer on $\rho_\mu(\tau,f)$ is determined by the power of the electric field contributed by that scatterer. An important observation is that when $\tau \to 0$, we have $\rho_\mu(\tau,f) \to 1$. This is because

$\rho_{E_{i,u}}(\tau, f)$, for $\forall i \in \Omega_d$ and $\forall u \in \{x, y, z\}$, is continuous at point $\tau = 0$. In addition, the variance $E_d^2(f)$ measures the power reflected by all the dynamic scatterers and it can be expressed as a function of the power reflected by each individual dynamic scatterer:

$$E_d^2(f) = \sum_{u\in\{x,y,z\}} \left(\sum_{i\in\Omega_d} \frac{2E_{s,u}^2(f)E_i^2(f)}{3} + \sum_{\substack{i_1,i_2\in\Omega_d \\ i_1\geq i_2}} \frac{E_{i_1}^2(f)E_{i_2}^2(f)}{9} \right). \tag{4.3}$$

As $\mu(t, f)$ is due to the propagations of EM waves and $\varepsilon(t, f)$ is due to the imperfect measurements of CSI, it can be assumed that $\mu(t, f)$ and $\varepsilon(t, f)$ are uncorrelated with each other, i.e., $\text{cov}(\mu(t_1, f), \varepsilon(t_2, f)) = 0$, for $\forall t_1, t_2$, Therefore, the auto-covariance function of $G(t, f)$ can be expressed as

$$\begin{aligned} \gamma_G(\tau, f) &\triangleq \text{cov}\Big(\mu(t, f) + \varepsilon(t, f), \mu(t - \tau, f) + \varepsilon(t - \tau, f)\Big) \\ &= E_d^2(f)\rho_\mu(\tau, f) + \sigma^2(f)\delta(\tau), \end{aligned} \tag{4.4}$$

where $\delta(\cdot)$ is Dirac delta function. The corresponding ACF of $G(t, f)$ can thus be expressed as

$$\rho_G(\tau, f) = \frac{E_d^2(f)}{E_d^2(f) + \sigma^2(f)}\rho_\mu(\tau, f) + \frac{\sigma^2(f)}{E_d^2 + \sigma^2(f)}\delta(\tau). \tag{4.5}$$

When there exists motion and $\tau \to 0$, with the knowledge of $\rho_\mu(\tau, f) \to 1$, we know $\rho_G(\tau, f) \to \frac{E_d^2(f)}{E_d^2(f)+\sigma^2(f)} > 0$; when there is no motion and $\tau \to 0$, we have $\rho_G(\tau, f) = 0$ since $E_d^2(f) = 0$. Therefore, $\lim_{\tau\to 0} \rho_G(\tau, f)$ is a good indicator of the presence of motion, which is only determined by $E_d^2(f)$ incurred by motion and the power of the measurement noise $\sigma^2(f)$. We will exploit this important observation in the following design of WiDetect.

4.2 Design of WiDetect

In this section, we present how to design a whole-home motion detection system using commercial WiFi based on the proposed model. Specifically, we propose novel motion statistics as a measure of the likelihood of the presence of motion and accordingly design a simple yet powerful motion detector.

4.2.1 Motion Statistics

Note that when time lag τ approaches 0 and the environment is dynamic, according to (5.8), for each subcarrier $f \in \mathcal{F}$, we have

$$\lim_{\tau \to 0} \rho_G(\tau, f) = \lim_{\tau \to 0} \frac{E_d^2(f)}{E_d^2(f) + \sigma^2(f)} \rho_\mu(\tau, f) = \frac{E_d^2(f)}{E_d^2(f) + \sigma^2(f)}. \tag{4.6}$$

If the environment is static, we have $\lim_{\tau \to 0} \rho_G(\tau, f) = 0$, since $\rho_\mu(\tau, f) = 0$ for $\forall \tau \neq 0$. Therefore, the quantity $\lim_{\tau \to 0} \rho_G(\tau, f)$ is a good indicator of the presence of the motion in the environment, which is only determined by the power of motion $E_d^2(f)$ and the power of measurement noise $\sigma^2(f)$ and is independent of the moving speed of the dynamic scatterers. However, $\lim_{\tau \to 0} \rho_G(\tau, f)$ cannot be measured directly due to the limitation of the channel sampling rate F_s. Instead, we use the quantity $\rho_G\left(\tau = \frac{1}{F_s}, f\right)$ as an approximation of $\lim_{\tau \to 0} \rho_G(\tau, f)$ as long as F_s is large enough, and the motion statistic $\phi(f)$ on subcarrier f is thus defined as

$$\phi(f) \triangleq \rho_G\left(\tau = \frac{1}{F_s}, f\right), \tag{4.7}$$

which can be estimated from the power response measurements $G(t,f)$ as

$$\hat{\phi}(f) = \frac{\hat{\gamma}_G\left(\tau = \frac{1}{F_s}, f\right)}{\hat{\gamma}_G(\tau = 0, f)}, \tag{4.8}$$

where $\hat{\gamma}_G(\tau, f)$ is the sample covariance. When there is no motion in the environment, we have $\phi(f) = 0$; when there is motion, we have $\phi(f) \in (0, \frac{E_d^2(f)}{E_d^2(f)+\sigma^2(f)})$ and $\phi(f)$ approaches to $\frac{E_d^2(f)}{E_d^2(f)+\sigma^2(f)}$ only when both the sampling rate F_s and the number of samples are sufficiently large.

Assume that the channel is sampled with equal intervals and there are T measurements in total. Without loss of generality, we can arrange the measured power responses as $G(t,f)$, for $t = 0, \frac{1}{F_s}, ..., \frac{T-1}{F_s}$ and $f = 1, ..., F$. When there is no motion in the environment, it is already shown in Section 3.2 that the power response on each subcarrier f follows a Gaussian distribution with a constant mean, i.e., $G(t,f) \sim \mathcal{N}(\mu(f), \sigma^2(f))$, where we define the constant as $\mu(f) \triangleq \mu(t,f)$, for $\forall t$. Furthermore, when T is large enough, the sample ACF of $G(t,f)$ can be approximated as a Gaussian random variable with mean $-\frac{1}{T}$ and $\frac{1}{T}$ as the variance, i.e., $\hat{\rho}_G(\tau, f) \sim \mathcal{N}(-\frac{1}{T}, \frac{1}{T})$ for $\forall \tau \neq 0$. Specifically, for the case $\tau = \frac{1}{F_s}$, the distribution of the estimation of the proposed motion statistic $\phi(f)$ is thus obtained as $\hat{\phi}(f) \sim \mathcal{N}(-\frac{1}{T}, \frac{1}{T})$. Since the noise term $\varepsilon(t,f)$ is independent for different subcarriers, the estimated motion statistics $\hat{\phi}(f)$, $\forall f \in \mathcal{F}$, are thus independent and identically distributed random variables. Note that the distribution of $\hat{\phi}(f)$ is only a function of the sample size T and is not affected by the variance of measurement noise $\sigma^2(f)$. Therefore, the variation of $\sigma^2(f)$ due to the imperfection of the circuits will not affect the statistical behaviors of $\hat{\phi}(f)$ when no motion is

present in the environment.

4.2.2 Detection Rule

Motion detection can be formulated as a hypothesis testing problem:

$$\begin{aligned}\mathcal{H}_0: &\quad \hat{\phi}(f) \sim \mathcal{N}(-\frac{1}{T}, \frac{1}{T}),\ \forall f \in \mathcal{F},\\ \mathcal{H}_1: &\quad \hat{\phi}(f) \to \frac{E_d^2(f)}{E_d^2(f)+\sigma^2(f)} > 0,\ \forall f \in \mathcal{F}\end{aligned}$$

where $\mathcal{H}_0$ denotes the null hypothesis when there is no motion in the monitored environment, and $\mathcal{H}_1$ denotes the alternative hypothesis when motion happens.

We define the average of motion statistics as $\hat{\psi} = \frac{1}{F}\sum_{f=1}^{F}\hat{\phi}(f)$. Since $\hat{\phi}(f)$'s are independent and identically distributed for different subcarriers, the distribution of the sample average of $\hat{\phi}(f)$ over F subcarriers can be approximated as $\hat{\psi} \sim \mathcal{N}(-\frac{1}{T}, \frac{1}{FT})$, that is, the variance of $\hat{\psi}$ is inversely proportional to the number of samples T and the number of subcarriers F. At the same time, since the motion statistic $\hat{\phi}(f)$ is a positive number when there is motion in the environment, a simple detection rule is proposed for the detection of the presence of motion: given a preset threshold η, if $\hat{\psi}$ is greater than or equal to η, than WiDetect reports a detection of motion; otherwise, no motion is detected.

Thus, under the hypothesis $\mathcal{H}_0$ and a given preset threshold η, the probability of false alarm can be approximated as

$$P\Big(\hat{\psi} > \eta\Big) = Q\bigg(\sqrt{FT}\Big(\eta + \frac{1}{T}\Big)\bigg), \tag{4.9}$$

where $Q(\cdot)$ denotes the Q-function, which is the tail probability of the standard normal distribution, i.e., $Q(x) = \frac{1}{2\pi}\int_x^{\infty}\exp(-\frac{u^2}{2})\,\mathrm{d}u$.

For the detection probability of WiDetect, it is hard to characterize it theoretically since $\hat{\phi}(f)$ is determined by $E_d^2(f)$, that is dependent on the location of motion, and $\sigma^2(f)$, that is dependent on the working condition of the WiFi chipsets. However, when there is no motion, the statistical behavior of $\hat{\psi}$ is only a function of F and T, which is independent of the variance of the measurement noise $\sigma^2(f)$.

4.3 Experimental Evaluation

To evaluate the performance of WiDetect, a prototype based on a pair of commercial WiFi devices is built to detect human motion in two different environments as shown in Fig. 4.1. The carrier frequency is set to 5.805GHz, and the bandwidth is set to 40MHz. Each WiFi device is equipped with 3 omnidirectional antennas, and each antenna-pair link has a total of 114 subcarriers. To avoid the correlations among adjacent subcarriers, we take one subcarrier from every two adjacent ones and only use 58 subcarriers for each link, considering the fact that the CSI of DC subcarrier is not accessible.

4.3.1 Validation of the Theoretical Analysis

We first verify the theoretical analysis described in Section 4.1, and then verify the performance of the proposed detection rule of WiDetect using the same WiFi channel. The sampling rate F_s is set to 180 Hz, and the Tx and Rx of WiDetect are placed at location Tx #2 and Rx #2, respectively, as shown in Fig. 4.1(a). One

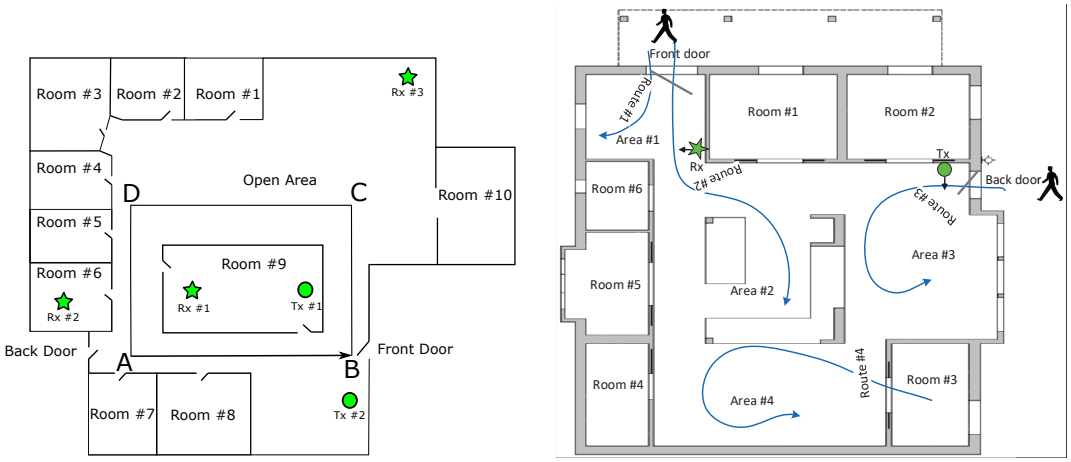

(a) A typical office.

(b) A typical single house.

Figure 4.1: Floorplans of two different environments.

subject first walks inside the conference room for 30 minutes, and then walks outside the conference room but within the square $A-B-C-D$ indicated in Fig. 4.1(a) for another 30 minutes. At last, we collect a set of one-hour CSI data when the environment is static and no one is inside the office.

We calculate the false positive rate using the experimental CSI data and compare with the theoretical false alarm probability according to (4.9), and the comparison is shown in Fig. 4.2(a) and Fig. 4.2(d) for different sample sizes T and different number of subcarriers F, respectively, for varying η. The theoretical curves match well with the experimental ones when η is greater, and the gap at smaller η is due to the correlation among different subcarriers, which we assume not existing in the theoretical analysis. As for the detection probability, Fig. 4.2(b) shows that increasing T improves the detection probability for a fixed η and Fig. 4.2(e) indicates that increasing F has no effect on the detection probability. The ROC curves in Fig. 4.2(c) and Fig. 4.2(f) show that the performance of

WiDetect improves as T and F increase.

From the analysis in Section 4.2, a higher sampling rate F_s is preferred, and the higher the sampling rate, the larger the motion statistics can be obtained when motion exists. The normalized histograms of $\hat{\psi}$ in the above-mentioned three scenarios with varying channel sampling rate F_s are also shown in Fig. 4.3. As we can observe from the figure, the average of the motion statistics $\hat{\psi}$ increases as the sampling rate increases when there exists motion, which facilitates the detection of the presence of the motion. However, In practice, a higher sampling rate would incur a larger interference to the existing WiFi network. As a result of the trade-off, we set channel sampling rate as $F_s = 30$Hz in the following experiments.

Furthermore, when motion occurs more closely to the one of the devices, $\hat{\psi}$ becomes larger as well. This is because the energy E_d^2 of the reflected EM waves off the moving human body is larger due to a smaller path loss when the human body is close to the transmission pair.

In the following experiments, the parameters $\eta = 0.1$, $T = 60$ are applied and all the available subcarriers from the 9 links are utilized in WiDetect.

4.3.2 Coverage Test

In this experiment, to test the coverage of WiDetect, one subject walks in different regions of an office and a single house as shown in Fig. 4.1, respectively, and the positions of the Tx and Rx are also indicated in the floorplan. We define the

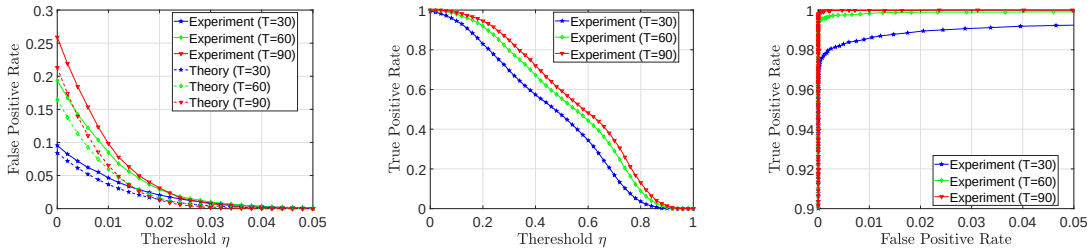

(a) False positive rate vs. η. (b) True positive rate vs. η. (c) RoC.

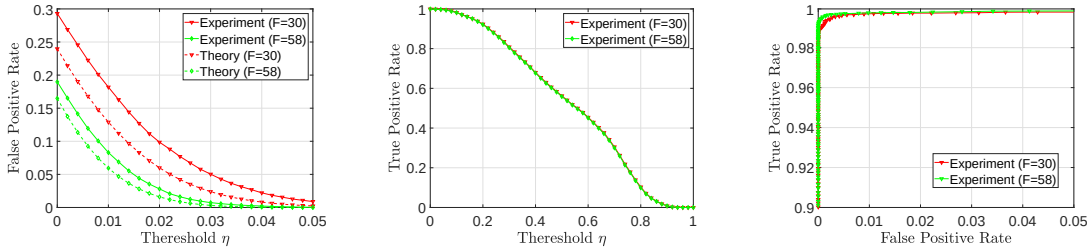

(d) False positive rate vs. η. (e) True positive rate vs. η. (f) RoC.

Figure 4.2: Performance of the proposed WiDetect for different window size T and number of subcarriers F.

empirical detection probability (EDP) of a region as the ratio between the duration when motion is detected and the total time when motion is present in that region. The corresponding results are summarized in Fig. 4.4(a) and Fig. 4.4(b), which show that the motion occurring in most of areas of the office and the house can be detected by the deployed single pair of WiFi devices except for a few rooms far away from the transmission pair. In some regions such as Room #1 and #2 in Fig. 4.4(a), motion is not detected all the time. However, as long as there is at least one motion detected along the subject's moving trajectory, the presence of that moving subject can be detected.

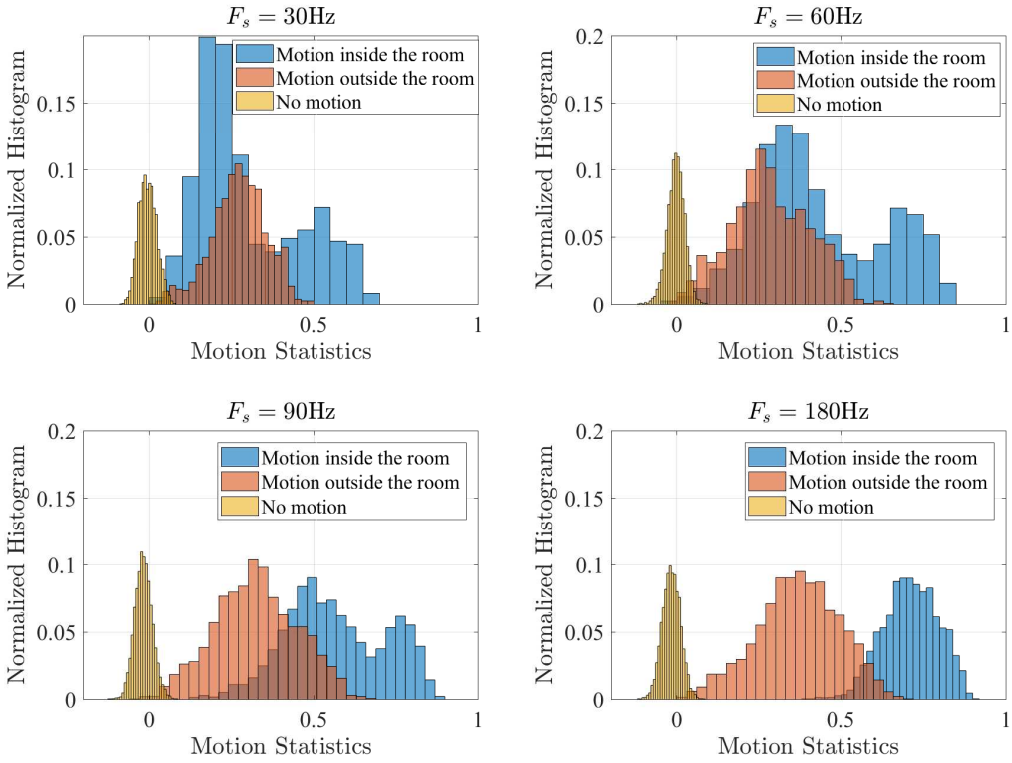

Figure 4.3: The normalized histogram of $\hat{\psi}$ under three conditions: motion inside of the room, motion outside of the room and no motion indoors with $T = 60$ and $F = 58$. The sampling rate of (a) - (d) is set to 30 Hz, 60 Hz, 90 Hz, and 180 Hz, respectively.

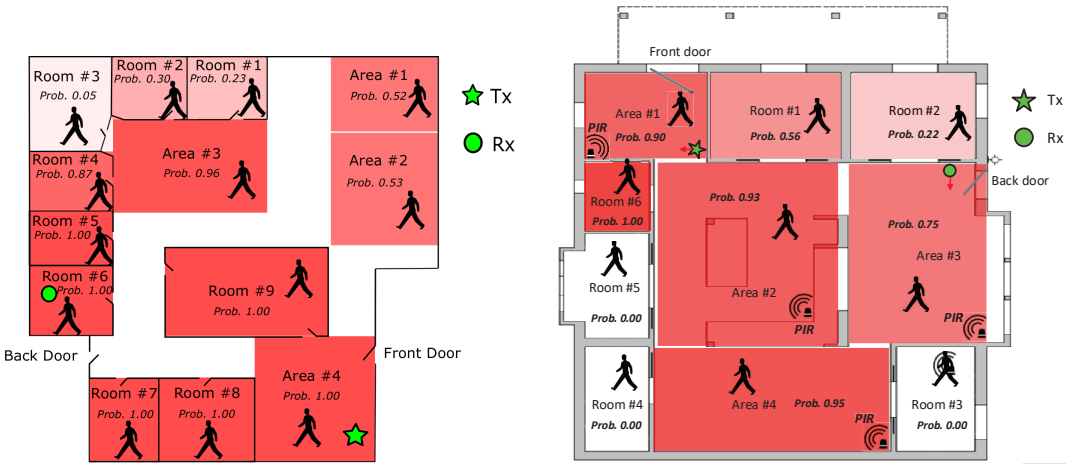

(a) The coverage of WiDetect in an office. (b) The coverage of WiDetect in a single house.

Figure 4.4: The coverage of WiDetect in two different environments.

Table 4.1: Empirical detection probability (EDP) for Different Routes

Route	#1	#2	#3	#4
EDP	0.90	0.98	0.83	1

4.3.3 Intrusion Test

In this experiment, one subject tries to "break" into the house following four different routes as indicated in Fig. 4.1(b), and then leaves the house following the same route. The subject spends about one minute in the house for each route. The empirical detection probability for the four routes are shown in Tab. 4.1. The results show that the presence of the "intruder" can be detected most of the time for all the routes.

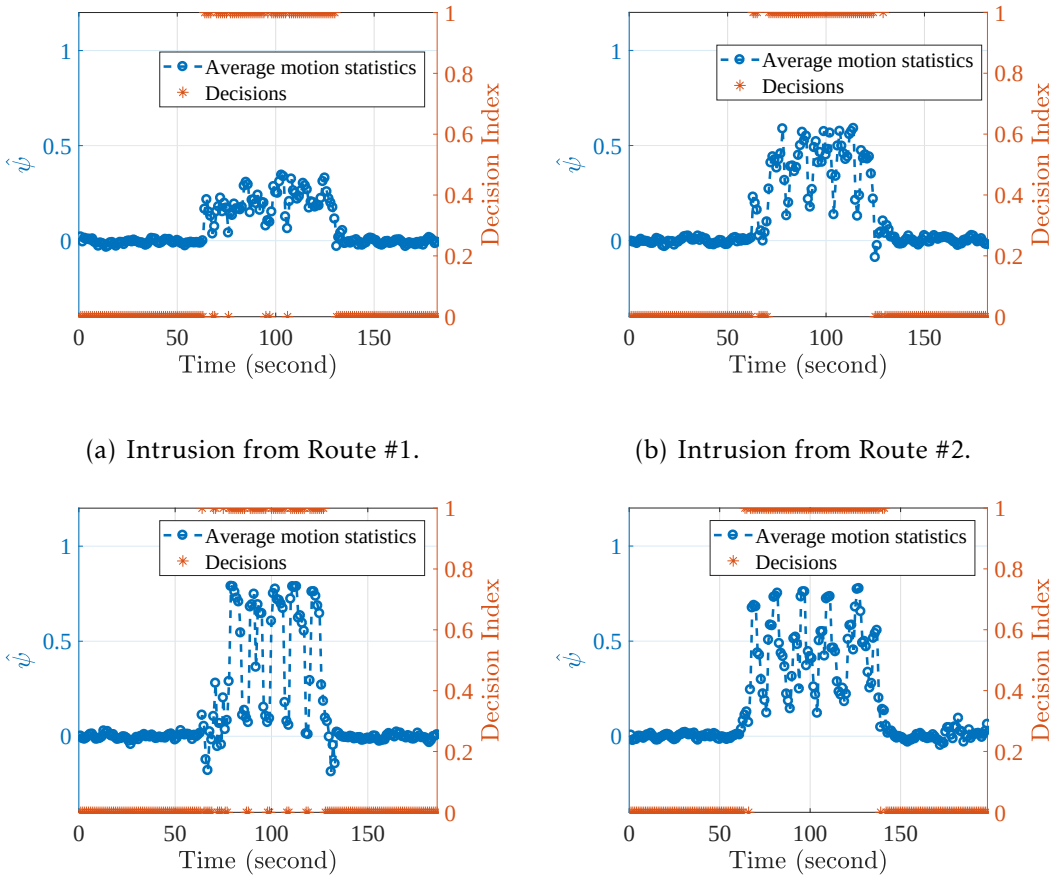

(a) Intrusion from Route #1.

(b) Intrusion from Route #2.

(c) Intrusion from Route #3.

(d) Intrusion from Route #4.

Figure 4.5: Experimental results for intrusion tests with different preset routes.

4.3.4 Long-Term Test

To evaluate the false alarm rate, we run WiDetect in the same single house for one week and compare with the detection that deploys 4 PIRs in different areas of the house. A participant is asked to enter the house every day and keeps a record of his activity as the groundtruth. The detection results for both WiDetect and the 4 PIRs are shown in Fig. 4.6, where an even decision index 0 indicates that no motion is detected and 1 indicates that motion is detected. It shows that 99.68%

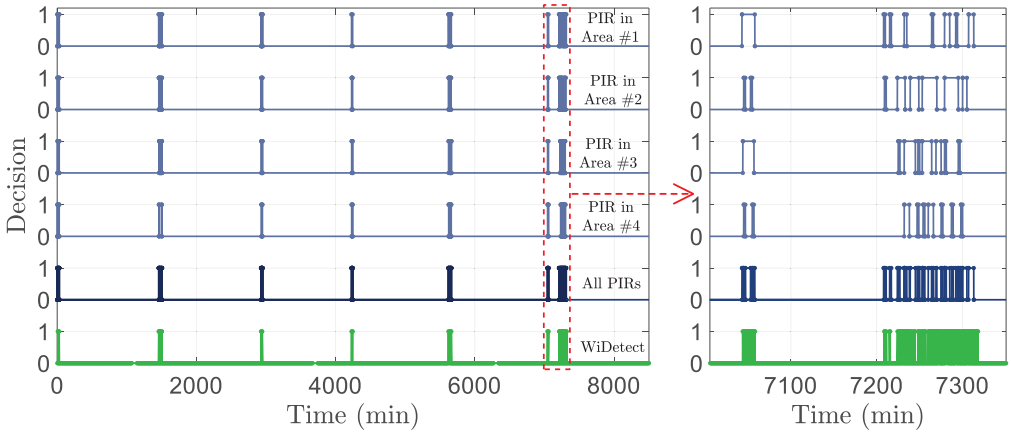

Figure 4.6: Experimental results for long-term test compared with PIRs.

percent of the recorded motion has been successfully detected by WiDetect, while only 86.80% percent of the motion is detected by the PIRs. No false alarms have been observed for both of the two systems during the whole week. The results show that WiDetect can achieve comparable detection performance as the PIRs while having a much larger coverage. In addition, WiDetect achieves a much higher time resolution in motion detections compared with the commercial PIRs.

Furthermore, WiDetect is also installed in an apartment with a couple living normally inside for one month. To show the patterns of daily activities, only the percentage of the motion detected within each hour is shown in Fig. 4.7. As we can see from the figure, It turns out that the lifestyle of the couple can be clearly revealed from the motion detection results of WiDetect.

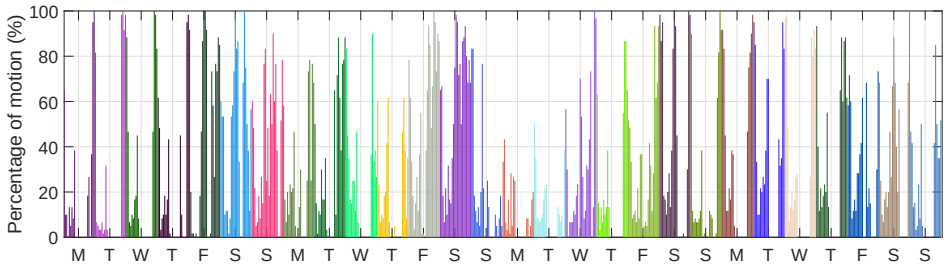

Figure 4.7: Motion monitoring for one month.

4.4 summary

In this work, we present the model, design and implementation of WiDetect, the first practical whole-home motion detection system that achieves almost zero false alarms using only a single WiFi link. A statistical model that comprehensively leverages all existing multipath components for motion detection is proposed and the relationship between the detection rate and false alarm rate for motion detection is also derived. Extensive experiments show its superiority over existing motion detection approaches. With extremely high sensitivity and fairly low false alarms, we believe that the proposed WiDetect can be a promising practical technology for ubiquitous device-free motion detection, allowing for a range of critical applications for smart life.

Chapter 5: Sleep Staging via Respiratory Rate Monitoring

Sleep plays a vital role in an individual's health and well-being, both mentally and physically. It is well recognized that sleep quantity and quality is fundamentally related to health risks like cardiovascular disease, stroke, kidney failure, diabetes, and adverse mental conditions, etc. Unfortunately, in a modern society, quite a lot of people suffer from sleep disorders. As recently reported, 10% of the population suffers from chronic insomnia (which is even higher among elders) [71], and 1/3 of Americans do not get sufficient sleep [22]. Sleep monitoring emerges as an effective mechanism to manage the morbidity and mortality associated with sleep related disorders, in addition to providing insight on people's general wellbeing.

Over the past few decades, various sleep monitoring solutions have been proposed. Typically they measure sleep time, recognize different sleep stages, e.g., wake, REM (Rapid Eye Movement) and NREM (Non-REM), and assess an individual's sleep quality. The medical gold standard is Polysomnography (PSG), which monitors various physiological parameters such as brain activity, respiration, and body movement by a number of wired sensors attached to the patient. Albeit accurate and comprehensive, PSG is usually expensive and cumbersome.

Invasive sensors may cause sleep difficulties, limiting PSG to clinical usage for confirmed patients. Other approaches including photoplethysmography (PPG) and actigraphy (ACT) require users to wear dedicated sensors during sleep. Ballistocardiogram (BCG) needs to instrument the mattress with an array of EMFi sensors to measure ballistic force. These approaches provide suitable solutions for those who need special cares but are less-than-ideal for the public due to their cost and complexity. Recent efforts in mobile computing tackle in-home sleep monitoring using smartphones and wearables. These methods, however, only provide coarse-grained, less accurate measurements and fail to monitor vital signs like respiratory rate. In addition, mobiles and wearables are undesirable for elders and those with dementia.

Different from prevailing solutions, in this chapter, we envision a future smart home that monitors daily sleep in a ubiquitous, non-invasive, contactless, and accurate manner, without instrumenting the body or the bed. While early works have investigated the feasibility of RF-based breathing estimation and sleep monitoring, they either rely on specialized hardware like FMCW radar [10,43,142], or only work in controlled environments [60,61,112,116]. Solutions based on dedicated radios are usually expensive and not ubiquitously applicable. Solutions using commodity devices typically require the user to lie still on a bed with radios exceedingly close to his/her chest. These solutions also fail in presence of extraneous motions or in Non-Line-Of-Sight (NLOS) scenarios. In addition, none of them can identify different sleep stages due to their limited accuracy in breathing estimation. Such limitations prevent them from becoming

practical in-home sleep monitoring application.

In this chapter, we first present the system model of SMARS in Section 5.1, and then, present the proposed instantaneous breathing rate estimator and the design of SMARS in Section 5.2 and Section 5.3, respectively. Lastly, extensive experimental evaluations will also be presented in Section 5.4. Section 5.5 summarizes this chapter.

5.1 System Model

In the following, we will review the model of CSI, especially under the setting of vital sign monitoring.

5.1.1 Modeling CSI

Given a wireless transmission pair each equipped with omnidirectional antennas, the CSI for the fading multipath channel at time t is expressed as

$$H(t, f) = \sum_{l \in \Omega} a_l(t) \exp(-j2\pi f \tau_l(t)), \tag{5.1}$$

where $a_l(t)$ and $\tau_l(t)$ denote the complex amplitude and propagation delay of the l-th multipath component (MPC), respectively, and Ω denotes the set of MPCs. The propagation delay is a function of the propagation distance: $\tau_l(t) = \frac{d_l(t)}{c}$, where c is the speed of light and $d_l(t)$ is the traveled distance of the l-th MPC. f denotes the particular frequency where the channel is measured. For example, in an OFDM-based communication system, such as WiFi, LTE, 5G, etc., the CSI is measured at each subcarrier with frequency f.

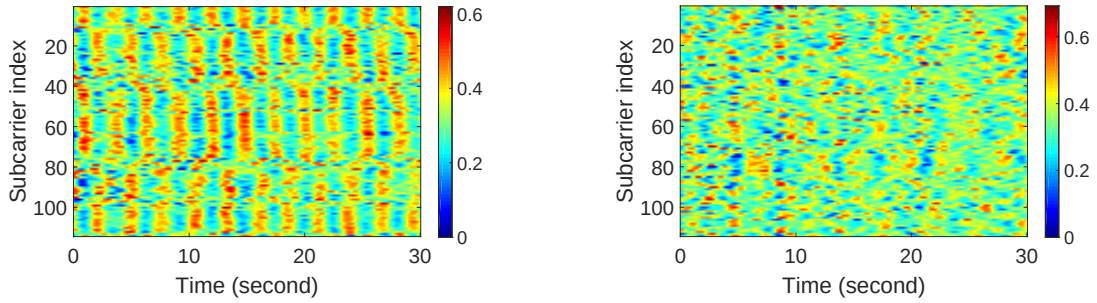

(a) LOS

(b) NLOS

Figure 5.1: The normalized CSI power response matrix with the presence of breathing signals. To facilitate the visualization, $G(t, f)$ is smoothed and normalized to the same amplitude over time for each subcarrier.

CSI depicts how radio signals propagate from a transmitter (Tx) to a receiver (Rx), e.g., reflected or scattered off all reflectors in the space such as the walls, furniture, human bodies, etc., and is highly sensitive to environmental perturbations. Any body motions, including minute chest and abdomen movements, will alter the paths of signal propagation and thus modulate the wireless signal before it arrives at the receiver, allowing SMARS to capture these motions and monitor human's sleep from the measured CSI time series.

5.1.2 Modeling Motion in CSI

Existing works usually adopt simplified models that make unrealistic assumptions of indoor multipath propagation. Most of them assume one dominate mirror reflection path from human body under 2-ray models [108, 140] that are developed for and only hold in outdoor environments [93], and accordingly at-

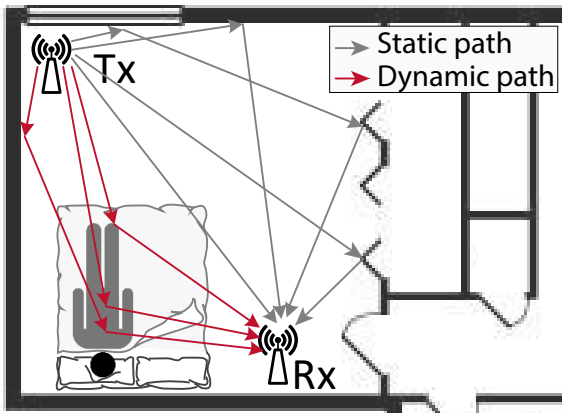

Figure 5.2: Multipath propagation

tempt to geometrically interpret multipath constructive and destructive interferences. In reality, however, signals bouncing off human body may reflect, scatter, and diffract before finally superimposed at the receiver, producing up to hundreds of multipaths indoors [32], as illustrated in Fig. 5.2. As a result, existing works can only work in clear LOS scenarios with strong breathing in proximity, where a dominant reflection path exists. A more realistic model is demanded for practical motion and breathing sensing.

Consider the case when there is a static person breathing indoors with a cycle of T_b seconds. As shown in Fig. 5.2, the MPCs can be classified into two sets: $\Omega_s(t)$ and $\Omega_d(t)$, where $\Omega_s(t)$ denotes the set of time-invariant MPCs, e.g., reflected off the floor and walls, and $\Omega_d(t)$ denotes the set of time-varying MPCs, e.g., reflected off the human body. Due to the periodic chest or abdomen movement during normal breathing, the propagation distance $d_l(t)$ of each MPC $\forall l \in \Omega_d(t)$ changes periodically with the same cycle as the breathing movement, i.e., $d_l(t + T_b) = d_l(t)$. Since the amplitude of breathing movement is small, the

change in the propagation distance for each dynamic path is also small. Therefore, it is reasonable to assume that both the sets $\Omega_s(t)$, $\Omega_d(t)$ and the complex amplitude of each MPC $a_l(t)$ are time-invariant within a sufficiently short period. Thus the CSI can be written as

$$\begin{aligned} H(t,f) &= \sum_{l_s \in \Omega_s} a_{l_s} \exp(-j2\pi f \frac{d_{l_s}}{c}) \\ &\quad + \sum_{l_d \in \Omega_d} a_{l_d} \exp(-j2\pi f \frac{d_{l_d}(t)}{c}) \\ &\triangleq H_s(f) + H_d(t,f), \end{aligned} \tag{5.2}$$

where $H_s(f)$ and $H_d(t,f)$ denote the contribution of the time-invariant MPCs and time-varying MPCs, respectively.

In real measurements, $H(t,f)$ is corrupted by the phase noise, caused by the timing and frequency synchronization offsets, and the additive thermal noise $n(t,f)$, and the reported CSI $\tilde{H}(t,f)$ can be expressed as

$$\tilde{H}(t,f) = \exp(-j(\alpha(t) + \beta(t)f))H(t,f) + n(t,f), \tag{5.3}$$

where $\alpha(t)$ and $\beta(t)$ are the random initial and linear phase distortions at time t, respectively. Define the *channel power response* $G(t,f)$ as the square of the magnitude of $\tilde{H}(t,f)$:

$$\begin{aligned} G(t,f) &\triangleq |\tilde{H}(t,f)|^2 \\ &= |H(t,f)|^2 + 2\mathrm{Re}\{n^*(t,f)H(t,f) \\ &\quad \exp(-j(\alpha(t) + \beta(t)f))\} + |n(t,f)|^2 \\ &\triangleq |H(t,f)|^2 + \varepsilon(t,f) \end{aligned} \tag{5.4}$$

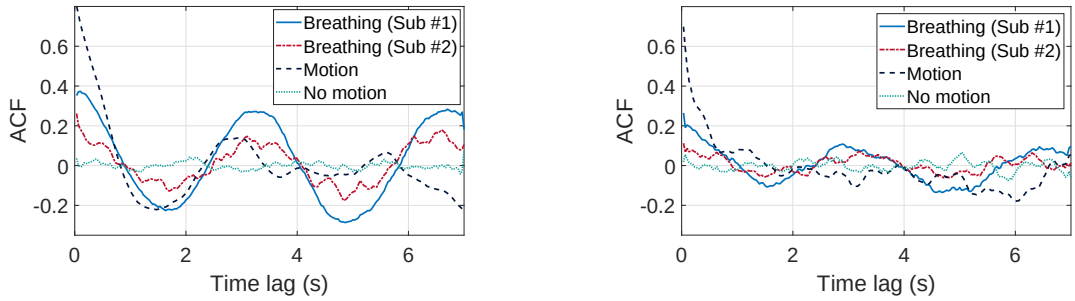

(a) LOS

(b) NLOS

Figure 5.3: The illustrations of ACFs under LOS and NLOS scenarios.

where the superscript * denotes the operator of complex conjugate, the operator Re{x} denotes the real part of x, and $\varepsilon(t,f)$ is defined as the noise term, which can be approximated as additive white Gaussian noise (AWGN) with variance $\sigma^2(f)$ and is statistically independent of $H(t,f)$ [138]. From (5.2) and the fact that $d_l(t+T_b) = d_l(t)$, $\forall l \in \Omega_d$, we have $|H(t+T_b,f)|^2 = |H(t,f)|^2$. Thus, $G(t,f)$ is modeled as a noisy periodic signal with a period of T_b.

As shown in Fig. 5.1, we measure the CSI power response $G(t,f)$ using a pair of commercial WiFi devices for both the two cases, when a subject is breathing in a LOS and a NLOS location with respect to the transmission pair, respectively. For the LOS case, the strength of the measured breathing signal is strong and the periodic pattern can be easily observed by most subcarriers as shown in Fig. 5.1(a). For the NLOS case as shown in Fig. 5.1(b), however, there are no apparent periodic patterns that can be observed since the breathing signal is much weaker.

Note that $G(t,f)$ is a result of numerous multipath components [32] adding up together in a complex way expressed in (5.2). As shown in Fig. 5.1(a), both the

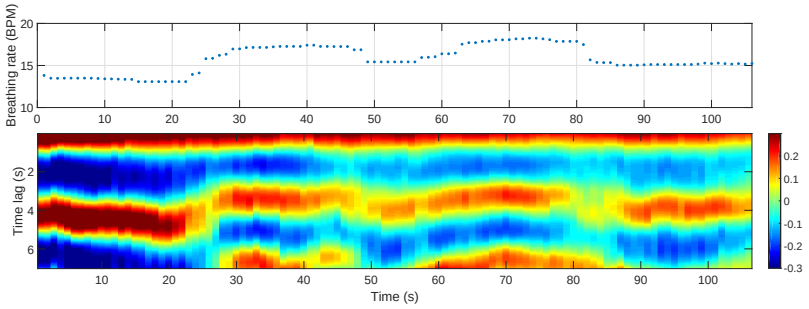

Figure 5.4: Breathing rate estimation from ACFs.

amplitudes and the phases of the breathing signal measured by CSI are different for different subcarriers. Accordingly, it is reasonable to express $|H(t,f)|^2$ in the following form:

$$|H(t,f)|^2 = g(f)b(t-\Delta t_f), \tag{5.5}$$

where $b(t)$ denotes a periodic stationary breathing signal with zero mean, which is related to the movement of the chest and abdomen, and $g(f)$ and Δt_f stand for the gain and the random initial phase of the breathing signal measured at the frequency f, respectively.

Combining (5.4) and (5.5), the received signal at subcarrier with frequency f is expressed as

$$G(t,f) = g(f)b(t-\Delta t_f) + \varepsilon(t,f). \tag{5.6}$$

Breathing estimation is then conducted based on the power response $G(t,f)$, which circumvents the use of noisy CSI phase and the usually handcrafted phase cleaning step.

5.2 Instantaneous Breathing Rate Estimation

5.2.1 Estimating Breathing Rate

Observing that breathing signal is periodic, previous methods usually perform frequency analysis on the CSI data collected in a time window to estimate breathing rate [60, 61, 116]. These methods require a large delay (e.g., more than 30 seconds) to gain better frequency resolution, and cannot observe immediate breathing rate changes, since breathing rate is assumed to be constant during the time window. Differently in SMARS, we adopt a statistical approach by examining the autocorrelation function (ACF) of CSI power response $G(t, f)$, which significantly shortens the time delay and produces instantaneous estimation.

ACF Calculation. The ACF for a stationary signal $x(t)$ is defined as follows:

$$\rho(\tau) = \frac{\text{cov}[x(t), x(t+\tau)]}{\text{cov}[x(t), x(t)]}, \tag{5.7}$$

where τ denotes the time lag, and $\text{cov}[\cdot]$ denotes the covariance operator. Thus, the ACF of $G(t, f)$ is computed as

$$\rho_G(\tau, f) = \frac{g^2(f)}{g^2(f) + \sigma^2(f)} \rho_b(\tau) + \frac{\sigma^2(f)}{g^2(f) + \sigma^2(f)} \delta(\tau), \tag{5.8}$$

where $\rho_b(\tau)$ is the ACF of $b(t)$, and $\delta(\tau)$ denotes the Dirichlet function. Define $k(f) \triangleq \frac{g^2(f)}{g^2(f)+\sigma^2(f)}$ as the normalized channel gain, and for $\tau \neq 0$, we have

$$\rho_G(\tau, f) = k(f) \rho_b(\tau). \tag{5.9}$$

In practice, the sample ACF is used instead [95], which is an estimate of the

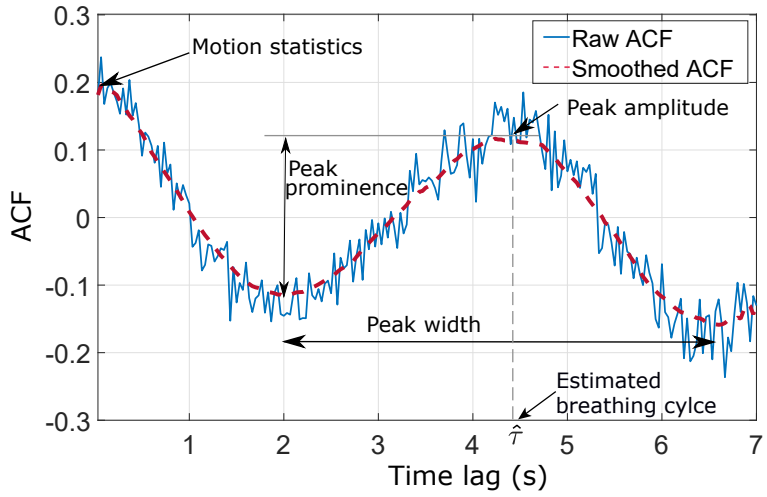

Figure 5.5: Features extracted from the derived ACF for breathing detection and estimation.

ACF, and we use $n(\tau, f)$ to stand for the estimation noise of the ACF, i.e.,

$$\hat{\rho}_G(\tau, f) = k(f)\rho_b(\tau) + n(\tau, f). \tag{5.10}$$

As shown in Fig. 5.3, when there is a breathing signal, the ACF will exhibit a definite peak at a certain delay (although the peak value may differ over different subcarriers), contributed by the periodic breathing motions. On the contrary, no prominent peaks can be observed on any subcarrier when there is no breathing (i.e., no periodic motions). In principle, as shown in Fig. 5.4, a time delay slightly longer than one breathing cycle (e.g., 5 to 7 seconds) is sufficient to pick up the first breathing rate and later on instantaneous estimates can be produced every one second.

Motion Statistic. Prior to breathing estimation, a key step is to examine whether there exists any extra large motions. As mentioned previously, breath-

ing will easily be buried in other large body motions, and should not be estimated in such case. As shown in Fig. 5.3(a) and (b), the first time lag of the ACF of a subcarrier, named as the *motion statistic* in the following, indicates the strength of total motions, including periodic and non-periodic motions, existing in the monitored area. A very large motion statistic indicates the presence of large motions, such as walking and standing up, and a very small motion statistic that is close to 0 indicates that there is no significant motion in the environment. When there is only breathing motion in the monitored area, the motion statistic of each subcarrier shows the sensitivity of that subcarrier to the breathing motion.

Breathing Detection and Estimation. Based on the calculated ACF, SMARS first detects the presence/absence of breathing and, if present, it then estimates the breathing rate. As shown in Fig. 5.5, for a subcarrier with frequency f, we extract the following five features from $\hat{\rho}_G(\tau, f)$ for breathing detection, in addition to the *motion statistic*:

1. *Peak prominence*: the vertical distance between a peak value and the largest height of the adjacent valleys, which measures the likelihood of the existence of the peak;
2. *Peak width*: the horizontal distance between the two adjacent valleys, which also measures the likelihood of the existence of a peak;
3. *Peak amplitude*: the height of a peak, which measures the amplitude of the ACF of the breathing signal and will be comparable to the value of motion statistic in presence of only breathing motion;

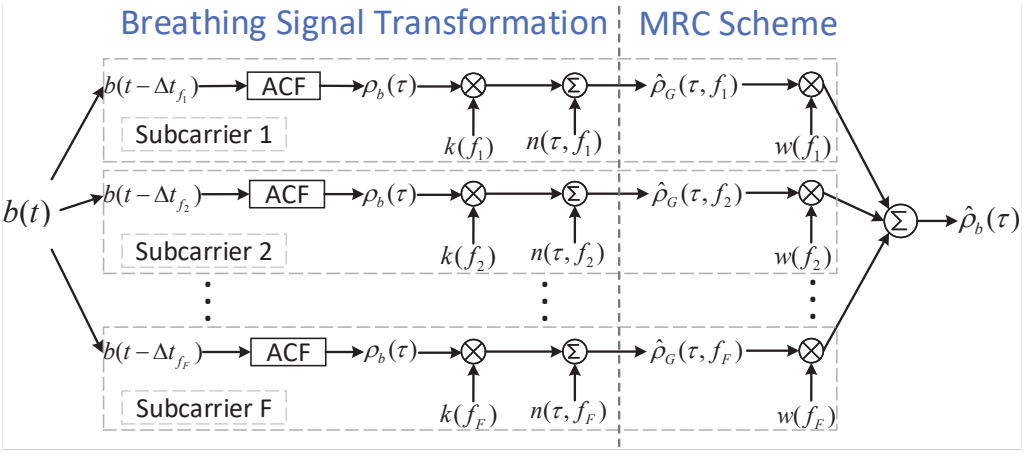

Figure 5.6: The diagram of MRC on ACF of breathing signal.

4. *Motion interference ratio*: the ratio between the motion statistic and peak amplitude, which measures the degree of the interference of the non-breathing motion, such as body movements, walking, standing up, typing keyboard, etc., in the environment;
5. *Peak location*: the horizontal distance between the origin and the peak (i.e., time lags), which measures the breathing cycle.

In general, the larger the motion statistic, peak prominence, peak width, peak amplitude and the smaller the motion interference ratio, the more likely is the presence of the breathing signal. In SMARS, the above six features are jointly fused to determine the existence of a breathing signal and the corresponding breathing rate. Once there is a breathing signal, the breathing rate can be estimated as BR = $60/\hat{\tau}$ bpm, where $\hat{\tau}$ is the location (i.e., time lags) of the first dominant peak of $\hat{\rho}_G(\tau, f)$.

5.2.2 Maximizing Breathing Signal

In practice, the SNR of the breathing signal on each subcarrier modulated by minute breathing motions is very low, especially when the person being monitored is far away from the link, covered by quilts, or behind the wall. As shown in Fig. 5.3, the SNR of the ACF for NLOS breathing is significantly lower than that for LOS scenarios. Previous approaches attempt to select a set of best subcarriers among others, or take an ensemble average over all subcarriers to improve the quality of the breathing signal strength [60, 61, 112, 116]. However, we make the following observations that demonstrate the flaws of these methods: 1) Any single subcarrier does not produce the optimal estimation, no matter what criteria is used for selection. 2) CSI amplitude or its variance is not an effective metric for subcarrier selection. The subcarrier with largest amplitude or variance usually does not capture the breathing signal to the best. 3) Due to frequency offsets across different subcarriers, CSI amplitudes responding to the person's breathing are unsynchronized and contain uncertain offsets (Fig. 5.1). Hence the CSI on different subcarriers cannot be directly averaged, which does not necessarily amplify, yet may instead rule out breathing signals. As a consequence, previous approaches do not produce reliable, not to mention optimal estimation.

To boost the breathing SNR, SMARS devises a novel scheme to combine the breathing signals measured on multiple subcarriers in an *optimal* manner. Our design is based on Maximal Ratio Combining (MRC), a classical diversity combining method in telecommunications that optimizes SNR by combining received

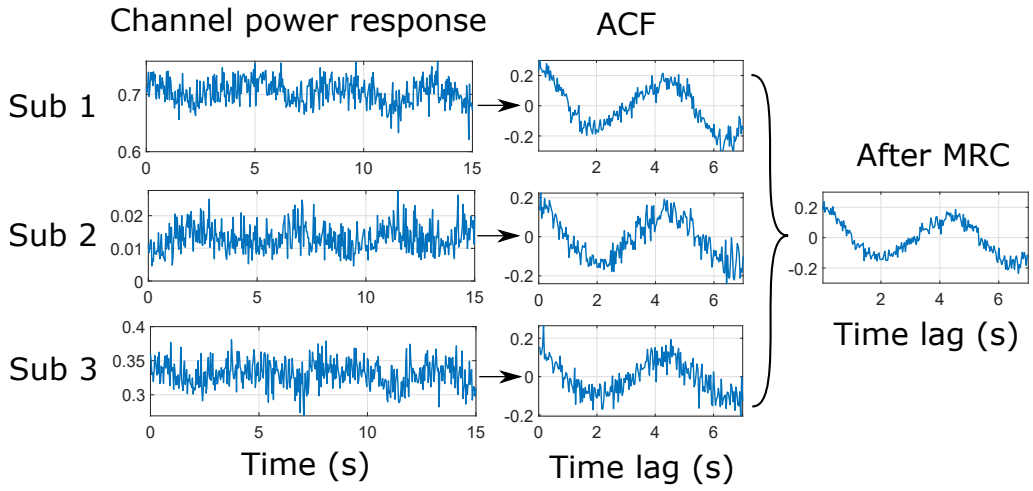

Figure 5.7: Example of MRC scheme for breathing signal maximization. Subcarrier 1, 2 and 3 rank the first, sixth and tenth respectively among the 114 subcarriers from a link according to $\hat{k}(f)$.

signals on multiple antennas [16].

MRC Model. We first review the basic concept of MRC in telecommunications in the following. Let vector $\mathbf{x} = [x_1, \ldots, x_N]^T$ denote the received signal at N antennas, which can be written as $\mathbf{x} = \mathbf{h}u + \mathbf{n}$, where $\mathbf{h} = [h_1, \ldots, h_N]^T$ denotes the constant channel gains, u denotes the transmitted random signal with unit power, and $\mathbf{n} = [n_1, \ldots, n_N]^T$ stands for the identically and independently distributed (I.I.D.) additive white Gaussian noise (AWGN) with variance σ^2. Let r denote the linearly combined signal:

$$r = \mathbf{w}^T\mathbf{x} = \mathbf{w}^T\mathbf{h}u + \mathbf{w}^T\mathbf{n}, \tag{5.11}$$

where $\mathbf{w} = [w_1, \ldots, w_N]^T$ denotes the normalized weight of each received signal at each antenna, that is, $\|\mathbf{w}\| = 1$. The SNR, denoted as γ, of the output signal r can

be denoted as

$$\gamma = \frac{\mathbb{E}[|\mathbf{w}^T\mathbf{h}u|^2]}{\mathbb{E}[|\mathbf{w}^T\mathbf{n}|^2]} = \frac{|\mathbf{w}^T\mathbf{h}|^2}{\sigma^2}. \tag{5.12}$$

By the Cauchy-Schwarz inequality, we have $|\mathbf{w}^T\mathbf{h}|^2 \leq \|\mathbf{w}\|\|\mathbf{h}\|$. The equality is achieved when $\mathbf{w}$ is linearly proportional to $\mathbf{h}$, i.e., $\mathbf{w}^* = \mathbf{h}/\|\mathbf{h}\|$, and the maximum of output SNR can be obtained as the sum of the SNR of received signals at each antenna, i.e., $\gamma = \gamma_1 + \cdots + \gamma_N$, where $\gamma_i = |h_i|^2/\sigma^2$.

MRC on Breathing Signal. In the context of breathing estimation with CSI, the breathing signal $b(t)$ is measured by multiple subcarriers. The SNR of the breathing signal, denoted as $\gamma(f)$, measured on subcarrier with frequency f at time t is defined as

$$\begin{aligned} \gamma(f) &= \frac{\mathbb{E}[(g(f)b(t-\Delta t_f))^2]}{\mathbb{E}[\varepsilon^2(t,f)]} \\ &= \frac{g^2(f)\mathbb{E}(b^2(t-\Delta t_f))}{\sigma^2(f)}, \end{aligned} \tag{5.13}$$

where $\mathbb{E}[\cdot]$ stands for the expectation operator. For convenience, the average power of the breathing signal $b(t)$ is normalized to unit power by definition, that is, $\mathbb{E}[b^2(t)] = 1$. Thus we have $\gamma(f) = g^2(f)/\sigma^2(f)$.

When applying MRC to exploit subcarrier diversity to maximize the overall SNR of the measured breathing signal optimally, however, we face three fundamental challenges:

1. The variance of the noise term in (5.6) is $\sigma^2(f)$, which is unknown and dependent on the frequency f, while MRC assumes the same variance of the noise for all the receiving elements;

2. The offset of the breathing signal Δt_f in (5.6) is incoherent for different subcarriers, while MRC requires that the transmitted signal is the same for all receiving elements;
3. The channel gain $g(f)$ in (5.6) is unknown, while MRC relies on the channel gain to compute the optimal combining weights for the receiving elements.

Fortunately, by using ACF instead of $G(t, f)$, SMARS successfully transforms the breathing signal into an appropriate form to apply MRC for optimal subcarrier combining.

Recall Section 5.2.1, when the breathing signal is extremely weak, i.e., $k(f)$ is close to zero, $G(t, f)$ is dominated by the white noise and thus, each tap of its ACF follows a zero-mean normal distribution with equal variance $1/N$ [95], i.e., $n(\tau, f) \sim \mathcal{N}(0, 1/N)$, where N is the number of samples used in the ACF estimation. Thus the variance of $n(\tau, f)$ is identical for different subcarriers, solving the first challenge.

As shown in Fig. 5.7, the ACF $\rho_b(\tau)$ are inherently synchronized over all subcarriers and is independent of the time origin. In other words, different subcarriers experience the same signal $\rho_b(\tau)$, which addresses the second challenge.

Regarding the third challenge, the channel gain $k(f)$ can be estimated as follows. For the case of single subject breathing, recall (5.9), when $\tau \to 0$, we have

$$\lim_{\tau \to 0} \rho_G(\tau, f) = k(f) \lim_{\tau \to 0} \rho_b(\tau). \tag{5.14}$$

Since the movement of chest and abdomen is continuous, the breathing signal

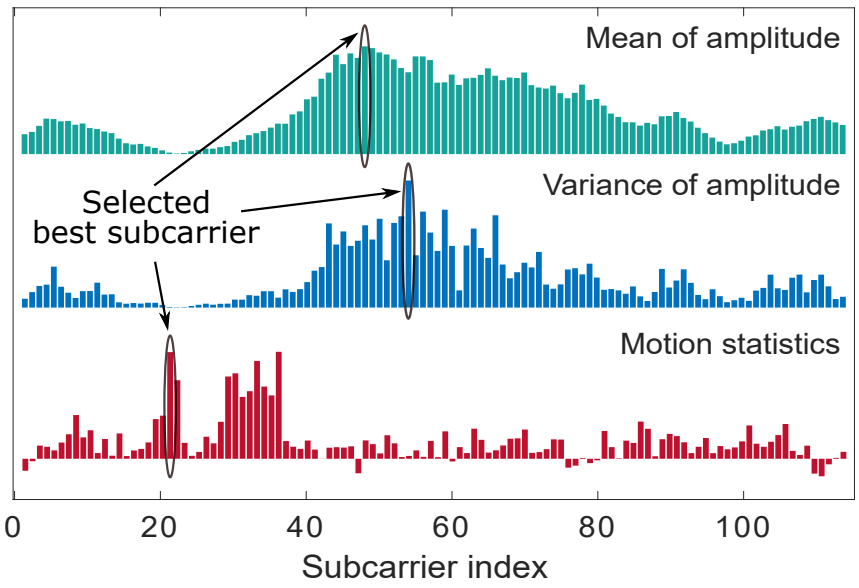

Figure 5.8: Comparison of the subcarrier selection schemes. The best subcarriers selected by the mean and variance are merely ranked 113-th and 95-th, respectively, when considering their motion statistics.

$b(t)$ is also continuous in time and we have $\lim_{\tau\to 0}\rho_b(\tau) = 1$, which leads to $\lim_{\tau\to 0}\rho_G(\tau, f) = k(f)$. As a result, when the channel sampling rate F_s is high enough, the quantity $\hat{\rho}_G(\tau = 1/F_s, f)$ is close to the channel gain $k(f)$. That is, $k(f)$ can be estimated as

$$\hat{k}(f) = \hat{\rho}_G(\tau = 1/F_s, f), \tag{5.15}$$

which is the same as the *motion statistic*. This is a key feature that underpins the use of MRC; otherwise one can still combine different subcarriers, but not optimally. To conclude, MRC can now be applied to the ACF of the breathing signal to maximize the SNR.

Maximizing Breathing SNR. We now maximize the SNR of the ACF of the breathing signal, instead of the SNR of the breathing signal, as in (5.5), which

cannot be directly maximized since the channel gain and noise cannot be measured in CSI.

Recall (5.10) and that the variance of the noise term is approximated as $1/N$, and thus, the SNR of the ACF of each subcarrier can be estimated as $N\hat{k}^2(f)$. Since the SNR of the breathing signal after MRC is the additive of the SNR measured by each subcarrier, the SNR of the combined ACF is expressed as

$$\gamma = N \sum_{f \in \mathcal{F}} \hat{k}^2(f). \tag{5.16}$$

Given a fixed number of subcarriers and sample number of N, it will be maximized by setting the optimal weight $w^\star(f)$ to $\hat{\rho}_G(\tau = 1/F_s, f)$ in the following linear combination: $\forall \tau$,

$$\begin{aligned} \hat{\rho}_b(\tau) &= \sum_{f \in \mathcal{F}} w^\star(f) \hat{\rho}_G(\tau, f) \\ &= \sum_{f \in \mathcal{F}} \hat{\rho}_G(\tau = 1/F_s, f) \hat{\rho}_G(\tau, f). \end{aligned} \tag{5.17}$$

Here $\hat{\rho}_b(\tau)$ is the ACF of the combined signal.

Fig. 5.6 summarizes the proposed scheme for breathing signal extraction and maximization. The left part of the figure shows the decomposition of the measured ACF of the channel power response when a person breathes normally in the monitored area, and the right part shows the MRC scheme for boosting the SNR of the ACF of the breathing signal. Fig. 5.7 depicts an illustrative example based on real-world measurements, where the SNR of the breathing signal is amplified by 2.5 dB compared to that obtained by the subcarrier with the largest variance and by 3.7 dB compared to that obtained by directly averaging

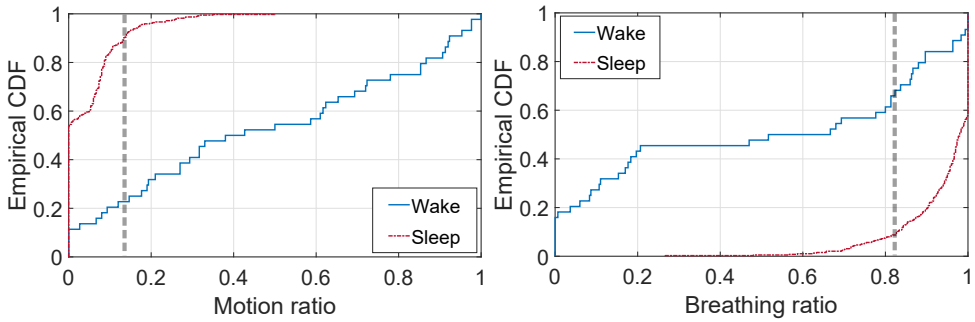

Figure 5.9: Empirical CDFs for the motion ratio and breathing ratio under two statuses: wake and sleep.

all subcarriers. Fig. 5.8 further demonstrates the gains of our ACF-based MRC scheme and confirms our observations in Section 5.2.2 that amplitudes and their variances are not effective metrics for subcarrier selection. As seen, the subcarrier that is the most sensitive to motion (i.e., holding the largest motion statistic) could experience very small amplitude and low variance.

Given the combined breathing signal with maximized SNR, SMARS then performs breathing detection and estimation, as described in Section 5.2.1, based on $\hat{\rho}_b(\tau)$, the combined ACF, instead of $\hat{\rho}_G(\tau, f)$ on a specific subcarrier, as illustrated in Fig. 5.4.

5.3 Sleep Monitoring

5.3.1 Sleep Stage Recognition

SMARS divides the continuous motion and breathing estimates of overnight sleep into 300-second epochs. For each epoch, SMARS recognizes three different

sleep stages, i.e., wake, REM sleep and NREM sleep. The staging is performed in two steps: first, SMARS differentiates wake from sleep mainly by body motions; second, REM and NREM stages are further identified during sleep period.

Sleep/Wake Detection. The key insight to identify the sleep and wake states is that, more frequent body movements will be observed when a subject is awake, while mainly breathing motion presents when he/she is asleep. SMARS utilizes the motion statistic defined in Section 5.2.1 to distinguish between the two states, since bodily movements are significantly stronger than breathing motions, and both of them can be easily captured and quantified by it.

Specifically, we define *motion ratio* as the percentage of time when the motion statistic, $\hat{\rho}_b(1/F_s)$, is larger than a preset threshold. Thus for the wake state, a higher motion ratio is expected, as shown in Fig. 5.9(a). Similarly, we also define *breathing ratio* as the percentage of time when the breathing signal is detected. Since bodily movements destroy the periodicity of the environmental dynamics, the breathing ratio will be lower when a subject is awake, as shown in Fig. 5.9(b).

Combining the above two features, SMARS labels an epoch as sleep only when the motion ratio is smaller than the predefined threshold and the breathing ratio is larger than another threshold. Both thresholds are empirically determined as in Fig. 5.9. Since our model statistically considers all multipaths indoors, the values of both thresholds generalize to different environments and subjects.

REM/NREM Recognition. SMARS exploits the following clinical facts [13] and accordingly extracts two distinctive features from breathing rate estimates

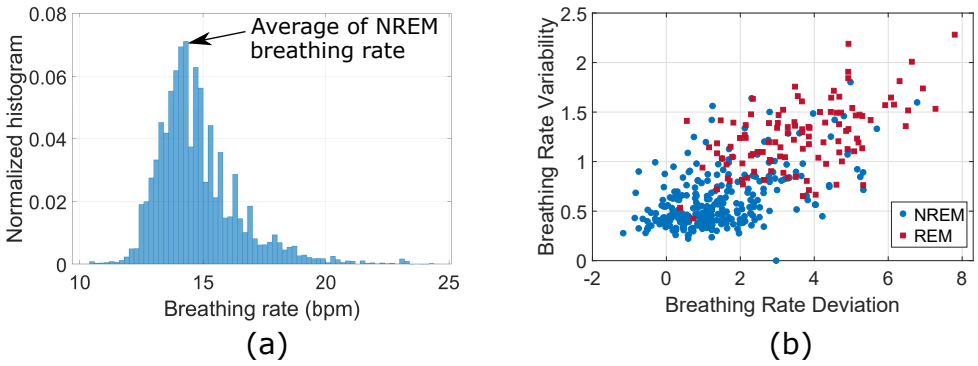

Figure 5.10: Features for REM-NREM classification. (a) The histogram of the breathing estimates of a whole night; (b) the distributions of breathing rate deviation and variability for NREM and REM sleep (each dot represents for an epoch).

for REM/NREM stages classification: Breathing rate is usually faster and exhibits higher variability and irregular patterns for REM stage, while it is more stable and slower for NREM stage.

Since NREM stage constitutes the majority (about 75% to 80%) of total sleep for typical healthy adults (Fig. 5.11) [13], the average breathing rate during NREM stage can be estimated by localizing the peak of the histogram of overnight breathing rate estimates, as shown in Fig. 5.10(a). On this basis, we define *breathing rate deviation*, the distance between the estimated average NREM breathing rate and the 90%-tile of the breathing rate for each epoch, to quantify the deviation of the breathing rate from the baseline during NREM stage.

To extract the variability of the breathing rate for each epoch, we first estimate the trend of breathing rate by applying a low pass filter to the breathing estimates of the whole night, and obtain the detrended breathing rate estimates by subtracting the trend from the original breathing rate estimates. Then, the

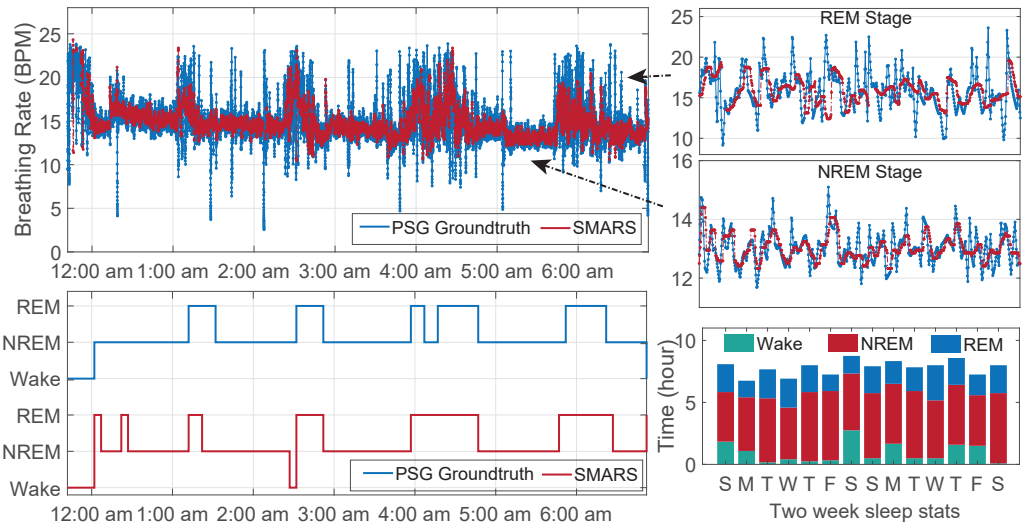

Figure 5.11: An example of SMARS monitoring results

breathing rate variability is defined and calculated for each epoch as the variance of the detrended estimates normalized by the length of epoch.

Fig. 5.10(b) visualizes the distribution of the proposed two features under NREM and REM sleep, respectively. As seen, the majority of the *breathing rate variability* and *breathing rate deviation* of NREM sleep are much smaller than those of REM sleep. Based on these two features, we train a support vector machine (SVM) [20], a widely used binary classifier, to differentiate between REM and NREM sleep.

To be more specific, the radial basis function (RBF) kernel is used in the SVM classifier since the boundary of the two clusters appears to be nonlinear. Since the typical proportion of REM sleep is only about 20% of the total sleep time, the cost of misclassification for the two classes are also adjusted according to their proportion of appearance, that is, the cost of misclassifying REM as NREM is four times larger than that of misclassifying NREM as REM.

5.3.2 Sleep Quality Assessment

When we obtain the estimates of wake, REM, and NREM stages of an overnight sleep, we can assess the elusive sleep quality for a user by following standard approach used in clinical practice. In particular, we calculate the sleep score for each night based on the recognized sleep stages as follows. Let T_N, T_R and T_W denote the durations (measured in hours) of NREM sleep, REM sleep and wake, respectively. Since there is no standard formula for sleep score calculation, a simple formula for the sleep score is applied in SMARS [4] [50]:

$$S = 10 * T_N + 20 * T_R - 10 * T_W, \tag{5.18}$$

which means that longer sleep time and REM duration, less awake time will result in better sleep score. According to recent research [57], REM sleep is crucial for mental recovery, and thus a higher weight has been assigned to REM sleep.

SMARS envisions a practical sleep monitoring for daily in-home use. Although it does not make much sense to compare the sleep score among different users, the trend or history of the sleep score for a particular user would reflect the changes of his/her sleep quality. We believe such results provide clinically meaningful evidences to help diagnose sleep disorders and manage personal health, in an attractive way.

5.4 Experimental Evaluation

In this section, we present the system implementation and experimental evaluation of SMARS. We first conduct field studies to evaluate the performance of SMARS and compare it with medical PSG devices as well as other commercial solutions. We then present overnight case studies in 6 homes to show SMARS's capability of monitoring and staging sleep in real-world scenarios.

5.4.1 Implementation

We implement a comprehensive system on compact embedded devices for rapid real-world deployment. The devices run Linux with the 3.18.71 kernel and are equipped with commodity Atheros WiFi chipsets. We modify the driver to expose CSI, which is reported with 114 subcarriers for channels on 5.8GHz WiFi band. Our system consists of a Tx that by default transmits standard WiFi packets at a rate of 30Hz and an Rx that captures CSI of every packet it received from the Tx. Unless specified otherwise, the Tx is equipped with 2 antennas and the Rx has 3 antennas.

We implement our system in C++, which runs in realtime on the Rx device, calculating the breathing rates and motion statistics as a function of time and sending the data back to a central server via Internet for visualization and sleep staging. The code generates new estimates of both motion and breathing every 1 second. To comprehensively evaluate the performance, we also implement a separate realtime version of Matlab code, in the same logic as the C++ code,

which runs on a Windows laptop.

5.4.2 Methodology

Data Collection. Our data collection involves two parts: First, we carry out extensive real-world case studies by deploying our system in 6 homes (including typical houses and apartments) with 6 willing participants. We have 1 female participant and 5 males, aging from 12 to 31 and weighted from 115 to 195 lbs. In total, we collect 32 nights (a total of about 234 hours) of sleep data. Two of the users contribute more than a week's data. A typical setting of our devices is shown in Fig. 5.2, which will vary from one night to another and from one home to another. The receiver is put close to the bed, while the transmitter is placed within the same room for some settings and outside the bedroom for some others. For every night, the users turn on the system for monitoring when they go to bed and stop it after they get up. During sleep, the subjects wear their daily nightgowns and tuck in typical covers like blankets and quilts as they usually do. In addition, the subjects sleep in a natural way, meaning that they are not instructed to lie in a certain position for a certain time period. Instead, they could move their bodies and change sleep postures at will. Normal environmental changes occur regarding the bedroom settings including bedding, tables, closets, etc, during long-term data collection. We note that our study is conducted in real-world scenarios without making any impractical assumptions, completely different from the controlled and short experiments by previous

works [60, 61, 104, 112, 116, 131, 140]. All human subjects involved in the data collection were approved by our IRB.

Second, we conduct experiments in our lab, a typical office building, to study the coverage of SMARS's motion and breathing detection and further look into the factors which impact the performance. The building contains 10 rooms separated by standard dry walls and furnished with desks, chairs, couches, shelves and computers. During the experiments, there are normal wireless traffics in the air.

To obtain groundtruth labels of sleep stages, we resort to the medical gold standard PSG devices [2]. Participants willing to collect PSG data are dressed with a number of contact sensors that record breathing and sleeping data. During sleep, these sensors and our system are simultaneously recording measurements. In total, we have five nights of PSG data. The PSG data (mainly EEG) is annotated with different sleep stages, according to the AASM specification [1]. Breathing rate is derived by the nasal airflow sensor of PSG.

Open dataset. We also validate our system on a public open dataset (denoted as POD in the following) [41], which was recently released by a real-world comparative study [42] on four state-of-the-art RF-based respiratory monitoring systems. The dataset contains 160 hours of overnight sleep data measured from twenty patients, including 11 male participants and 9 females with respective median ages of 55 and 60 years old. The CSI is measured from a 2×2 MIMO system at a sampling rate of 9.9 Hz, with 114 subcarriers on each antenna pair. The PSG data are clinically labeled with detailed sleep stages. In this dataset, all

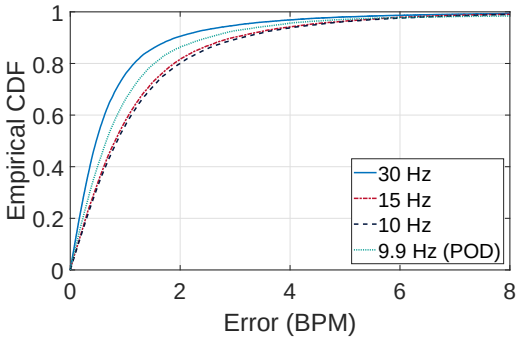

Figure 5.12: Overall accuracy of breathing estimation.

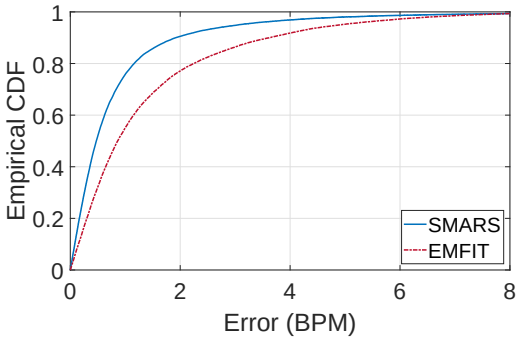

Figure 5.13: Accuracy comparison with EMFIT.

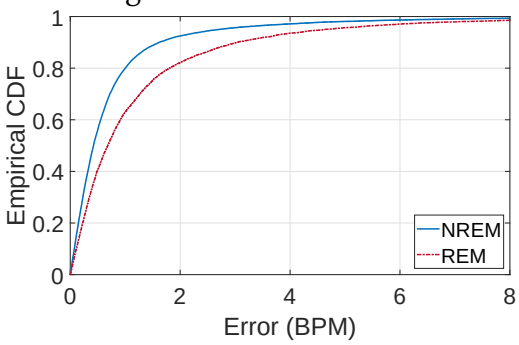

Figure 5.14: Breathing estimation for NREM/REM stage.

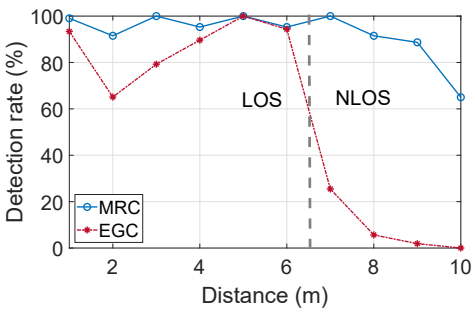

Figure 5.15: The impact of MRC on the sensing coverage.

four RF testbeds are positioned in an optimal way so that the link line between Tx and Rx is perpendicular to and on top of the subject's chest. Further details about the dataset can be found in [41, 42].

Comparison. As our system outperforms the state-of-the-art RF-based sleep monitoring works in terms of accuracy, coverage and robustness to diverse working conditions, we choose to compare with commercial products using radar and contact sensors. Specifically, we select ResMed, which employs low-power radar technology, and EMFIT [4], which embeds an array of EMFi sensors into a mat

that underpins the mattress. The list prices of ResMed (Sleepscore Max) and EMFIT are $149 and $299, respectively. For comparison, we monitor the participant's sleep with multiple systems simultaneously and compare the overnight outputs of individual technologies. ResMed only works in a short range of up to 2 meters. Thus we place it 1 meter away from the subject's chest during our experiments. As ResMed only provides stage data but no raw breathing data, we only compare sleep staging performance with it. As for the open dataset, we compare the performance of SMARS with the results reported in [42].

5.4.3 Breathing Estimation Performance

5.4.3.1 Overall Performance

We study and compare the overall performance of SMARS with the state-of-the-art works and commercial products.

Accuracy. We evaluate the accuracy of breathing rate estimation on both our own measurements and the open dataset. As shown in Fig. 5.12, evaluation based on our own data demonstrates that SMARS achieves a remarkably high accuracy. In particular, the median error is 0.47 bpm and the 95%-tile error is only 2.92 bpm, using a sampling rate of 30Hz. Fig. 5.12 also shows the results based on the open dataset, which demonstrates similar performance with a median error of 0.66 bpm and 95%tile error of 3.79 bpm. The accuracy is slightly worse since a lower sampling rate of 9.9 Hz is used in the open dataset. As comparison, the real-world study in [42] reported that the best existing system still produces

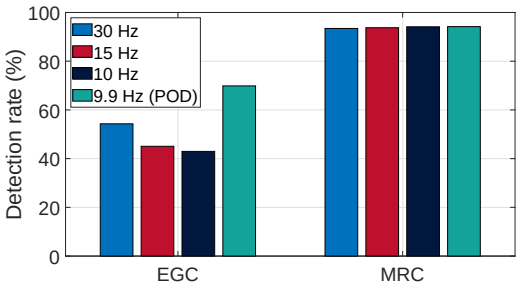

Figure 5.16: The impacts of different sampling rates.

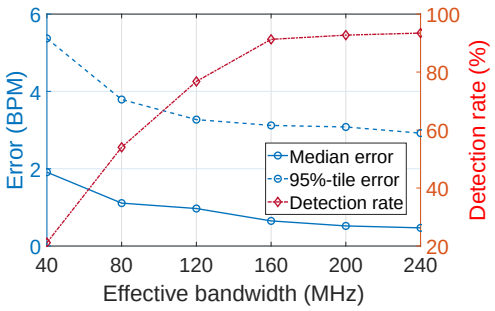

Figure 5.17: The impact of effective bandwidth.

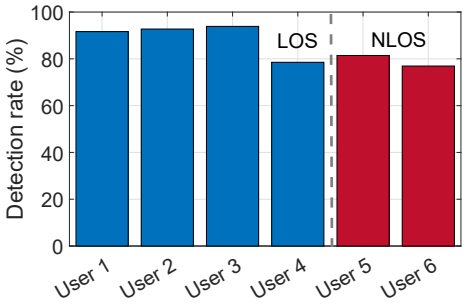

Figure 5.18: The breathing detection ratio for six users.

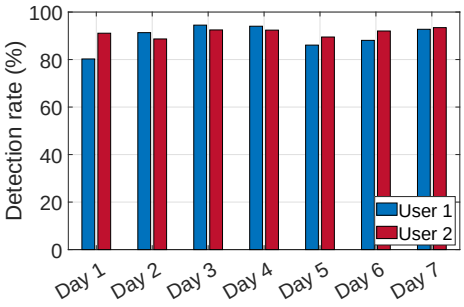

Figure 5.19: One week monitoring for 2 users.

a considerable median error of 2~3 bpm and a 95%-tile error of about 10 bpm under the same settings.

Besides exceeding existing research proposals, our solution also produces considerably better performance than commercial products based on contact sensors. Specifically, as shown in Fig. 5.13, SMARS outperforms EMFIT by 0.39 bpm in median error and 1.86 bpm in 95%-tile error. The result is somewhat counter-intuitive since contact sensors should be better in principle. The sensor array of EMFIT, however, is vulnerable to sleeping position and posture, leading to occasionally unreliable estimates during sleep. In contrast, as detailed subsequently,

SMARS is more robust regarding sleep position.

Instantaneity. Past works on breathing estimation cannot capture instantaneous respiratory rate changes. A person's breathing rate, however, could change dramatically, especially during REM stage (as measured by PSG in Fig. 5.11). Thus it is interesting to understand SMARS' capability of track instantaneously varying breathing rate, which is critical to sleep staging. For this purpose, we compare the respective estimation accuracy in REM stage that usually observes fast changing breathing and NREM stage that normally observes relatively stable breathing. As illustrated in Fig. 5.14, SMARS maintains consistently high accuracy, regardless of stable or varying breathing. Although the estimation errors slightly increase with fast changing breathing (during REM stage), the median error is under 0.7 bpm and, more importantly, the changing trend is precisely captured (See upper right of Fig. 5.11). SMARS outputs one estimate per second in realtime. It takes 0.14 s to process one-second data on a laptop with Intel Core i7 processor and 16 GB memory (Matlab version).

Coverage. SMARS enlarges the sensing coverage to an unparalleled level thanks to its MRC scheme. To quantitatively understand the effective coverage, we conduct experiments in a typical office building. We put a Tx and a Rx, separate by 8.0 m, and monitor a subject's breathing when he sits at locations that are from 1 to 10 meters away to the link line. We use *detection rate*, defined as the percentage of time when the breathing rate is successfully picked up to the total amount of sleep time, to evaluate the coverage. As shown in Fig. 5.15, SMARS achieves a detection rate above 90% when the subject is 8 meters away and still

retains 88.7% and 65% at distances of 9m and 10m, respectively. Note that for distances larger than 6 m, the subject is in another room and has no LOS view to the Tx-Rx link. The coverage is even better than systems using FMCW radar that covers 8m [10], not to mention previous WiFi-based approaches that only work when the Tx and Rx are both positioned next to a person with the formed link line fairly close to the person's chest. Although the coverage would be slightly different under different settings (e.g., device placement), our measurements already demonstrate extraordinary coverage that is more than sufficient for practical applications.

Robustness. With the goal of staging sleep, it is critical to continuously monitor breathing throughout the whole night. As verified by [42], however, previous works have frequent periods when breathing cannot be reliably detected. Thus, in addition to the accuracy, we would like to understand how robust SMARS is to natural overnight sleep, during which the subject would change postures and move body. As shown in Fig. 5.18, SMARS consistently reliably detects breathing for 6 different subjects at 6 homes that differ not only in device settings but also in building structure, layout, bedding, and furnitures, etc. In particular, even in NLOS condition for user 5 and 6 who place the Tx inside the closed closet and outside the bedroom respectively, SMARS yields more than 80% detection rates. Furthermore, Fig. 5.19 depicts that breathing detection rate for two users' one week data, which demonstrates robustly high detection rate over different nights of natural sleeping. These results suggest that our model is independent of environments and subjects, and is capable of adapting to various scenarios.

5.4.3.2 Parameter Study

In the following, we examine the key factors that impact the performance of SMARS' breathing estimation.

Impact of MRC. MRC is a key module that improves the accuracy, coverage, and robustness of SMARS. We examine the benefits of MRC by comparing with an Equal Gain Combining (EGC) policy, which basically averages over all subcarriers. As depicted in Fig. 5.15, MRC remarkably boosts the detection rate in NLOS scenarios (cases with distances >7m in Fig. 5.15) by more than 65% compared to EGC. Fig. 5.16 further demonstrates significant gains brought by MRC on overnight data. By using MRC, SMARS consistently maintains high detection rates of >90%, regardless of sampling rates of 30Hz, 20Hz, or 10Hz. By comparison, the detection rate of EGC is less than 70% when sampling rate is 30Hz. While MRC largely improves the detection rate and thus extends the coverage and facilitates the robustness, it provides marginal improvement in accuracy. Specifically, the median accuracy is improved by 0.1 bpm with MRC compared to EGC. The reason is that, as long as breathing can be detected, our ACF-based approach will yield accurate estimate.

Impact of Sampling Rate. We study the impacts of sampling rate on SMARS. As shown in Fig. 5.12, the median accuracy of breathing estimation decreases from 0.47 bpm to 0.85 bpm when the sampling rate decreases from 30Hz to 10Hz. The detection rate, as shown in Fig. 5.16, does not change too much with respect to sampling rate. Note that both the accuracy and detection rate on

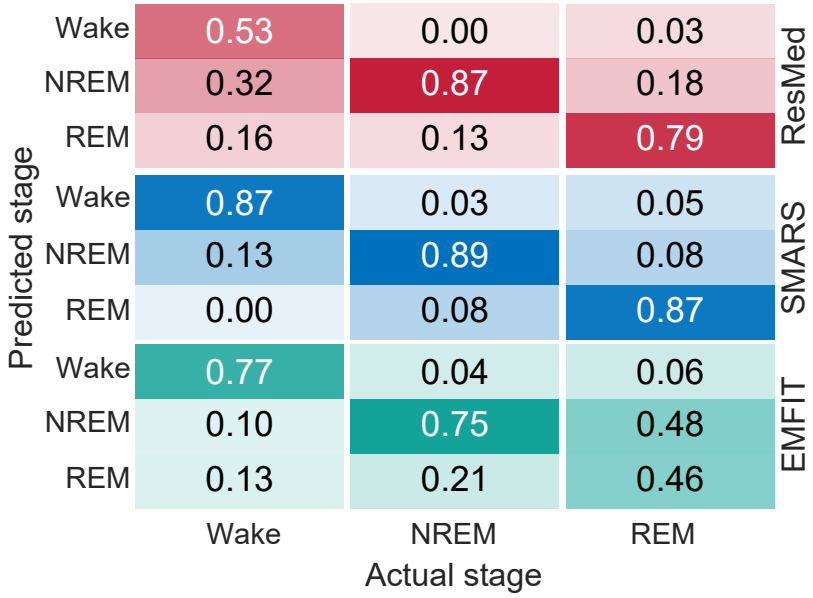

Figure 5.20: Confusion matrix of ResMed, SMARS, and EMFIT.

the open dataset with 9.9Hz sampling rate are better than our self-collected data. This is because the open dataset was collected in an optimal setting for previous works, i.e., the Tx and Rx were placed exceedingly close to each other and to the subject, while we deploy the devices in a natural and comfortable manner during our data collection. To conclude, a higher sampling rate will yield better performance while 30Hz or even 10Hz is adequate in practice.

Impact of Effective Bandwidth. We study the impacts of frequency diversity attributed by antennas via effective bandwidth defined as $W_e \triangleq N_s B$, where N_s denotes the number of spatial streams between the Tx and Rx, and B denotes the bandwidth of each stream (40MHz in our system). Fig. 5.17 shows that with the increasing of effective bandwidth, the median error and 95%-tile error decrease, and at the same time, the detection rate increases. The results suggest that a

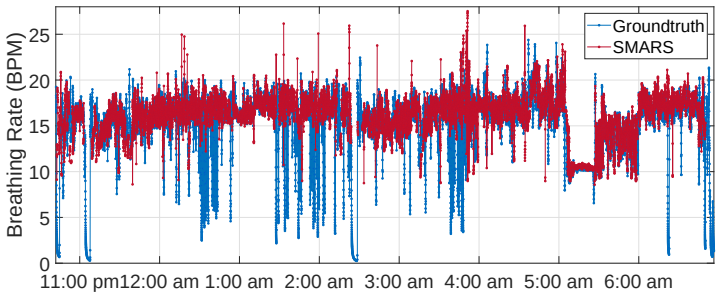

Figure 5.21: The breathing monitoring result for a typical patient in the open dataset.

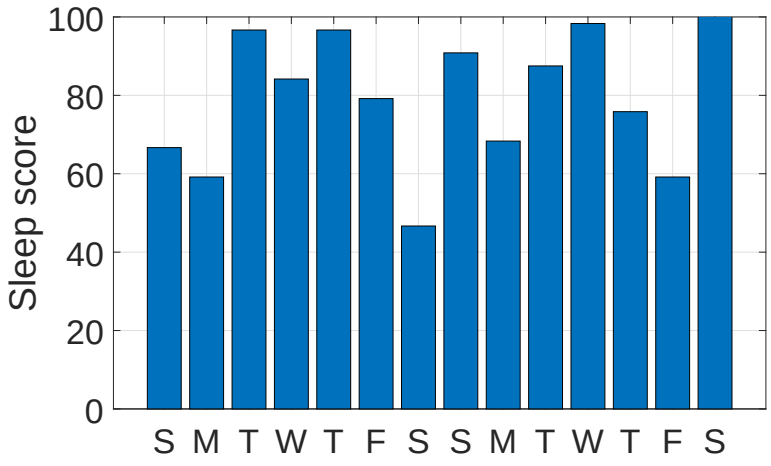

Figure 5.22: Sleep quality assessment over two weeks.

2×2 MIMO system (i.e., 160MHz effective bandwidth) is sufficient for SMARS to achieve a remarkable performance.

5.4.4 Sleep Staging Performance

In this section, we evaluate the performance in sleep staging and compare with commercial products. We further carry out a two-week case study for long-term daily sleep monitoring.

5.4.4.1 Sleep Stage Recognition Accuracy

We summarize the accuracy of SMARS compared to two commercial products EMFIT and ResMed in Tab. 5.1. Fig. 5.20 shows the more detailed confusion matrices. As seen, SMARS yields an overall accuracy of 88.4% in sleep staging, outperforming commercial solutions EMFIT and ResMed, which use contact sensors and UWB radar respectively. In particular, SMARS achieves a recognition accuracy of 87%, 89% and 87% for wake/NREM/REM detection respectively, which is better than EMFIT and ResMed. Note that EMFIT performs staging with additional heart rate measurements, ResMed further incorporates microphones (from their smartphone App), while SMARS purely relies on breathing and motion estimation.

Regarding the public open dataset, SMARS does not perform sleep staging well for those patients, although remarkable accuracy in breathing estimation is achieved. This is because, for those patients with severe diseases, such as sleep

Table 5.1: Comparison of different sleep monitoring systems.

	Overall	Wake	Sleep	REM	NREM
SMARS	88.4%	86.7%	96.3%	86.9%	89.1%
EMFIT	69.8%	76.7%	98.2%	46.3%	74.9%
ResMed	81.2%	52.6%	95.3%	78.9%	87.2%

apnea, their breathing pattern is not only affected by sleep stages but also by the inherent, erratic chest movement and abnormal respiration caused by the diseases. Fig. 5.21 illustrates the overnight breathing, both the ground truths and our estimates, for an elderly patient. As seen, the breathing patterns fluctuate and do not exhibit distinguishable patterns we observed in healthy subjects as in Fig. 5.11. As a consequence, the natural relationship between breathing patterns and sleep stages no longer holds for this patient. In the future, we intend to study SMARS on a broad spectrum of patients, ranging from normals to those with chronic sleep disorders. From these studies, we hope to unveil the capabilities of SMARS as a diagnostic instrument, and also as a supplementary health monitoring technology.

5.4.4.2 Long-term Daily Sleep Assessment

To demonstrate the capability of SMARS for daily sleep monitoring, we carry out a two-week case study for a specific user. Every night, the participant sleeps with our system running. During the data collection, the bedroom envi-

ronments, device locations, in addition to the bedding and his nightclothes will change from night to night. Here we assess the user's sleep quality by calculating the sleep score as specified in (5.18). Fig. 5.22 illustrates the historical scores over the two-week term. Based on these quantitative sleep quality statistics, SMARS offers useful data for personal healthcare.

5.5 Summary

This chapter presents the design, implementation, and evaluation of S-MARS, the first practical sleep monitoring system that exploits ambient radio signals to recognize sleep stages, without instrumenting users' body or the bed. SMARS achieves this goal by monitoring breathing and body movements during sleep accurately and instantaneously, to a level of performance previously only attainable with expensive specialized infrastructure. A key enabler behind is a statistical model that considers all reflection and scattering multipaths indoors without making unrealistic assumptions. We implement SMARS on commercial WiFi chipsets and validate its performance by extensive experiments with 32 nights data collected in 6 homes. We believe SMARS takes a promising step towards practical in-home sleep monitoring.

Chapter 6: Indoor Tracking: a Time-Reversal Focusing Ball Approach

With the proliferation of the Internet of Things (IoT) applications, Indoor Positioning and Indoor Navigation (IPIN) has received an increasing attention in recent years. Technavio forecasts the global IPIN market to grow to USD 7.8 billion by 2021 [3], and more than ever before, enterprises of all sizes are investing in IPIN technology to support a growing list of applications, including patient tracking in hospitals, asset management for large groceries, workflow automation in large factories, navigation in malls, appliance control, etc.

Although Global Positioning System (GPS) can achieve good accuracy with a low cost in outdoor real-time tracking, such a good balance between the cost and performance has not been realized for indoor tracking yet [25].

In this chapter, we propose WiBall, a wireless system for indoor tracking, that can work well in both none-line-of-sight (NLOS) and line-of-sight (LOS) scenarios and is robust to environmental dynamics as well. WiBall estimates the incremental displacement of the device at every moment, and thus, it can track the trace of the device in real time. WiBall adopts a completely new paradigm in the moving distance estimation, which is built on the proposed discovered physi-

cal phenomenon of radio signals. In the past, the moving distance estimation can be done by analyzing the output of IMU that is attached to the moving object. Accelerometer readings are used to detect walking steps and then, the walking distance can be estimated by multiplying the number of steps with the stride length [105]. However, pedestrians often have different stride lengths that may vary up to 40% even at the same speed, and 50% with various speeds of the same person [130]. Thus calibration is required to obtain the average stride lengths for different individuals, which is impractical in real applications and thus has not been widely adopted. The moving distance can also be estimated by analyzing radio signals that are affected by the movement of the device. Various methods have been proposed based on the estimation of the maximum Doppler frequency, such as level crossing rate methods [73], covariance based methods [85] [120], and wavelet-based methods [68]. However, the performance of these estimators is unsatisfactory in practical scenarios. For example, the approach in [120] can only differentiate whether a mobile station moves with a fast speed ($\geq$ 30km/h) or with a slow speed ($\leq$ 5km/h).

In WiBall, a new scheme for moving distance estimation based on the time-reversal (TR) resonating effect [58] [102] is proposed. TR is a fundamental physical resonance phenomenon that allows people to focus the energy of a transmitted signal at an intended focal spot, both in the time and spatial domains, by transmitting the TR waveform. The research of TR can be traced back to the 1950s when it was first utilized to align the phase differences caused by multi-path fading during long-distance information transmissions. The TR resonating

effect was first observed in a practical underwater propagation environment [84] that the energy of a transmitted signal can be refocused at the intended location because by means of TR the RX recollects multipath copies of a transmitted signal in a coherent matter.

In this chapter, we present a new discovery that the energy distribution of the TR focusing effect exhibits a location-independent property, which is only related to the physical parameters of the transmitted EM waves. This is because the number of multipath components (MPC) in indoors is so large that the randomness of the received energy at different locations can be averaged out as a result of the law of large numbers. Based on this location-independent feature, WiBall can estimate the moving distance of the device in a complex indoor environment without requiring any pre-calibration procedures. To cope with the cumulative errors in distance estimation, WiBall incorporates the constraints imposed by the floorplan of buildings and corrects the cumulative errors whenever a landmark, such as a corner, hallway, door, etc., is met. Combining the improved distance estimator and the map-based error corrector, the proposed WiBall is shown to be able to achieve decimeter-level accuracy in real-time tracking regardless of the moving speed and environment.

The rest of the chapter is organized as follows. Section 6.1 introduces the system model of the proposed WiBall and also the TR principle for speed estimation. Section 6.2 presents an IMU-based moving direction estimator and a map-based localization corrector, which can correct the accumulated localization error. Experimental evaluation is shown in Section 6.3 and Section 6.4 summa-

rizes this chapter.

6.1 System Model

In this section, we first introduce the overall system architecture of WiBall and the TR radio system. Then, we derive the analytical normalized energy distribution of the TR focal spot. We show that the normalized energy distribution is location-independent and can be used to estimate distance. Last, we discuss the TR-based distance estimator.

6.1.1 Overview of WiBall

WiBall consists of a transmitter (TX) broadcasting beacon signals periodically to all the RXs being tracked. WiBall estimates the paths that the RX travels, i.e., the location of the RX $\vec{\mathbf{x}}$ at time t_i is estimated as

$$\vec{\mathbf{x}}(t_i) = \vec{\mathbf{x}}(t_{i-1}) + \vec{\Delta}(t_i), \tag{6.1}$$

where $\vec{\mathbf{x}}(t_{i-1})$ represents the location of the RX at the previous time t_{i-1}, and $\Delta(t_i)$ is the incremental displacement. The magnitude of $\vec{\Delta}(t_i)$, denoted as $d(t_i)$, and the angle of $\vec{\Delta}(t_i)$, denoted as $\theta(t_i)$, correspond to the moving distance and the change of moving direction of the RX from t_{i-1} to t_i, respectively. As shown in Fig. 6.1, the location of the RX at time t_n is computed based on the accumulative displacements from time t_0 to t_n and the initial start point $\vec{\mathbf{x}}(t_0)$.

WiBall estimates the moving distance $d(t_i)$ based on the TR resonating effect, which can be obtained from the CSI measurements at the RX. The estimation

of $\theta(t_i)$ is based on the angular velocity and gravity direction from IMU, which is a built-in module for most smartphones nowadays.

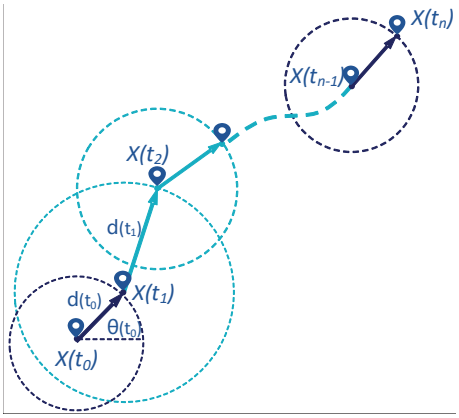

Figure 6.1: Illustration of the tracking procedure.

6.1.2 TR Radio System

Consider a rich-scattering environment, e.g., an indoor or metropolitan area, and a wireless transceiver pair each equipped with a single omnidirectional antenna. Given a large enough bandwidth, the MPCs in a rich-scattering environment can be resolved into multiple taps in discrete-time and let $h(l; \vec{T} \to \vec{R}_0)$ denote the l-th tap of the channel impulse response (CIR) from $\vec{T}$ to $\vec{R}_0$, where $\vec{T}$ and $\vec{R}_0$ denotes the coordinates of the TX and RX, respectively. In the TR transmission scheme, the RX at $\vec{R}_0$ first transmits an impulse and the TX at $\vec{T}$ captures the CIR from $\vec{R}_0$ to $\vec{T}$. Then the RX at $\vec{T}$ simply transmits back the time-reversed and conjugated version of the captured CIR, i.e., $h^*(-l; \vec{R}_0 \to \vec{T})$, where $*$ denotes complex conjugation. With channel reciprocity, i.e., the forward and backward channels are identical [119], the received signal at any location $\vec{R}$ when the TR

waveform $h^*(-l;\vec{R}_0 \to \vec{T})$ is transmitted can be written as [31]

$$s(l;\vec{R}) = \sum_{m=0}^{L-1} h(m;\vec{T} \to \vec{R}) h^*(m-l;\vec{R}_0 \to \vec{T}), \tag{6.2}$$

where L is the number of resolved multipaths in the environment. When $\vec{R} = \vec{R}_0$ and $l = 0$, we have $s(0;\vec{R}) = \sum_{m=0}^{L-1} |h(m,\vec{T} \to \vec{R}_0)|^2$ with all MPCs added up coherently, i.e., the signal energy is refocused at a particular spatial location at a specific time instance. This phenomenon is termed as the TR spatial-temporal resonating effect [135] [127].

To study the TR resonating effect in the spatial domain, we fix time index $l = 0$ and define the TR resonating strength (TRRS) between the CIRs of two locations $\vec{R}_0$ and $\vec{R}$ as the normalized energy of the received signal when the TR waveform for location $\vec{R}_0$ is transmitted:

$$\begin{aligned} &\eta(\mathbf{h}(\vec{R}_0), \mathbf{h}(\vec{R})) \\ &= \left| \frac{s(0;\vec{R})}{\sqrt{\sum_{l_1=0}^{L-1} |h(l_1;\vec{T} \to \vec{R}_0)|^2} \sqrt{\sum_{l_2=0}^{L-1} |h(l_2;\vec{T} \to \vec{R})|^2}} \right|^2, \end{aligned} \tag{6.3}$$

where we use $\mathbf{h}(\vec{R})$ as an abbreviation of $h(l;\vec{T} \to \vec{R})$, $l = 0, ..., L-1$, when $\vec{T}$ is fixed. Note that the range of TRRS is normalized to be $[0, 1]$ and TRRS is symmetric, i.e., $\eta(\mathbf{h}(\vec{R}_0), \mathbf{h}(\vec{R})) = \eta(\mathbf{h}(\vec{R}), \mathbf{h}(\vec{R}_0))$.

We built a pair of customized TR devices to measure the TRRS at different locations, as shown in Fig. 6.2(a). The devices operate at $f_0 = 5.8$GHz ISM band with 125MHz bandwidth, and the corresponding wavelength is $\lambda = c/f_0 = 5.17$cm. The RX is placed on a 5 cm $\times$ 5 cm square area above a channel probing

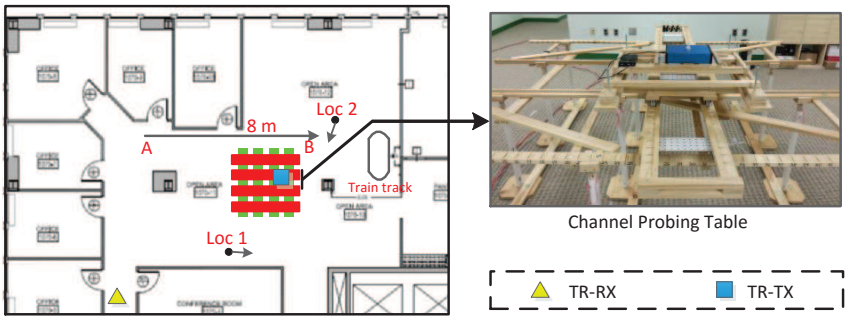

(a) TR prototype and channel probing platform.

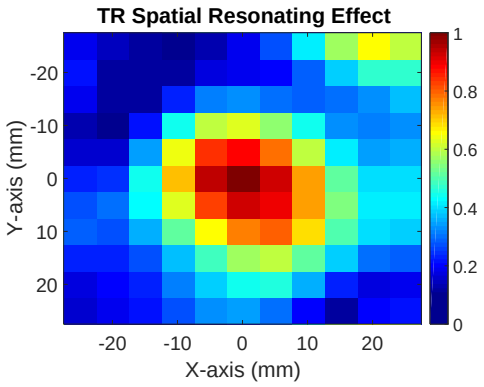

(b) TRRS in spatial domain.

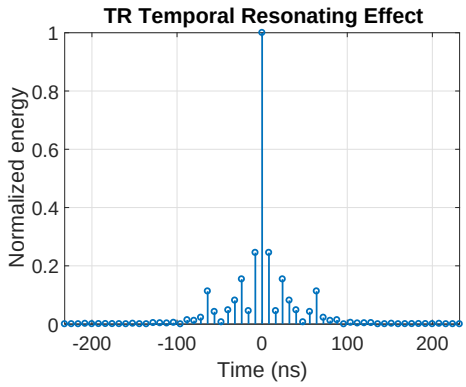

(c) TRRS in time domain.

Figure 6.2: TR prototype and the environment of the measurement, the TRRS distribution in the spatial domain, and the normalized energy of the received signal at the focal spot $\vec{R}_0$ in the time domain.

table with 0.5cm resolution, and the center of the square is set to be the focal spot $\vec{R}_0$. The TRRS distribution around $\vec{R}_0$ in the spatial domain and the normalized received energy at $\vec{R}_0$ in the time domain are shown in Fig. 6.2(b) and Fig. 6.2(c), respectively. As we can see from the results, the received energy is concentrated around $\vec{R}_0$ both in spatial and time domains almost symmetrically, which shows that a bandwidth of 125MHz is able to achieve the TR resonating effect in a typical indoor environment.

6.1.3 Energy Distribution of TR Focal Spot

Assume that all the EM waves propagate in a far-field zone, and then each MPC can be approximated by a plane EM wave. For the purpose of illustration, the receive antenna is placed in the origin of the space and each MPC can be represented by a point in the space whose coordinate is determined by its angle of arrival and propagation distance, e.g., the point A, as shown in Fig. 6.3, where r stands for the total traveled distance of the MPC, θ denotes the direction of arrival of the MPC, and $G(\omega)$ denotes the power gain with $\omega = (r, \theta)$. In a rich-scattering environment, we can also assume that ω is uniformly distributed in the space and the total number of MPCs is large. When a vertically polarized antenna is used, only the EM waves with the direction of electric field orthogonal to the horizontal plane are collected. Then, the received signal is just a scalar sum of the electric field of the impinging EM waves along the vertical direction. In the sequel, without loss of generality, we only consider the TRRS distribution in the horizontal plane since its distribution in the vertical plane is similar.

For a system with bandwidth B, two MPCs would be divided into different taps of the measured CIR as long as the difference of their time of arrival is larger than the sampling period $1/B$, that is, any two MPCs with a difference of their traveled distances larger than c/B can be separated. With a sufficiently large system bandwidth B, the distance resolution c/B of the system is so small that all of the MPCs with significant energy can be separated in the spatial domain, i.e., each significant MPC can be represented by a single tap of a measured CIR.

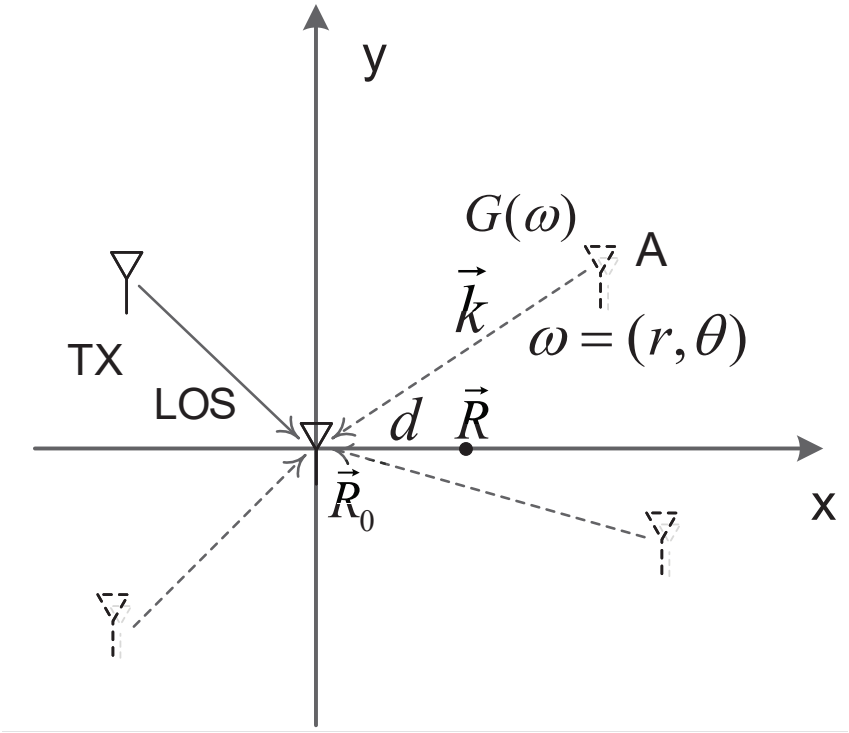

Figure 6.3: Illustration of the polar coordinates in the analysis.

Assume that the distribution of the energy of each MPC is uniform in direction θ, i.e., the distribution of $G(\omega)$ is only a function of r. Then the energy of MPCs coming from different directions would be approximately the same when the number of MPCs is large. Mathematically, for any point $\vec{R}$ in a source-free region with constant mean electric and magnetic fields, the channel impulse response when a delta-like pulse is transmitted can be written as [31]

$$\begin{aligned} & h(t; \vec{T} \to \vec{R}) \\ = & \sum_{\omega \in \Omega} G(\omega) q(t - \tau(\omega)) e^{i(2\pi f_0 (t - \tau(\omega)) - \phi(\omega) - \vec{k}(\omega) \cdot \vec{R})}, \end{aligned} \tag{6.4}$$

where $q(t)$ is the pulse shaper, $\tau(\omega) = r/c$ is the propagation delay of the MPC ω, f_0 is the carrier frequency, Ω is the set of MPCs, $\phi(\omega)$ is the change of phase due

to reflections and $\vec{k}(\omega)$ is the wave vector with amplitude $k = c/f_0$. Accordingly, the l-th tap of a sampled CIR at location $\vec{R}$ can be expressed as

$$\begin{aligned} & h(l;\vec{T}\rightarrow\vec{R}) \\ = & \sum_{\tau(\omega)\in[lT-\frac{T}{2},lT+\frac{T}{2})} G(\omega)q(\Delta\tau(l,\omega))e^{i(2\pi f_0\Delta\tau(l,\omega)-\phi(\omega)-\vec{k}(\omega)\cdot\vec{R})} \end{aligned} \tag{6.5}$$

where T is the channel measurement interval and $\Delta\tau(l,\omega) = lT - \tau(\omega)$ for $l = 0,1,...,L-1$. When the TR waveform $h^*(-l;\vec{R}_0\rightarrow\vec{T})$ is transmitted, the corresponding received signal at the focal spot $\vec{R}_0$ can be written as

$$\begin{aligned} & s(0;\vec{R}) \\ = & \sum_{l=1}^{L}\left|\sum_{\tau\in[lT-\frac{T}{2},lT+\frac{T}{2})} G(\omega)q(\Delta\tau(l,\omega))e^{i(2\pi f_0\Delta\tau(l,\omega)-\phi(\omega))}\right|^2. \end{aligned} \tag{6.6}$$

(6.6) shows that the MPCs with propagation delays $\tau(\omega)\in[lT-\frac{T}{2},lT+\frac{T}{2})$ for each l would be merged into one single tap, and the signals coming from different taps would add up coherently while the MPCs within each sampling period T would add up incoherently. It indicates that the larger the bandwidth, the larger the TR focusing gain that can be achieved, since more MPCs can be aligned and added up coherently. When the bandwidth is sufficiently large, the received signal at each point $\vec{R}$ can be approximated as

$$s(0;\vec{R}) \approx \sum_{l=1}^{L}|G(\omega)q(\Delta\tau(l,\omega))|^2 e^{-i\vec{k}(\omega)\cdot(\vec{R}-\vec{R}_0)}. \tag{6.7}$$

When a rectangular pulse shaper is used, i.e., $q(t) = 1$ for $t\in[-\frac{T}{2},\frac{T}{2})$ and $q(t) = 0$ otherwise, under the above symmetric scattering assumption the received signal

$s(0;\vec{R})$ can thus be approximated as

$$\begin{aligned} s(0;\vec{R}) &= \sum_{\omega\in\Omega} |G(\omega)|^2 e^{-i\vec{k}\cdot(\vec{R}-\vec{R}_0)} \\ &\approx \int_0^{2\pi} P(\theta) e^{-ikd\cos(\theta)} d\theta \\ &= PJ_0(kd), \end{aligned} \tag{6.8}$$

where the coordinate system in Fig. 6.3 is used, Ω stands for the set of all significant MPCs, $J_0(x)$ is the 0^{th}-order Bessel function of the first kind, and d is the Euclidean distance between $\vec{R}_0$ and $\vec{R}$. Here we use a continuous integral to approximate the discrete sum and $P(\theta) = P$ denotes the density of the energy of MPCs coming from direction θ. For $\vec{R} = \vec{R}_0$, it degenerates to the case of $d = 0$ and thus $s(0;\vec{R}_0) \approx P$. Since the denominator of (6.3) is the product of the energy received at two focal spots, it would converge to P^2. At the same time, the numerator is approximately $P^2 J_0^2(kd)$ as discussed above. As a result, the TRRS defined in (6.3) can be approximated as

$$\eta(\mathbf{h}(\vec{R}_0), \mathbf{h}(\vec{R})) \approx J_0^2(kd). \tag{6.9}$$

In the following, since the theoretic approximation of the TRRS distribution only depends on the distance between two points, we use $\bar{\eta}(d) = J_0^2(kd)$ to stand for the approximation of TRRS between two points with distance d.

To evaluate the above theoretic approximation, we also built a mobile channel probing platform equipped with stepping motors that can control the granularity of the CIR measurements precisely along any predefined direction. Extensive measurements of CIRs from different locations have been collected in the

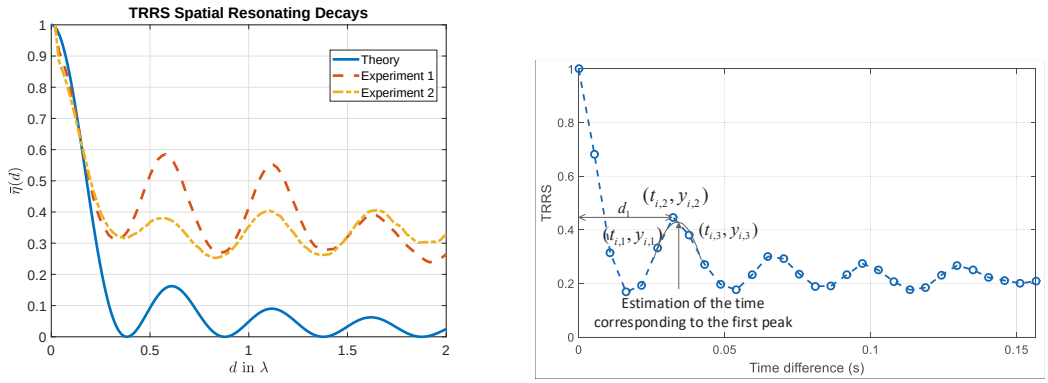

(a) Comparison of the TRRS distribution between experimental results and the theoretical result. Experiments 1 and 2 correspond to Location 1 and Location 2 respectively in Fig. 6.2(a).

(b) Illustration of the proposed TR-based speed estimation algorithm.

Figure 6.4: The distributions of TRRS.

environment shown in Fig. 6.2(a). Fig. 6.4(a) shows two typical experimental results measured at Location 1 and Location 2 with a separation of 10m as shown in Fig. 6.2(a). The distance d away from each predefined focal spot increases from 0 to 2λ with a resolution of 1mm. The measured TRRS distribution functions agree with the theoretic approximation quite well in the way that the positions of the peaks and valleys in the measured curves are almost the same as those of the theoretic curve. Although Locations 1 and 2 are far apart, the measured TRRS distribution functions exhibit similar damping pattern when the distance d increases.

We also observe that the measured TRRS distribution functions are far above 0. This is due to the contribution of the direct path between the TR devices. Therefore, the energy density function $P(\theta)$ in (6.8) consists of a term which

is symmetric in direction due to NLOS components and another term which is asymmetric in direction due to LOS components. As a result, the TRRS is indeed a superposition of $J_0^2(kd)$ and some unknown function which is the result of the asymmetric normalized energy distribution of MPCs in certain directions. Since the pattern of $J_0^2(kd)$, embedded in the TRRS distribution function, is location-independent, we can exploit this feature for speed estimation.

A numerical simulation using a ray-tracing approach is also implemented to study the impact of bandwidth on TRRS distribution. In the simulation, the carrier frequency of the transmitted signals is set to be 5.8 GHz. 200 scatterers are uniformly distributed in a 7.5 m by 7.5 m square area. The reflection coefficient is distributed uniformly and independently in $(0, 1)$ for each scatterer. The distance between the TX and RX is 30 m and the RX (focal spot) is set to be the center of the square area. Fig. 6.5 shows the distributions of TRRS around the focal spot when the system bandwidth 40 MHz, 125 MHz and 500 MHz, respectively. As we can see from the results, as the bandwidth increases, the distribution of TRRS in the horizontal plane becomes more deterministic-like and converges to the theoretical approximations.

6.1.4 TR-Based Distance Estimator

Since the shape of the TRRS distribution function $\bar{\eta}(d) \approx J_0^2(kd)$ is only determined by the wave number k which is independent of specific locations, it can be utilized as an intrinsic ruler to measure distance in the space. Consider that

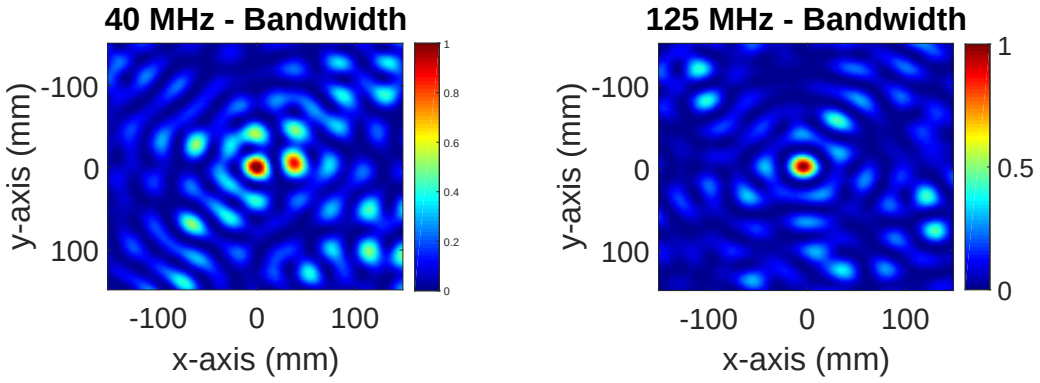

(a) 40 MHz bandwidth.

(b) 125 MHz bandwidth.

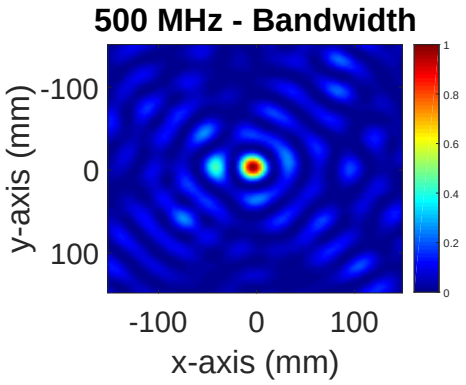

(c) 500 MHz bandwidth.

Figure 6.5: Numerical simulations of the distributions of TRRS with varying bandwidth.

an RX moves along a straight line with a constant speed v starting from location $\vec{R}_0$, and a TX keeps transmitting the TR waveform corresponding to $\vec{R}_0$ at regular intervals. Then, the TRRS measured at the RX is just a sampled version of $\eta(d)$, which would also exhibit the Bessel-function-like pattern, as illustrated in Fig. 6.4(b).

Take the first local peak of $\eta(d)$ for example. The corresponding theoretical distance d_1 is about 0.61λ according to the Bessel-function-like pattern. In order to estimate the moving speed, we only need to estimate how much time $\hat{t}$ it takes for the RX to reach the first local peak starting from point $\vec{R}_0$. We use a quadratic curve to approximate the shape of the first local peak. Combining the knowledge of the timestamps of each CIR measurement, $\hat{t}$ can be estimated by the vertex of the quadratic curve. Therefore, we obtain the speed estimation as $\hat{v} = (0.61\lambda)/\hat{t}$, and then, the moving distance can be calculated by integrating the instantaneous speed over time. One thing to note is that as long as the rate of CIR measurement is fast enough, it is reasonable to assume that the moving speed is constant during the measurement of the TRRS distribution. For example, in Fig. 6.4(b) the duration is about 0.16 seconds.

In practice, the channel is not measured with a uniform interval and the empirical probability density function (PDF) of the time interval between adjacent channel measurements is shown in Fig. 6.6. To overcome the imperfect channel sampling process, we combine multiple realizations of the TRRS distribution function measured at adjacent time slots to increase the accuracy of the estimation of $\hat{t}$. For the i-th measurement, first find the data points near the first

local peak $(t_{i,j}, y_{i,j})$, $i = 1,...,N$, $j = 1,2,3$, as shown in Fig. 6.4(b), where N is the number of TRRS distribution functions obtained within the window of channel measurements. Then fit the data points with a quadratic regression model $y_{i,j} = \alpha + \beta t_{i,j} + \gamma t_{i,j}^2 + e_{i,j}$, and thus estimation of the elapsed time is $\hat{t} = -\hat{\beta}_{\text{LS}}/(2\hat{\gamma}_{\text{LS}})$, where $\hat{\beta}_{\text{LS}}$ and $\hat{\gamma}_{\text{LS}}$ are the least-square estimators of β and γ, respectively. Different reference points can be used as well, such as the first local valley, the second local peak and so on, to increase the accuracy of estimation. Therefore, the moving distance at time t can be estimated as $\hat{d}(t) = \hat{v}(t)\Delta t$, where Δt denotes the time duration between the current packet and the previous packet. The procedures of the proposed TR-based distance estimator has been summarized in the flowchart shown in Fig. 6.7.

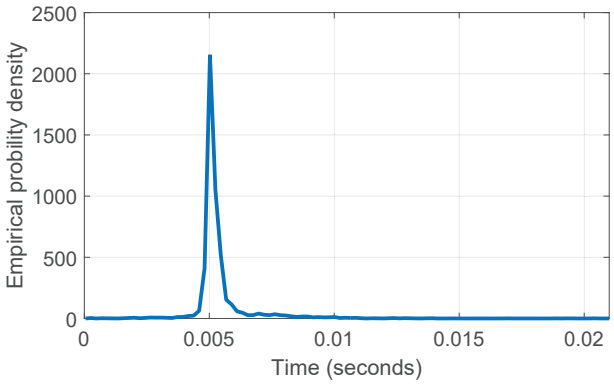

Figure 6.6: Empirical probability density for time intervals between adjacent packets.

Note that besides taking advantage of TR spatial focusing effect, the proposed distance estimator also exploits the physical properties of EM waves and thus does not require any pre-calibration, while the estimator presented in our

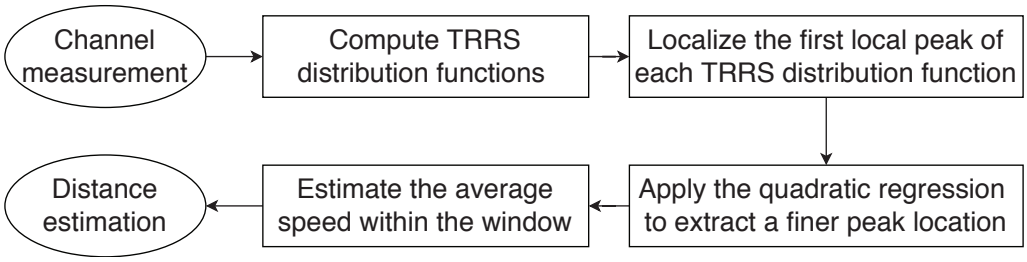

Figure 6.7: Flowchart of the TR-based distance estimator.

previous work [135] needs to measure the TRRS spatial decay curve in advance.

6.2 Direction Estimation and Map-Assisted Error Correction

In this section, we introduce the other two key components of WiBall: the IMU-based moving direction estimator and the map-based position corrector.

6.2.1 IMU-based Moving Direction Estimator

If the RX is placed in parallel to the horizontal plane, the change of moving direction can be directly measured by the readings of the gyroscope in the z-axis, i.e., $\theta(t_i) = \omega_z(t_{i-1})(t_i - t_{i-1})$, where $\omega_z(t_{i-1})$ denotes the angular velocity of the RX with respect to z-axis in its local coordinate system at time slot t_{i-1}. However, in practice, the angle of the inclination between the RX and the horizontal plane is not zero, as shown in Fig. 6.8, and WiBall needs to transform the rotation of the RX into the change of the moving direction in the horizontal plane. Since the direction of the gravity $\vec{\mathbf{g}}/\|\vec{\mathbf{g}}\|$ can be estimated by the linear accelerometer, the rotation of the RX in the horizontal plane, which is orthogonal to the $\vec{\mathbf{g}}/\|\vec{\mathbf{g}}\|$, can be obtained by projecting the angular velocity vector $\vec{\boldsymbol{\omega}} = \omega_x\hat{\mathbf{x}} + \omega_y\hat{\mathbf{y}} + \omega_z\hat{\mathbf{z}}$

with respect to its local coordinate system onto the direction $\vec{\mathbf{g}}/\|\vec{\mathbf{g}}\|$. Therefore, the change of moving direction $\theta(t_i)$ is obtained as

$$\theta(t_i) = \frac{\vec{\omega}^T(t_{i-1})\vec{\mathbf{g}}(t_{i-1})}{\|\vec{\mathbf{g}}(t_{i-1})\|} \cdot (t_i - t_{i-1}), \tag{6.10}$$

where $\vec{\omega}(t_{i-1})$ and $\vec{\mathbf{g}}(t_{i-1})$ denote the vector of angular velocity and the gravity at time t_{i-1}, respectively.

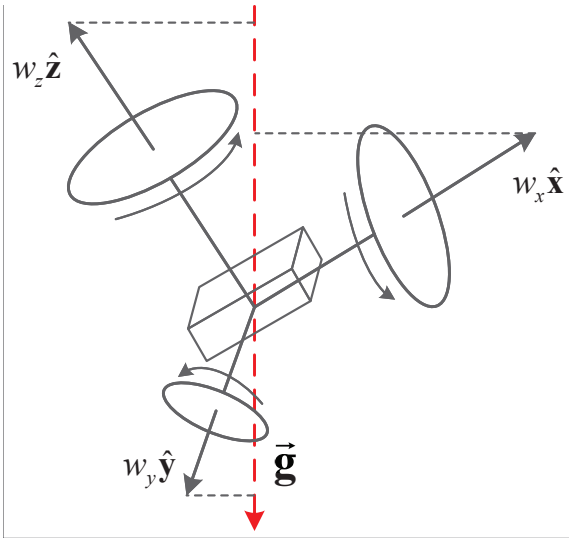

Figure 6.8: Transforming the rotation of RX into the moving direction in horizontal plane.

6.2.2 Map-based Position Corrector

Since WiBall estimates the current location of the RX based on the previous locations, its performance is limited by the cumulative error. However, for typical indoor environments, there are certain constraints in the floorplan which can be utilized as landmarks and thus, the cumulative errors may be corrected correspondingly as long as a landmark is identified. For example, Fig. 6.9 shows

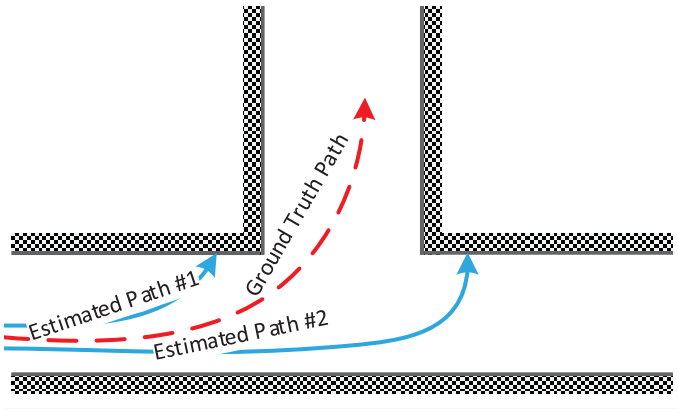

Figure 6.9: Two possible estimated paths and the ground truth path.

a T-shaped corridor and two possible estimated paths are illustrated in the figure. The moving distance of path #1 is underestimated and that of path #2 is overestimated, while the dotted line corresponds to the ground truth path. Both of the estimated traces would penetrate the wall in the floorplan if the errors are not corrected, which violates the physical constraints imposed by the structure of the building. In these two cases, a reasoning procedure can be implemented and WiBall tries to find the most possible path that can be fitted to the floorplan where all the border constraints imposed by the floorplan are satisfied. Therefore, the cumulative errors of both the distance estimations and direction estimations can be corrected when a map-based position correction is implemented.

6.3 Experimental Evaluation

To evaluate the performance of WiBall, various experiments are conducted in different indoor environments using the prototype as shown in Fig. 6.2(a). In this section, we first evaluate the performance of the TR-based distance estimator.

Then, the performance of WiBall in tracking a moving object in two different environments is studied. At last, the impact of packet loss and system window length on the proposed system is also discussed.

6.3.1 Evaluations of TR Distance Estimator

The first experiment is to estimate the moving distance of a toy train running on a track. We put one RX on a toy train as shown in Fig. 6.10(a) and place one TX about 20m from the RX with two walls between them. The sampling period between adjacent channel measurement is set to $T = 5\,\text{ms}$. CIRs are collected continuously when the toy train is running on the track. We also set an anchor point as shown in Fig. 6.10(a) on the train track and collect the CIR when the train is at the anchor. The TRRS values between all the measured CIRs and the CIR of the anchor are computed and shown in Fig. 6.10(b). The peaks in the red line indicate that the train passes the anchor three times. The estimated length of the track for this single loop is 8.12m and the error is 1.50%, given the actual length of the train track is 8.00m. The train slows down when it makes turns due to the increased friction and then speeds up in the straight line. This trend is reflected in the speed estimation shown by the blue curve. To show the consistency of the distance estimator over time, we collect the CIRs for 100 laps in total and estimate the track length for each lap separately. The histogram of the estimation results is shown in Fig. 6.11. The mean of the estimation error is about 0.02m and the standard error deviation is about 0.13m, which shows that the estimation is

consistent even over a long period.

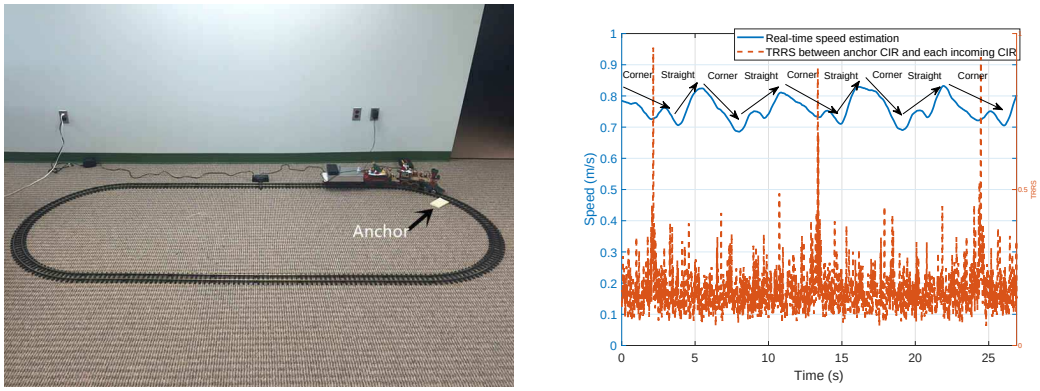

(a) The toy train and the train track used in the experiment.

(b) The estimated speed of the toy train over time.

Figure 6.10: Tracking the speed of the toy train.

The second experiment is to estimate the human walking distance. One RX is put on a cart and one participant pushes the cart along the line from point A to point B shown in Fig. 6.2(a) with an approximately constant speed of 1m/s. To control the walking speed, the participant uses a timer and landmarks placed on the floor during the experiment. In the upper panel of Fig. 6.12(a), for each time t, the TRRS values between the CIR measured at time t and those measured at time $t - \Delta t$, where $\Delta t \in (0s, 0.16s]$, are plotted along the vertical axis. As we can see from the figure, when the person moves slowly (e.g., at the beginning or the end of the experiment), the time differences between the local peaks of the measured TRRS distribution along the vertical axis are greater than that when the person moves faster. In addition, for $t \in [0.5s, 3.5s]$, the asymmetric part of the density function $P(\theta)$ of the energy of MPCs is more significant compared to the case when $t \in [3s, 9.5s]$ and thus the pattern of $J^2(kd)$ is less obvious than

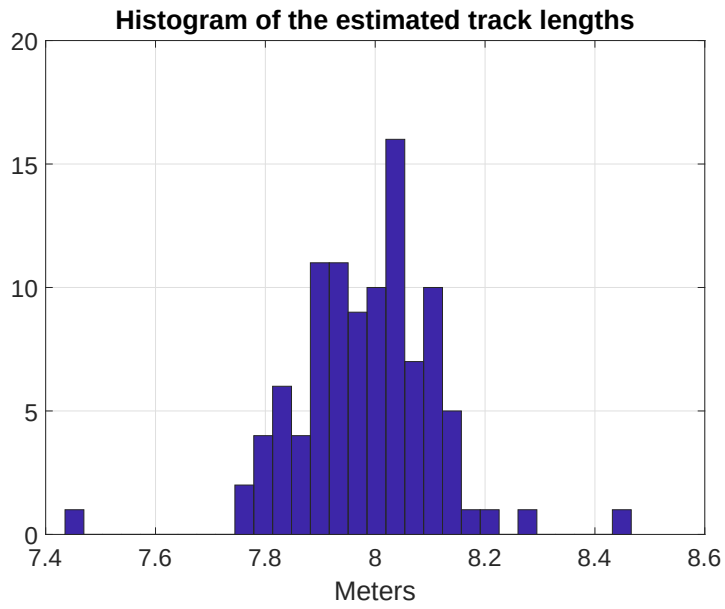

Figure 6.11: The histogram of the estimated track lengths for a total of 100 experiments.

the latter one. The bottom panel of Fig. 6.12(a) shows the corresponding walking speed estimation. The actual distance is 8m and the estimated walking distance is 7.65m, so the corresponding error is 4.4%. The loss of performance is from the blockage of signals by the human body, which reduces the number of significant MPCs.

We further let the participant carry the RX and walk for a distance of 2m, 4m, 6m, 8m, 10m and 12m, respectively. The ground-truth travel distances are measured by a laser distance meter. For each ground-truth distance, the experiment is repeated 20 times with different paths and the walking speed does not need to be constant. The results are shown in Fig. 6.12(b), where the 5, 25, 75, and 95-th percentiles of the estimated distances for each actual distance are plot-

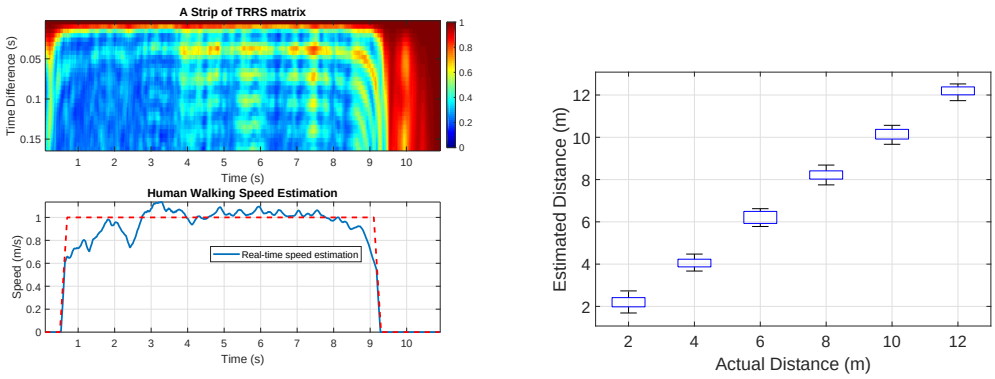

(a) Speed estimation for a controlled human walking speed (1m/s).

(b) The results for walking distance estimation.

Figure 6.12: Human walking speed/distance estimation.

ted from the bottom line to the top line for each block. We find that when the ground-truth distance is small, the error tends to be large. This is mainly because the participant could introduce additional sources of errors which are uncontrollable, such as not following the path strictly, shaking during walking, and not stopping at the exact point in the end. When the distance is short, the impact of this kind of error can be magnified greatly. However, when the walking distance is large, the impact of the uncontrollable errors on the estimation result is insignificant.

6.3.2 Estimated Traces in Different Environment

We evaluate the performance of indoor tracking using WiBall in two sets of experiments. In the first set of experiments, a participant walks inside a building with a large open space. He carriers the RX with him and walks from Point A on the second floor to point B on the first floor, as shown in Fig. 6.13(a). The TX

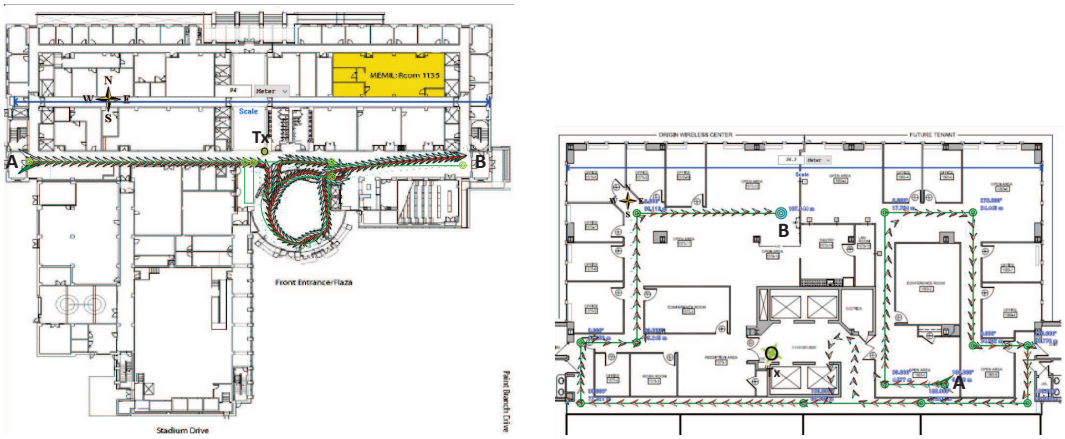

(a) Estimated path in a building with a lot of open space.

(b) Estimated path in an office environment.

Figure 6.13: Experiment results in different environments.

is placed closed to the middle of the path on the second floor. The dimension of the building is around $94\,m \times 73\,m$. Although the moving distance of the first segment of the path is overestimated, the estimated path is corrected when the participant enters the staircase leading to the first floor.

In the second set of experiments, the participant walks inside an office environment. Fig. 6.13(b) demonstrates a typical example of the estimated traces in a typical office of a multi-storey. One RX is put on a cart and the participant pushes the cart along the route from Point A to Point B, as illustrated in the figure. The dimension of the environment is around $36.3\,m \times 19\,m$ and the placement of the TX is also shown in the figure. As we can see from the figure, the estimated path matches the ground truth path very well because the cumulative errors have been corrected by the constraints from the floorplan.

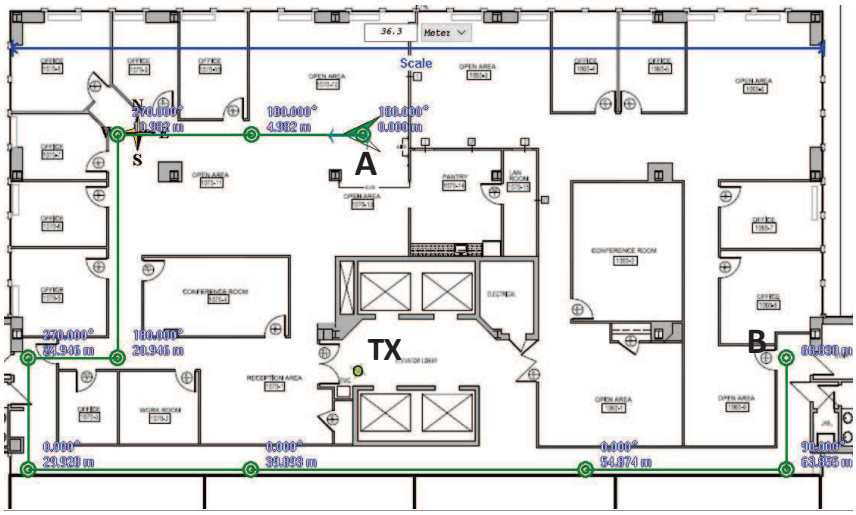

Figure 6.14: The route for the evaluation of statistical errors.

6.3.3 Statistical Analysis of Localization Error

To evaluate the distribution of the localization errors, extensive experiments have been conducted in the same office environment shown in Fig. 6.13(b). The participant pushes the cart with the RX on the cart, following the route as shown in Fig. 6.14.

The RX starts from Point A and stops at different locations in the route shown in Fig. 6.14. The lengths of the chosen paths are 5, 21, 25, 30, 40, 64, and 69m, respectively, and the end of each path is marked with two green circles. For each specific path, the experiment is repeated for 25 times. The estimation error for different paths has been analyzed through empirical cumulative distribution function (CDF), as shown in Fig. 6.15. Based on the results, the median of the estimation error for the selected paths is around 0.33m, and the 80 percentile of the estimation error is within 1m. Therefore, WiBall is able to achieve a sub-

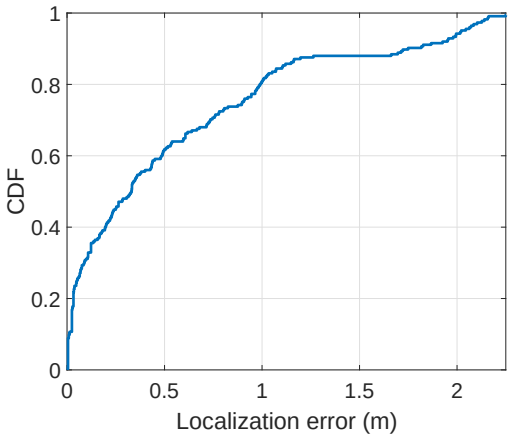

Figure 6.15: Empirical CDF of localization error.

meter median error in this complex indoor environment.

6.3.4 Impact of Packet Loss on Distance Estimation

In the previous experiments, WiBall operates on a vacant band and the packet loss rate can thus be neglected. However, in practice, the RF interference from other RF devices operated on the same frequency band will increase the packet loss rate. Since WiBall relies on the first peak of the TRRS distribution for distance estimation, enough samples need to be collected so as to estimate the first peak accurately, and a high packet loss can affect the peak estimation and thus increase distance estimation error.

To study the impact of RF interference, a pair of RF devices is configured to operate in the same frequency band of WiBall to act as an interference source, and we run the tracking system for 100 times with the ground-truth distance being 10m. When the interfering devices are placed closer to the transmission

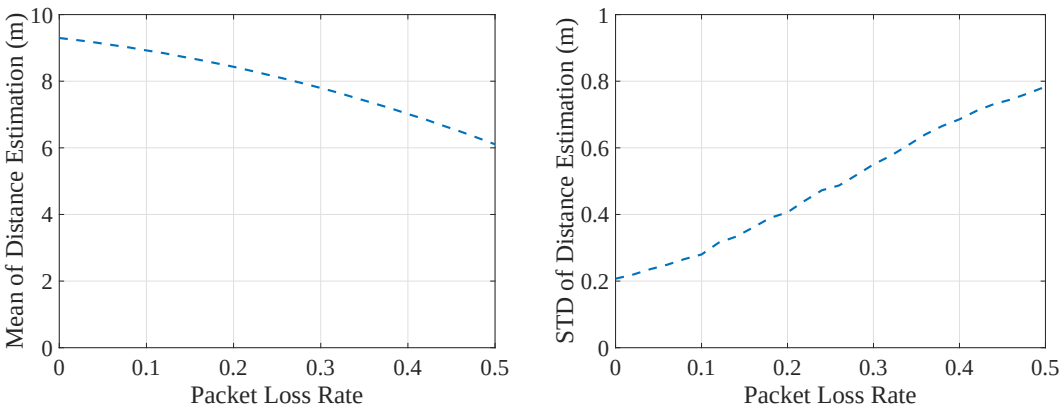

(a) Sample mean of the distance estimation. (b) Standard deviation of the distance estimation.

Figure 6.16: The impact of packet loss on the accuracy of distance estimation.

pair of WiBall, WiBall encounters a higher packet loss rate. Therefore, to obtain various packet loss rates, the interfering devices are placed at different locations during the experiment. The average estimated distance and standard deviation of the estimation under different packet loss rates are shown in Fig. 6.16. It is seen that a large packet loss rate would lead to an underestimation of the moving distance and increase the deviations of the estimates.

6.3.5 Impact of Window Length on Distance Estimation

In the following, the impact of window length on the performance of the proposed TR-based distance estimator is studied. One implicit assumption of the proposed estimator is that the speed of the moving device is constant within the observation window of channel measurements. The length of the observation window should be at least $0.61\lambda/v$, where v is the actual speed of the device. Furthermore, more samples of channel measurements will also improve the accuracy

of $\hat{t}$ as described in Section 6.1.4. Therefore, the window length is an important system parameter of WiBall.

In the following experiments, one RX is put on a toy train whose speed can be tuned and remains constant during each experiment. One TX is placed in two different locations: a LOS location where the RX is within the fields of vision of the TX, and a NLOS location where the direct path between the RX and TX is blocked by walls. The TX keeps transmitting packets with a uniform interval of 5 ms. Two experiments are conducted for each location of the TX with two different speeds of the toy train, 0.72 m/s and 0.63 m/s, respectively, and each experiment lasts 10 minutes. The 5 and 95-th percentiles and the sample mean of the estimated speed have been shown in Fig. 6.17 with different window lengths. It can be observed that when the window length is smaller than 30 samples, the speed estimates have a bias for the both cases; when the window length is greater or equal to 30 samples, the bias is close to 0 and the range of the estimates becomes stable. In addition, a higher accuracy can be achieved when the TX is placed in the NLOS location.

6.4 Summary

In this work, we propose WiBall, which offers an accurate, low-cost, calibration-free and robust solution for INIP in indoor environments without requiring any infrastructure. WiBall leverages the physical properties of the TR focusing ball in radio signals, such as WiFi, LTE, 5G, etc., to estimate the moving distance of an

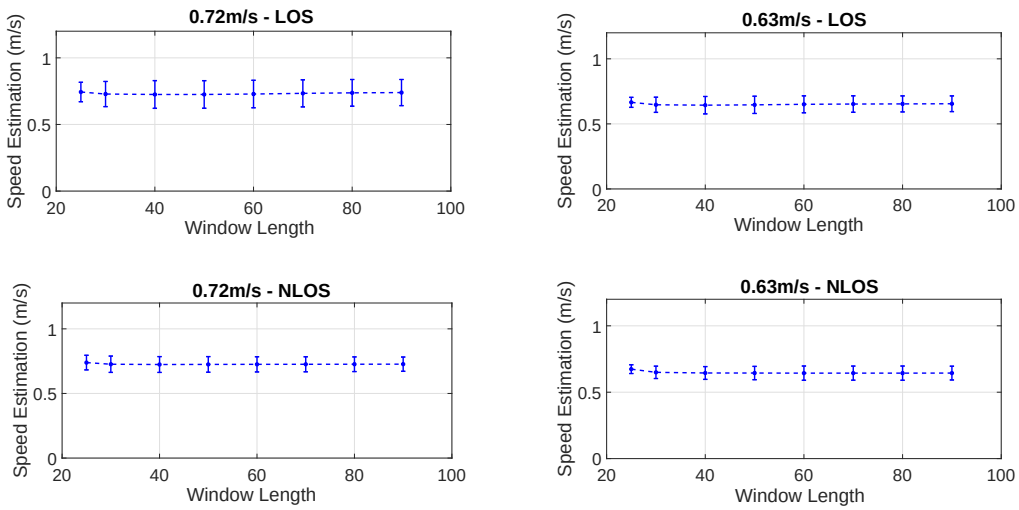

Figure 6.17: Impact of window length in terms of speed estimations.

object being monitored and does not need any specialized hardware. It is shown through extensive experiments that WiBall can achieve a decimeter-level accuracy. WiBall is also easily scalable and can accommodate a large number of users with only a single access point or TX. Therefore, WiBall can be a very promising candidate for future indoor tracking systems.

Chapter 7: Conclusion

7.1 Summary

In this dissertation, we first present the primer of wireless sensing, including the channel models for radio propagations and the techniques to harvest the information embedded in hundreds of multipaths indoors.

Then, we have presented four CSI-based indoor wireless sensing systems:

1. *passive indoor speed estimation*: in Chapter 3, we propose WiSpeed, a universal indoor speed estimation system for human motion leveraging commercial WiFi, which can estimate the speed of a moving object under either device-free or device-based condition. WiSpeed is built upon the statistical theory of EM waves which quantifies the impact of human motion on EM waves for indoor environments. We conduct extensive experiments in a typical indoor environment which demonstrates that WiSpeed can achieve a MAPE of 4.85% for device-free human walking speed monitoring and a MAPE of 4.62% for device-based speed estimation. Meanwhile, it achieves an average detection rate of 95% with no false alarms for human fall detection. Due to its large coverage, robustness, low cost, and low computational

complexity, WiSpeed is a very promising candidate for indoor passive human activity monitoring systems.

2. *motion detection*: in Chapter 4, we present the model, design, and implementation of WiDetect, the first practical whole-home motion detection system that achieves almost zero false alarms using only a single WiFi link. A statistical model that comprehensively leverages all existing multipath components for motion detection is proposed and the relationship between the detection rate and false alarm rate for motion detection is also derived. Extensive experiments show its superiority over existing motion detection approaches. With extremely high sensitivity and fairly low false alarms, we believe that the proposed WiDetect can be a promising practical technology for ubiquitous device-free motion detection, allowing for a range of critical applications for smart life.

3. *sleep monitoring*: in Chapter 5, we present the design, implementation, and evaluation of SMARS, the first practical sleep monitoring system that exploits ambient radio signals to recognize sleep stages, without instrumenting users' body or the bed. SMARS achieves this goal by monitoring breathing and body movements during sleep accurately and instantaneously, to a level of performance previously only attainable with expensive specialized infrastructure. A key enabler behind is a statistical model that considers all reflection and scattering multipaths indoors without making unrealistic assumptions. We implement SMARS on commercial WiFi chipsets and

validate its performance by extensive experiments with the 32 nights data collected in 6 homes. We believe SMARS takes a promising step towards practical in-home sleep monitoring.

4. *indoor tracking*: in Chapter 6, we propose WiBall, which offers an accurate, low-cost, calibration-free and robust solution for indoor positioning and indoor navigation without requiring any infrastructure. WiBall leverages the physical properties of the TR focusing ball in radio signals, such as WiFi, LTE, 5G, etc., to estimate the moving distance of an object being monitored and does not need any specialized hardware. It is shown through extensive experiments that WiBall can achieve a decimeter-level accuracy. WiBall is also easily scalable and can accommodate a large number of users with only a single access point or TX. Therefore, WiBall can be a very promising candidate for future indoor tracking systems.

Many important applications can be developed based on the proposed four systems. In particular, the passive speed estimation system further enables IoT applications such as fall detection, gait monitoring, and fitness tracking; the motion detection system enables intrusion detection, human behavior analysis, and smart home; the sleep monitoring system can be further developed into a continuous time wellbeing monitoring system by incorporating motion detection and fall detection; the indoor tracking system can facilitate applications in manufacturing asset tracking, intelligent transportation, and so on.

7.2 Future Work

There are several open problems and challenges to be explored and investigated before the successful deployment of the proposed indoor wireless sensing systems. The exploration of these issues could make the proposed IoT applications more versatile and useful in real life scenarios.

Firstly, the complexity of the proposed algorithms should be optimized. In particular, the computational complexity of the proposed passive speed estimator, WiSpeed, in Chapter 3 is quite large, which cannot be accommodated in low-cost embedded systems. Instead, cloud computing is needed for the computation. However, the bandwidth consumption of the system is larger than the average capacity of an ordinary residential.

Secondly, in this dissertation, we only consider the scenario where only a single pair of Tx and Rx is available. However, in the future, multiple pairs may be deployed in the environment, which will enable the feasibility of passive motion localization in addition to detection. With the location information of the motion, the performance of fall detection can also be improved, e.g., in some locations, such as bathroom and stairs, the likelihood of falls is higher and the damage can be even more serious.

Lastly, as the WiFi technology is evolving, more bandwidth and more antennas are available compared with the current standard. At the same time, the frontier of wireless sensing using ambient radio signals can be further explored. It can be expected that even the minute movement, such as the movement of fin-

gers and eyeballs, can be detected or tracked, which will enable more interesting IoT applications in the future.

Bibliography

[1] The aasm manual for the scoring of sleep and associated events. https://www.philips.com.hk/healthcare/product/HC1043941/alice-pdx-portable-sleep-diagnostic-system. Accessed: 2018-09-18.

[2] Alice pdx: portable sleep diagnostic system. https://www.philips.com.hk/healthcare/product/HC1043941/alice-pdx-portable-sleep-diagnostic-system, note = Accessed: 2018-09-18.

[3] Global Indoor Positioning and Indoor Navigation (IPIN) Market 2017-2021. https://tinyurl.com/ya35sh2z [Accessed: 07-Dec-2017], 2017. [Online].

[4] Emfit sleep tracking & monitoring with heart-rate-variability. https://www.emfit.com/, 2018.

[5] H. Abdelnasser, M. Youssef, and K. A. Harras. WiGest: A ubiquitous WiFi-based gesture recognition system. In *Proc. of IEEE INFOCOM*, pages 1472–1480, April 2015.

[6] Heba Abdelnasser, Khaled A Harras, and Moustafa Youssef. Ubibreathe: A ubiquitous non-invasive wifi-based breathing estimator. In *Proceedings of the 16th ACM International Symposium on Mobile Ad Hoc Networking and Computing*, pages 277–286. ACM, 2015.

[7] Fadel Adib, Zach Kabelac, Dina Katabi, and Robert C. Miller. 3D tracking via body radio reflections. In *11th USENIX Symposium on Networked Systems Design and Implementation*, pages 317–329. USENIX Association, 2014.

[8] Fadel Adib, Zachary Kabelac, Dina Katabi, and Robert C Miller. 3d tracking via body radio reflections. In *NSDI*, volume 14, pages 317–329, 2014.

[9] Fadel Adib and Dina Katabi. See through walls with WiFi! *SIGCOMM Comput. Commun. Rev.*, 43(4):75–86, August 2013.

[10] Fadel Adib, Hongzi Mao, Zachary Kabelac, Dina Katabi, and Robert C. Miller. Smart homes that monitor breathing and heart rate. In *Proceedings of the 33rd Annual ACM Conference on Human Factors in Computing Systems (CHI)*, 2015.

[11] Kamran Ali, Alex X. Liu, Wei Wang, and Muhammad Shahzad. Keystroke recognition using WiFi signals. In *Proc. of the 21st Annual International Conference on Mobile Computing & Networking*, pages 90–102. ACM, 2015.

[12] Kamran Ali, Alex X Liu, Wei Wang, and Muhammad Shahzad. Keystroke recognition using wifi signals. In *Proceedings of the 21st Annual International Conference on Mobile Computing and Networking (MobiCom)*, 2015.

[13] Bruce M Altevogt, Harvey R Colten, et al. *Sleep disorders and sleep deprivation: an unmet public health problem*. National Academies Press, 2006.

[14] Fabio Bagalà, Clemens Becker, Angelo Cappello, Lorenzo Chiari, Kamiar Aminian, Jeffrey M Hausdorff, Wiebren Zijlstra, and Jochen Klenk. Evaluation of accelerometer-based fall detection algorithms on real-world falls. *PloS one*, 7(5):e37062, 2012.

[15] Paramvir Bahl and Venkata N Padmanabhan. Radar: An in-building rf-based user location and tracking system. In *INFOCOM 2000. Nineteenth Annual Joint Conference of the IEEE Computer and Communications Societies. Proceedings. IEEE*, volume 2, pages 775–784. Ieee, 2000.

[16] John R Barry, Edward A Lee, and David G Messerschmitt. *Digital communication*. Springer Science & Business Media, 2012.

[17] David K Barton. *Radar system analysis and modeling*, volume 1. Artech House, 2004.

[18] Eric Blossom. Gnu radio: tools for exploring the radio frequency spectrum. *Linux journal*, 2004(122):4, 2004.

[19] George EP Box, Gwilym M Jenkins, Gregory C Reinsel, and Greta M Ljung. *Time series analysis: forecasting and control*. John Wiley & Sons, 2015.

[20] Christopher JC Burges. A tutorial on support vector machines for pattern recognition. *Data mining and knowledge discovery*, 2(2):121–167, 1998.

[21] Paul Castro, Patrick Chiu, Ted Kremenek, and Richard Muntz. A probabilistic room location service for wireless networked environments. In *Ubicomp 2001: Ubiquitous Computing*, pages 18–34. Springer, 2001.

[22] Centers for Disease Control and Prevention. Short sleep duration among us adults. https://www.cdc.gov/sleep/data_statistics.html, 2018.

[23] C. Chen, Y. Chen, Y. Han, H. Q. Lai, F. Zhang, and K. J. R. Liu. Achieving centimeter-accuracy indoor localization on WiFi platforms: A multi-antenna approach. *IEEE Internet of Things Journal*, 4(1):122–134, Feb 2017.

[24] C. Chen, Y. Han, Y. Chen, H. Q. Lai, F. Zhang, B. Wang, and K. J. R. Liu. TR-BREATH: Time-reversal breathing rate estimation and detection. *IEEE Transactions on Biomedical Engineering*, PP(99):1–14, 2017.

[25] Chen Chen, Yan Chen, Yi Han, Hung-Quoc Lai, and K. J. Ray Liu. Achieving centimeter-accuracy indoor localization on wifi platforms: A frequency hopping approach. *IEEE Internet of Things Journal*, 4(1):111–121, 2017.

[26] Yan Chen, Feng Han, Yu-Han Yang, Hang Ma, Yi Han, Chunxiao Jiang, Hung-Quoc Lai, David Claffey, Zoltan Safar, and KJ Ray Liu. Time-reversal wireless paradigm for green internet of things: An overview. *IEEE Internet of Things Journal*, 1(1):81–98, 2014.

[27] Zhenyu Chen, Mu Lin, Fanglin Chen, Nicholas D Lane, Giuseppe Cardone, Rui Wang, Tianxing Li, Yiqiang Chen, Tanzeem Choudhury, and Andrew T Campbell. Unobtrusive sleep monitoring using smartphones. In *Proceedings of the 7th International Conference on Pervasive Computing Technologies for Healthcare*, 2013.

[28] Tzi-Dar Chiueh, Pei-Yun Tsai, and I-Wei Lai. *Baseband receiver design for wireless MIMO-OFDM communications*. John Wiley & Sons, 2012.

[29] William S Cleveland. Robust locally weighted regression and smoothing scatterplots. *Journal of the American statistical association*, 74(368):829–836, 1979.

[30] Richard J Doviak et al. *Doppler radar and weather observations*. Courier Corporation, 2006.

[31] Hassan El-Sallabi, Persefoni Kyritsi, Arogyaswami Paulraj, and George Papanicolaou. Experimental investigation on time reversal precoding for space–time focusing in wireless communications. *IEEE Transactions on Instrumentation and Measurement*, 59(6):1537–1543, 2010.

[32] W. M. Gifford, W. W. L. Li, Y. J. Zhang, and M. Z. Win. Effect of bandwidth on the number of multipath components in realistic wireless indoor channels. In *Proceedings of the IEEE International Conference on Communications (ICC)*, June 2011.

[33] Domenico Giustiniano and Stefan Mangold. Caesar: carrier sense-based ranging in off-the-shelf 802.11 wireless lan. In *Proceedings of the Seventh*

COnference on emerging Networking EXperiments and Technologies, page 10. ACM, 2011.

[34] Jon Gjengset, Jie Xiong, Graeme McPhillips, and Kyle Jamieson. Phaser: Enabling phased array signal processing on commodity wifi access points. In *Proceedings of the 20th annual international conference on Mobile computing and networking*, pages 153–164. ACM, 2014.

[35] Stuart A Golden and Steve S Bateman. Sensor measurements for wi-fi location with emphasis on time-of-arrival ranging. *IEEE Transactions on Mobile Computing*, 6(10), 2007.

[36] Ernesto Martín Gorostiza, José Luis Lázaro Galilea, Franciso Javier Meca Meca, David Salido Monzú, Felipe Espinosa Zapata, and Luis Pallarés Puerto. Infrared sensor system for mobile-robot positioning in intelligent spaces. *Sensors*, 11(5):5416–5438, 2011.

[37] S. Z. Gurbuz, C. Clemente, A. Balleri, and J. J. Soraghan. Micro-Doppler-based in-home aided and unaided walking recognition with multiple radar and sonar systems. *IET Radar, Sonar Navigation*, 11(1):107–115, 2017.

[38] Daniel Halperin, Wenjun Hu, Anmol Sheth, and David Wetherall. Tool release: Gathering 802.11n traces with channel state information. *SIGCOMM Comput. Commun. Rev.*, 41(1):53–53, January 2011.

[39] Tian Hao, Guoliang Xing, and Gang Zhou. isleep: unobtrusive sleep quality monitoring using smartphones. In *Proceedings of the 11th ACM Conference on Embedded Networked Sensor Systems (SenSys)*, 2013.

[40] David A Hill. *Electromagnetic fields in cavities: deterministic and statistical theories*, volume 35. John Wiley & Sons, 2009.

[41] Peter Hillyard. Rf_respiration_monitoring_dataverse. https://doi.org/10.7910/DVN/X7AYXQ, 2018.

[42] Peter Hillyard, Anh Luong, Alemayehu Solomon Abrar, Neal Patwari, Krishna Sundar, Robert Farney, Jason Burch, Christina A. Porucznik, and Sarah Pollard. Experience: Cross-technology radio respiratory monitoring performance study. In *Proceedings of the 24th Annual International Conference on Mobile Computing and Networking (MobiCom)*, Oct 2018.

[43] Chen-Yu Hsu, Aayush Ahuja, Shichao Yue, Rumen Hristov, Zachary Kabelac, and Dina Katabi. Zero-effort in-home sleep and insomnia monitoring using radio signals. *Proceedings of the ACM on Interactive, Mobile, Wearable and Ubiquitous Technologies (UbiComp)*, 1(3):59:1–59:18, September 2017.

[44] Chen-Yu Hsu, Yuchen Liu, Zachary Kabelac, Rumen Hristov, Dina Katabi, and Christine Liu. Extracting gait velocity and stride length from surrounding radio signals. In *Proc. of CHI Conference on Human Factors in Computing Systems*, pages 2116–2126. ACM, 2017.

[45] Wenjun Jiang, Chenglin Miao, Fenglong Ma, Shuochao Yao, Yaqing Wang, Ye Yuan, Hongfei Xue, Chen Song, Xin Ma, Dimitrios Koutsonikolas, et al. Towards environment independent device free human activity recognition. 2018.

[46] Yuanwei Jin, José MF Moura, Yi Jiang, Daniel D Stancil, and Ahmet G Cepni. Time reversal detection in clutter: Additional experimental results. *IEEE Transactions on Aerospace and Electronic Systems*, 47(1):140–154, 2011.

[47] Ossi Johannes Kaltiokallio, Hüseyin Yigitler, Riku Jäntti, and Neal Patwari. Non-invasive respiration rate monitoring using a single cots tx-rx pair. In *Proceedings of the 13th international symposium on information processing in sensor networks (IPSN)*, 2014.

[48] M. Khan, B. N. Silva, and K. Han. Internet of things based energy aware smart home control system. *IEEE Access*, 4:7556–7566, 2016.

[49] Seung-Jean Kim, Kwangmoo Koh, Stephen Boyd, and Dimitry Gorinevsky. l1 trend filtering. *SIAM review*, 51(2):339–360, 2009.

[50] Juha M Kortelainen, Martin O Mendez, Anna Maria Bianchi, Matteo Matteucci, and Sergio Cerutti. Sleep staging based on signals acquired through bed sensor. *IEEE Transactions on Information Technology in Biomedicine*, 14(3):776–785, 2010.

[51] Ahmed E Kosba, Ahmed Saeed, and Moustafa Youssef. Rasid: A robust wlan device-free passive motion detection system. In *Proc. of IEEE International Conferentce on Pervasive computing and communications*, pages 180–189. IEEE, 2012.

[52] Manikanta Kotaru, Kiran Joshi, Dinesh Bharadia, and Sachin Katti. Spotfi: Decimeter level localization using wifi. In *ACM SIGCOMM Computer Communication Review*, volume 45, pages 269–282. ACM, 2015.

[53] Y Kozlov and T Weinkauf. Persistence1D: Extracting and filtering minima and maxima of 1d functions. *http://people.mpi-inf.mpg.de/weinkauf/notes/persistence1d.html*, pages 11–01, 2015.

[54] Michael Kuhn, Cemin Zhang, Brandon Merkl, Depeng Yang, Yazhou Wang, Mohamed Mahfouz, and Aly Fathy. High accuracy uwb localization in dense indoor environments. In *Ultra-Wideband, 2008. ICUWB 2008. IEEE International Conference on*, volume 2, pages 129–132. IEEE, 2008.

[55] Oscar D Lara, Miguel A Labrador, et al. A survey on human activity recognition using wearable sensors. *IEEE Communications Surveys and Tutorials*, 15(3):1192–1209, 2013.

[56] Joon-Yong Lee and Robert A Scholtz. Ranging in a dense multipath environment using an uwb radio link. *IEEE Journal on Selected Areas in Communications*, 20(9):1677–1683, 2002.

[57] Itamar Lerner, Shira M Lupkin, Neha Sinha, Alan Tsai, and Mark A Gluck. Baseline levels of rapid eye movement sleep may protect against excessive activity in fear-related neural circuitry. *Journal of Neuroscience*, 37(46):11233–11244, 2017.

[58] Geoffroy Lerosey, J De Rosny, A Tourin, A Derode, G Montaldo, and M Fink. Time reversal of electromagnetic waves. *Physical review letters*, 92(19):193904, 2004.

[59] F. Lin, Y. Zhuang, C. Song, A. Wang, Y. Li, C. Gu, C. Li, and W. Xu. Sleepsense: A non-contact and cost-effective sleep monitoring system. *IEEE Transactions on Biomedical Circuits and Systems*, 11(1):189–202, Feb 2017.

[60] Jian Liu, Yan Wang, Yingying Chen, Jie Yang, Xu Chen, and Jerry Cheng. Tracking vital signs during sleep leveraging off-the-shelf wifi. In *Proceedings of the 16th ACM International Symposium on Mobile Ad Hoc Networking and Computing*, pages 267–276. ACM, 2015.

[61] X. Liu, J. Cao, S. Tang, and J. Wen. Wi-sleep: Contactless sleep monitoring via wifi signals. In *Proceedings of the IEEE Real-Time Systems Symposium (RTSS)*, Dec 2014.

[62] Jiguang Lv, Wu Yang, Liangyi Gong, Dapeng Man, and Xiaojiang Du. Robust wlan-based indoor fine-grained intrusion detection. In *Proc. of IEEE Global Communications Conference (GLOBECOM)*, pages 1–6. IEEE, 2016.

[63] Rainer Mautz and Sebastian Tilch. Survey of optical indoor positioning systems. In *Indoor Positioning and Indoor Navigation (IPIN), 2011 International Conference on*, pages 1–7. IEEE, 2011.

[64] Jun-Ki Min, Afsaneh Doryab, Jason Wiese, Shahriyar Amini, John Zimmerman, and Jason I Hong. Toss'n'turn: smartphone as sleep and sleep quality detector. In *Proceedings of the SIGCHI conference on human factors in computing systems (CHI)*, 2014.

[65] Jos MF Moura and Yuanwei Jin. Detection by time reversal: Single antenna. *IEEE transactions on signal processing*, 55(1):187–201, 2007.

[66] Subhas Chandra Mukhopadhyay. Wearable sensors for human activity monitoring: A review. *IEEE sensors journal*, 15(3):1321–1330, 2015.

[67] Patrick Murphy, Ashu Sabharwal, and Behnaam Aazhang. Design of warp: A flexible wireless open-access research platform. In *Proc. EUSIPCO*, pages 53–54, 2006.

[68] Ravi Narasimhan and Donald C Cox. Speed estimation in wireless systems using wavelets. *IEEE Transactions on Communications*, 47(9):1357–1364, 1999.

[69] Anh Nguyen, Raghda Alqurashi, Zohreh Raghebi, Farnoush Banaei-Kashani, Ann C Halbower, and Tam Vu. A lightweight and inexpensive in-ear sensing system for automatic whole-night sleep stage monitoring. In *Proceedings of the 14th ACM Conference on Embedded Network Sensor Systems (SenSys)*, 2016.

[70] Phuc Nguyen, Xinyu Zhang, Ann Halbower, and Tam Vu. Continuous and fine-grained breathing volume monitoring from afar using wireless signals. In *Proceedings of the 35th Annual IEEE International Conference on Computer Communications (INFOCOM)*, 2016.

[71] National Institute of Health. Brain basics: Understanding sleep. `http://www.ninds.nih.gov/disorders/brain_basics/understanding_sleep.htm#sleep_disorders`, 2018.

[72] A. Papoulis and U. Pillai. *Probability, random variables, and stochastic processes*. McGraw-Hill, 2002.

[73] Goohyun Park, Daesik Hong, and Changeon Kang. Level crossing rate estimation with doppler adaptive noise suppression technique in frequency domain. In *Vehicular Technology Conference, 2003. VTC 2003-Fall. 2003 IEEE 58th*, volume 2, pages 1192–1195. IEEE, 2003.

[74] Neal Patwari, Lara Brewer, Quinn Tate, Ossi Kaltiokallio, and Maurizio Bocca. Breathfinding: A wireless network that monitors and locates breathing in a home. *IEEE Journal of Selected Topics in Signal Processing*, 8(1):30–42, 2014.

[75] Thomas Penzel, Niels Wessel, Maik Riedl, Jan W Kantelhardt, Sven Rostig, Martin Glos, Alexander Suhrbier, Hagen Malberg, and Ingo Fietze. Cardiovascular and respiratory dynamics during normal and pathological sleep. *Chaos: An Interdisciplinary Journal of Nonlinear Science*, 17(1):015116, 2007.

[76] S. Pinto, J. Cabral, and T. Gomes. We-care: An IoT-based health care system for elderly people. In *IEEE International Conference on Industrial Technology (ICIT)*, pages 1378–1383, March 2017.

[77] Qifan Pu, Sidhant Gupta, Shyamnath Gollakota, and Shwetak Patel. Whole-home gesture recognition using wireless signals. In *Proc. of the 19th Annual International Conference on Mobile Computing & Networking*, pages 27–38. ACM, 2013.

[78] Kun Qian, Chenshu Wu, Zheng Yang, Yunhao Liu, and Kyle Jamieson. Widar: Decimeter-level passive tracking via velocity monitoring with commodity wi-fi. In *Proc. of the 18th ACM International Symposium on Mobile Ad Hoc Networking and Computing*, page 6. ACM, 2017.

[79] Kun Qian, Chenshu Wu, Zheng Yang, Yunhao Liu, and Kyle Jamieson. Widar: Decimeter-level passive tracking via velocity monitoring with commodity wi-fi. In *Proceedings of the 18th ACM International Symposium on Mobile Ad Hoc Networking and Computing*, page 6. ACM, 2017.

[80] Kun Qian, Chenshu Wu, Yi Zhang, Guidong Zhang, Zheng Yang, and Yunhao Liu. Widar2. 0: Passive human tracking with a single wi-fi link. *Procs. of ACM MobiSys*, 2018.

[81] Kun Qian, Chenshu Wu, Zimu Zhou, Yue Zheng, Zheng Yang, and Yunhao Liu. Inferring motion direction using commodity wi-fi for interactive exergames. In *Proc. of CHI Conference on Human Factors in Computing Systems*, pages 1961–1972. ACM, 2017.

[82] Tauhidur Rahman, Alexander T. Adams, Ruth Vinisha Ravichandran, Mi Zhang, Shwetak N. Patel, Julie A. Kientz, and Tanzeem Choudhury. Dopplesleep: A contactless unobtrusive sleep sensing system using short-range doppler radar. In *Proceedings of the 2015 ACM International Joint Conference on Pervasive and Ubiquitous Computing (UbiComp)*, New York, NY, USA, 2015.

[83] Ish Rishabh, Don Kimber, and John Adcock. Indoor localization using controlled ambient sounds. In *Indoor Positioning and Indoor Navigation (IPIN), 2012 International Conference on*, pages 1–10. IEEE, 2012.

[84] Philippe Roux, Benoit Roman, and Mathias Fink. Time-reversal in an ultrasonic waveguide. *Applied Physics Letters*, 70(14):1811–1813, 1997.

[85] Ashwin Sampath and Jack M Holtzman. Estimation of maximum doppler frequency for handoff decisions. In *Vehicular Technology Conference, 1993., 43rd IEEE*, pages 859–862. IEEE, 1993.

[86] Sara E Schaefer, Cynthia Carter Ching, Heather Breen, and J Bruce German. Wearing, thinking, and moving: testing the feasibility of fitness tracking with urban youth. *American Journal of Health Education*, 47(1):8–16, 2016.

[87] Henry Scheffe. *The analysis of variance*, volume 72. John Wiley & Sons, 1999.

[88] M. Seifeldin, A. Saeed, A. E. Kosba, A. El-Keyi, and M. Youssef. Nuzzer: A large-scale device-free passive localization system for wireless environments. *IEEE Transactions on Mobile Computing*, 12(7):1321–1334, July 2013.

[89] Souvik Sen, Dongho Kim, Stephane Laroche, Kyu-Han Kim, and Jeongkeun Lee. Bringing cupid indoor positioning system to practice. In *Proceedings of the 24th International Conference on World Wide Web*, pages 938–948. International World Wide Web Conferences Steering Committee, 2015.

[90] Souvik Sen, Jeongkeun Lee, Kyu-Han Kim, and Paul Congdon. Avoiding multipath to revive inbuilding wifi localization. In *Proceeding of the 11th annual international conference on Mobile systems, applications, and services*, pages 249–262. ACM, 2013.

[91] Souvik Sen, Božidar Radunovic, Romit Roy Choudhury, and Tom Minka. You are facing the Mona Lisa: Spot localization using PHY layer information. In *Proc. of the 10th International Conference on Mobile Systems, Applications, and Services*, pages 183–196. ACM, 2012.

[92] Souvik Sen, Bozidar Radunovic, Romit Roy Choudhury, and Tom Minka. Precise indoor localization using phy information. In *Proceedings of the 9th international conference on Mobile systems, applications, and services*, pages 413–414. ACM, 2011.

[93] John S Seybold. *Introduction to RF propagation*. John Wiley & Sons, 2005.

[94] Longfei Shangguan, Zheng Yang, Alex X Liu, Zimu Zhou, and Yunhao Liu. Stpp: Spatial-temporal phase profiling-based method for relative rfid tag localization. *IEEE/ACM Transactions on Networking (ToN)*, 25(1):596–609, 2017.

[95] Robert H Shumway and David S Stoffer. Time series analysis and its applications with r examples. *Time series analysis and its applications with R examples*, 2006.

[96] Li Sun, Souvik Sen, Dimitrios Koutsonikolas, and Kyu-Han Kim. WiDraw: Enabling hands-free drawing in the air on commodity WiFi devices. In *Proc. of the 21st Annual International Conference on Mobile Computing & Networking*, pages 77–89. ACM, 2015.

[97] James D Taylor. *Introduction to ultra-wideband radar systems*. CRC press, 1994.

[98] David Tse and Pramod Viswanath. *Fundamentals of wireless communication*. Cambridge university press, 2005.

[99] David Tse and Pramod Viswanath. *Fundamentals of wireless communication*. Cambridge university press, 2005.

[100] Ph Van Dorp and FCA Groen. Feature-based human motion parameter estimation with radar. *IET Radar, Sonar & Navigation*, 2(2):135–145, 2008.

[101] Richard Van Nee. Delay spread requirements for wireless networks in the 2.4 GHz and 5 GHzi bands. *IEEE*, 802:802–22, 1997.

[102] Beibei Wang, Yongle Wu, Feng Han, Yu-Han Yang, and KJ Ray Liu. Green wireless communications: A time-reversal paradigm. *IEEE Journal on Selected Areas in Communications*, 29(8):1698–1710, 2011.

[103] G. Wang, Y. Zou, Z. Zhou, K. Wu, and L. M. Ni. We can hear you with Wi-Fi! *IEEE Transactions on Mobile Computing*, 15(11):2907–2920, Nov 2016.

[104] Hao Wang, Daqing Zhang, Junyi Ma, Yasha Wang, Yuxiang Wang, Dan Wu, Tao Gu, and Bing Xie. Human respiration detection with commodity wifi devices: Do user location and body orientation matter? In *Proceedings of the ACM International Joint Conference on Pervasive and Ubiquitous Computing (UbiComp)*, 2016.

[105] He Wang, Souvik Sen, Ahmed Elgohary, Moustafa Farid, Moustafa Youssef, and Romit Roy Choudhury. No need to war-drive: Unsupervised indoor localization. In *Proceedings of the 10th international conference on Mobile systems, applications, and services*, pages 197–210. ACM, 2012.

[106] Liang Wang, Guoying Zhao, Li Cheng, and Matti Pietikäinen. *Machine learning for vision-based motion analysis: Theory and techniques*. Springer, 2010.

[107] Wei Wang, Alex X. Liu, Muhammad Shahzad, Kang Ling, and Sanglu Lu. Understanding and modeling of WiFi signal based human activity recognition. In *Proc. of the 21st Annual International Conference on Mobile Computing & Networking*, pages 65–76. ACM, 2015.

[108] Wei Wang, Alex X Liu, Muhammad Shahzad, Kang Ling, and Sanglu Lu. Understanding and modeling of wifi signal based human activity recognition. In *Proceedings of the 21st annual international conference on mobile computing and networking*, pages 65–76. ACM, 2015.

[109] Xiaogang Wang. Intelligent multi-camera video surveillance: A review. *Pattern recognition letters*, 34(1):3–19, 2013.

[110] Xuyu Wang, Lingjun Gao, and Shiwen Mao. Phasefi: Phase fingerprinting for indoor localization with a deep learning approach. In *Global Communications Conference (GLOBECOM), 2015 IEEE*, pages 1–6. IEEE, 2015.

[111] Xuyu Wang, Lingjun Gao, Shiwen Mao, and Santosh Pandey. Deepfi: Deep learning for indoor fingerprinting using channel state information. In *Wireless Communications and Networking Conference (WCNC), 2015 IEEE*, pages 1666–1671. IEEE, 2015.

[112] Xuyu Wang, Chao Yang, and Shiwen Mao. Tensorbeat: Tensor decomposition for monitoring multiperson breathing beats with commodity wifi. *ACM Transactions on Intelligent Systems and Technology*, 9(1):8:1–8:27, September 2017.

[113] Y. Wang, K. Wu, and L. M. Ni. WiFall: Device-free fall detection by wireless networks. *IEEE Transactions on Mobile Computing*, 16(2):581–594, Feb 2017.

[114] Yan Wang, Jian Liu, Yingying Chen, Marco Gruteser, Jie Yang, and Hongbo Liu. E-eyes: Device-free location-oriented activity identification using fine-grained wifi signatures. In *Proc. of the 20th Annual International Conference on Mobile Computing & Networking*, pages 617–628. ACM, 2014.

[115] Martin Werner, Moritz Kessel, and Chadly Marouane. Indoor positioning using smartphone camera. In *Indoor Positioning and Indoor Navigation (IPIN), 2011 International Conference on*, pages 1–6. IEEE, 2011.

[116] C. Wu, Z. Yang, Z. Zhou, X. Liu, Y. Liu, and J. Cao. Non-invasive detection of moving and stationary human with wifi. *IEEE Journal on Selected Areas in Communications*, 33(11):2329–2342, Nov 2015.

[117] Chenshu Wu, Zheng Yang, Zimu Zhou, Xuefeng Liu, Yunhao Liu, and Jiannong Cao. Non-invasive detection of moving and stationary human with wifi. *IEEE Journal on Selected Areas in Communications*, 33(11):2329–2342, 2015.

[118] Kaishun Wu, Jiang Xiao, Youwen Yi, Dihu Chen, Xiaonan Luo, and Lionel M Ni. Csi-based indoor localization. *IEEE Transactions on Parallel and Distributed Systems*, 24(7):1300–1309, 2013.

[119] Zhung-Han Wu, Yi Han, Yan Chen, and KJ Ray Liu. A time-reversal paradigm for indoor positioning system. *IEEE Transactions on Vehicular Technology*, 64(4):1331–1339, 2015.

[120] Chengshan Xiao, Karl D Mann, and Jan C Olivier. Mobile speed estimation for tdma-based hierarchical cellular systems. *IEEE Transactions on Vehicular Technology*, 50(4):981–991, 2001.

[121] Jiang Xiao, Kaishun Wu, Youwen Yi, Lu Wang, and Lionel M Ni. Pilot: Passive device-free indoor localization using channel state information. In *Proc. of IEEE International Conference on Distributed Computing Systems (ICDCS)*, pages 236–245. IEEE, 2013.

[122] Yaxiong Xie, Zhenjiang Li, and Mo Li. Precise power delay profiling with commodity wifi. In *Proceedings of the 21st Annual International Conference on Mobile Computing and Networking*, pages 53–64. ACM, 2015.

[123] Tong Xin, Bin Guo, Zhu Wang, Pei Wang, Jacqueline Chi Kei Lam, Victor Li, and Zhiwen Yu. Freesense: A robust approach for indoor human detection using wi-fi signals. *Proceedings of the ACM on Interactive, Mobile, Wearable and Ubiquitous Technologies*, 2(3):143, 2018.

[124] Jie Xiong and Kyle Jamieson. Arraytrack: a fine-grained indoor location system. Usenix, 2013.

[125] Jie Xiong, Karthikeyan Sundaresan, and Kyle Jamieson. Tonetrack: Leveraging frequency-agile radios for time-based indoor wireless localization. In *Proceedings of the 21st Annual International Conference on Mobile Computing and Networking*, pages 537–549. ACM, 2015.

[126] Q. Xu, Y. Chen, B. Wang, and K. J. R. Liu. TRIEDS: Wireless events detection through the wall. *IEEE Internet of Things Journal*, 4(3):723–735, June 2017.

[127] Qinyi Xu, Yan Chen, and KJ Ray Liu. Combating strong–weak spatial–temporal resonances in time-reversal uplinks. *IEEE Transactions on Wireless Communications*, 15(1):568–580, 2016.

[128] Qinyi Xu, Yan Chen, BeiBei Wang, and KJ Ray Liu. Radio biometrics: Human recognition through a wall. *IEEE Transactions on Information Forensics and Security*, 12(5):1141–1155, 2017.

[129] Jialei Yang, James M Keller, Mihail Popescu, and Marjorie Skubic. Sleep stage recognition using respiration signal. In *Proceedings of the 38th Annual International Conference of the Engineering in Medicine and Biology Society (EMBC)*, 2016.

[130] Zheng Yang, Chenshu Wu, Zimu Zhou, Xinglin Zhang, Xu Wang, and Yunhao Liu. Mobility increases localizability: A survey on wireless indoor localization using inertial sensors. *ACM Computing Surveys (Csur)*, 47(3):54, 2015.

[131] Zhicheng Yang, Parth H. Pathak, Yunze Zeng, Xixi Liran, and Prasant Mohapatra. Vital sign and sleep monitoring using millimeter wave. *ACM Transactions on Senor Networks*, 13(2):14:1–14:32, April 2017.

[132] Moustafa Youssef and Ashok Agrawala. The horus wlan location determination system. In *Proceedings of the 3rd international conference on Mobile systems, applications, and services*, pages 205–218. ACM, 2005.

[133] Jaeseok Yun and Min-Hwan Song. Detecting direction of movement using pyroelectric infrared sensors. *IEEE Sensors Journal*, 14(5):1482–1489, 2014.

[134] A Zaffaroni, L Gahan, L Collins, E O'hare, C Heneghan, C Garcia, I Fietze, and T Penzel. Automated sleep staging classification using a non-contact biomotion sensor. *Age (yrs)*, 31:9–3, 2014.

[135] F. Zhang, C. Chen, B. Wang, H. Q. Lai, and K. J. R. Liu. A time-reversal spatial hardening effect for indoor speed estimation. In *Proc. of IEEE ICASSP*, pages 5955–5959, March 2017.

[136] Feng Zhang, Chen Chen, Beibei Wang, Hung-Quoc Lai, Yi Han, and KJ Ray Liu. Wiball: A time-reversal focusing ball method for decimeter-accuracy indoor tracking. *IEEE Internet of Things Journal*, 2018.

[137] Feng Zhang, Chen Chen, Beibei Wang, Hung-Quoc Lai, Yi Han, and KJ Ray Liu. Widetect: A robust and low-complexity wireless motion detector. In *2018 IEEE International Conference on Acoustics, Speech and Signal Processing (ICASSP)*, pages 6398–6402. IEEE, 2018.

[138] Feng Zhang, Chen Chen, Beibei Wang, and KJ Ray Liu. Wispeed: A statistical electromagnetic approach for device-free indoor speed estimation. *IEEE Internet of Things Journal*, 5(3):2163–2177, 2018.

[139] Feng Zhang, Chenshu Wu, Min Wu, Bogus Dan, Hangfang Zhang, Beibei Wang, and KJ Ray Liu. Smars: sleep monitoring via ambient radio signals. *Submitted to NSDI*, 2018.

[140] Fusang Zhang, Daqing Zhang, Jie Xiong, Hao Wang, Kai Niu, Beihong Jin, and Yuxiang Wang. From fresnel diffraction model to fine-grained human respiration sensing with commodity wi-fi devices. *Proceedings of the ACM on Interactive, Mobile, Wearable and Ubiquitous Technologies (UbiComp)*, 2(1):53:1–53:23, March 2018.

[141] Jie Zhang, Zhanyong Tang, Meng Li, Dingyi Fang, Petteri Tapio Nurmi, and Zheng Wang. Crosssense: towards cross-site and large-scale wifi sensing. 2018.

[142] Mingmin Zhao, Shichao Yue, Dina Katabi, Tommi S. Jaakkola, and Matt T. Bianchi. Learning sleep stages from radio signals: A conditional adversarial architecture. In *Proceedings of the 34th International Conference on Machine Learning (ICML)*, volume 70, 06–11 Aug 2017.

[143] Zimu Zhou, Zheng Yang, Chenshu Wu, Longfei Shangguan, and Yunhao Liu. Omnidirectional coverage for device-free passive human detection. *IEEE Transactions on Parallel and Distributed Systems*, 25(7):1819–1829, 2014.

[144] Hai Zhu, Fu Xiao, Lijuan Sun, Ruchuan Wang, and Panlong Yang. R-ttwd: Robust device-free through-the-wall detection of moving human with wifi. *IEEE Journal on Selected Areas in Communications*, 35(5):1090–1103, 2017.